RICE UNIVERSITY

Third Harmonic Generation from Aligned Single-Wall Carbon Nanotubes

by

Darius T. Morris, Jr.

A THESIS SUBMITTED
IN PARTIAL FULFILLMENT OF THE
REQUIREMENTS FOR THE DEGREE

Doctor of Philosophy

APPROVED, THESIS COMMITTEE:

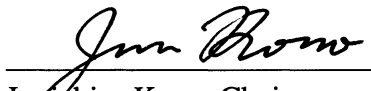

Junichiro Kono, Chair
Professor of Electrical & Computer
Engineering and Physics & Astronomy

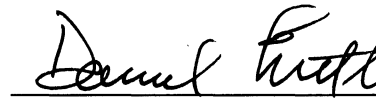

Daniel M. Mittleman
Professor of Electrical & Computer
Engineering

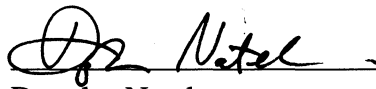

Douglas Natelson
Professor of Physics & Astronomy

Houston, Texas

April, 2012

ABSTRACT

Third Harmonic Generation from Aligned Single-Wall Carbon Nanotubes

by

Darius T. Morris, Jr.

Optical properties of single-wall carbon nanotubes (SWCNTs) have been extensively studied during the last decade, and much basic knowledge has been accumulated on how light emission, scattering, and absorption occur in the realm of linear optics. However, their nonlinear optical properties remain largely unexplored. Here, we have observed strong third harmonic generation from highly aligned SWCNTs with intense mid-infrared radiation. Through power dependent experiments, we have determined the absolute value of the third-order nonlinear optical susceptibility, $\chi^{(3)}$, of our SWCNT film to be 6.92×10^{-12} esu, which is three orders of magnitude larger than that of the fused silica reference sample we used. Furthermore, through polarization-dependent third harmonic generation experiments, all the nonzero tensor elements of $\chi^{(3)}$ have also been extracted. The contribution of the weaker tensor elements to the overall $\chi^{(3)}$ signal has been calculated to be approximately 1/6 of that of the dominant $\chi^{(3)}_{zzzz}$ component. These results open up new possibilities for application of carbon nanotubes in optoelectronics.

Acknowledgments

I would first like to thank my Lord and Savior, Jesus Christ for giving me the courage to take this journey toward my PhD. He gave me the strength, guidance, and peace to get through this process. Through Him I know that all things are possible.

I would also like to thank my mom, dad, sister and the rest of my family. They always understood when I couldn't make it home for the holidays or even when I would disappear for weeks at a time. These are the people from whom I draw my inspiration. Thank you for your unconditional love and encouragement, and for keeping in your prayers. I love you all!

Thank you to Dr. Kono for giving me opportunity to work in your lab and travel to other countries to do research. Thanks for always taking time out of your busy schedule to address any experiment issues or for any impromptu physics lessons. I am happy to have had an advisor who applied a great amount of pressure for obtaining excellent results, but also one that encouraged me to have another drink over a game of pool. I would like to also thank Gary Woods for his invaluable knowledge that he lent to this project. Thank you to my committee for taking the time to read my thesis and participate in my defense. Thanks to my collaborators for taking interest in my research, and giving excellent insight on how to make my research stronger.

Thank you to my colleagues in Kono Lab for your endless support in the lab and for your insight on experimental methods. I enjoyed sharing stories and life experiences with you on a daily basis. I can honestly say that I had one of the best experiences that a graduate student could have, because of you!

I would like to also thank all of my funding agencies, especially MIRTHE for providing the extra knowledge and opportunities that I gained from the workshops, presentations, and

retreats. Thank you to Roxanne for making sure that I get to/from those destinations and that I have a place to stay, no matter the mishap.

Thanks to Sarah and other Kono Lab staff who not only helped with school/administrative issues, but also any personal issues that came up in graduate school, and for making sure my money was always on time. I would also like to thank Theresa Chatman and the AGEP program for their constant support, and making sure that I got fed.

Last but not least, to my friends that I had before graduate school and the ones that I've made while I was here. Thanks for keeping me entertained on a daily basis, keeping me up on music, sports, politics, and entertainment, when lab doesn't permit me to do so. Thank you for always lending an ear when things in my life didn't go the way that they are supposed to, and making me laugh when I needed it. Thank you to my girlfriend, Jasmine Brown, for understanding the life of a graduate student, being supportive, being in love with me, and making me want to be a better man!

Contents

Illustrations

Chapter 1

Introduction

In this dissertation, we have studied third harmonic generation in single-wall carbon nanotubes (SWCNTs).

Carbon-based materials have gained exponentially growing interest over the past 70 years, since the work by Wallace, who showed a linear $E(k)$ dispersion relation for monolayer graphene [27, 28]. Because of this linear dispersion, electrons in graphene behave like photons, possessing a high velocity ($v_F \sim 10^6$ m/s), and a high electron mobility ($\sim 2 \times 10^5$ cm^2/Vs) at room temperature. This linear energy dispersion also leads to a universal optical conductivity in graphene, $\pi e^2/2h$, in which each atomic layer of graphene absorbs 2.3% of incident light from the visible to the far-infrared [29, 30].

These unique electrical and optical properties have also trickled down to graphene's various derivatives, shown in Figure 1.1. Specifically, single-wall carbon nanotubes (SWCNTs) are unique 1D systems with a wide range of unusual properties. They can be semiconducting or metallic, depending on how they are rolled. Metallic tubes have been measured to have a fermi velocity of $v_F = 8.1 \times 10^5$ m/s, a measured electron mobility of 100,000 cm^2/Vs and boast a current carrying capacity ($\sim 10^9$ A/cm^2) that can be up to 1000 times greater than that of copper. These properties make them a popular material for nanoelectronics, expected to replace copper one day in nanocircuits and inter-connects. Semiconducting carbon nanotubes are direct bandgap semiconductors (electrons in the conduction band can directly emit photons after recombination with a hole in the valence band), making carbon nanotubes an ideal candidate for opto-electronic technologies like

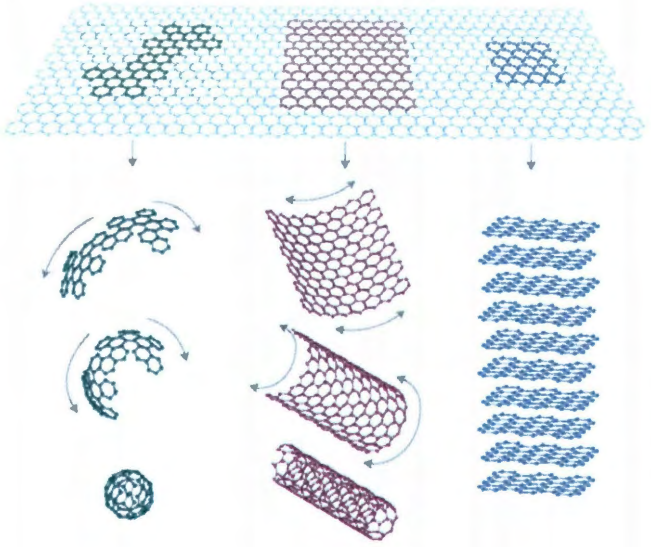

Figure 1.1 : 2D graphene and its derivatives, (a) 0D fullerenes, (b) 1D carbon nanotubes, and (c) 3D graphite [1].

light emitting diodes (LEDs). Because of the diameter dependent bandgap (semiconducting carbon nanotubes have the ability to absorb and emit light from the visible to the infrared through interband transitions) present in carbon nanotubes, these LEDs will also be widely tunable. These fascinating properties make graphene and SWCNTs great candidates for a wide variety of potential applications, such as transistors, capacitors, lasers, LEDs, and detectors [31–36]. Though much work has been done on the electrical and linear optical properties of SWCNTs, such as absorption and emission (properties that take place under weak electric fields), only a small amount of studies have been done on the nonlinear optical properties of SWCNTs.

Since the demonstration of the first working laser by Mainman in 1960, there have been many advances in nonlinear optics. The birth of the field in 1961 was marked by a notable second harmonic generation experiment by Franken *et al.* [37–39]. The field studies the

modification of linear optical properties under sufficiently large laser electric fields. The interaction between intense light and matter leads to a wide spectrum of phenomena, such as optical frequency conversion, phase conjugation, optical limiting, nonlinear refraction, and Raman scattering. Because, nonlinear processes belong to some of the fastest phenomena known, they can be used for processing data and functions on the femto- and picosecond time scale. The far reaching impact of this field is realized in the technologies of nonlinear crystals, widely tunable ultra-fast lasers, optical switches, and optical limiters. The study of these nonlinear optical properties in different materials has allowed this field to evolve into one of the most fascinating areas in physics and engineering.

Chapter 2 of this thesis will review the band structure of graphene and SWCNTs, and the subsequent linear optical properties that develop. Chapter 3 will go over nonlinear optics and the processes that develop under intense laser electric fields. It will also review the nonlinear optical susceptibility that describes these processes. Chapter 4 will deal with the previous theoretical and experimental second and third-order nonlinear optical studies on SWCNTs. Chapter 5 will describe our sample, experimental setup, and procedures of our experiment. Chapter 6 will present and discuss results of our experiment on the power dependence of the third harmonic for SWCNTs, allowing us to determine the absolute value of the third-order nonlinear susceptibility, $\chi^{(3)}$. Chapter 7 will review our experiment on the polarization dependence of the third harmonic for SWCNTs, allowing us to extract the nonzero tensor components of $\chi^{(3)}$.

Chapter 2

Band Structure and Linear Optical Properties of Single-Wall Carbon Nanotubes

2.1 Graphene Band Structure

A single-wall carbon nanotube (SWCNT) is described as a single sheet of graphene rolled into a cylindrical 1D nanostructure. Thus, the 1D energy dispersion relations for SWCNTs, from which many of their electrical and optical properties originate, are constructed from the 2D band structure of graphene.

Graphene is a two-dimensional hexagonal lattice of sp^2-bonded carbon atoms. This lattice can be constructed from a 2 carbon atom unit cell (separated by $a_{C-C} = 1.42\,\text{Å}$), translated by the primitive lattice vectors, $\vec{a}_1$ and $\vec{a}_2$, situated at 60° angles to each other (Figure 2.1). These primitive vectors are defined as

$$\vec{a}_1 = \frac{a}{2}\left(\sqrt{3}, 1\right) \text{ and } \vec{a}_2 = \frac{a}{2}\left(\sqrt{3}, -1\right), \tag{2.1}$$

where $a = \sqrt{3}a_{C-C} = 2.49\,\text{Å}$. From these primitive lattice vectors, the reciprocal lattice vectors are derived as [40]

$$\vec{b}_1 = \frac{2\pi}{3a}\left(\sqrt{3}, 3\right) \text{ and } \vec{b}_2 = \frac{2\pi}{3a}\left(\sqrt{3}, -3\right). \tag{2.2}$$

The 2D energy dispersion relation of graphene can be derived within the nearest-neighbor tight binding approximation [28]. We introduce the atomic orbitals

$$\varphi_A(\vec{r}) \text{ and } \varphi_B(\vec{r}) \tag{2.3}$$

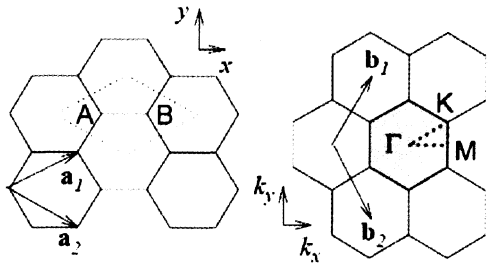

Figure 2.1 : Unit vectors in and primite cell (a) in real space and (b) reciprocal space [2].

which are eigenfunctions of the carbon atom at sites A and B, respectively. Thus, we express our wavefunctions inside of a periodic lattice as linear combinations of atomic orbitals

$$\psi_{\mathrm{A}}(\vec{r}) = \sum_{R} e^{i\vec{k}\cdot\vec{R}} \varphi_{\mathrm{A}}(\vec{r}-\vec{R}) \tag{2.4}$$

$$\psi_{\mathrm{B}}(\vec{r}) = \sum_{R} e^{i\vec{k}\cdot\vec{R}} \varphi_{\mathrm{B}}(\vec{r}-\vec{R}) \tag{2.5}$$

where $\vec{k}$ is the Bloch wavevector, restricted to the 1st Brillouin Zone and $\vec{R}$ is the translational vector of the lattice. The total wavefunction is a superposition of both the carbon site A and B basis vectors

$$\Psi(\vec{r}) = c_{\mathrm{A}}\psi_{\mathrm{A}}(\vec{r}) + c_{\mathrm{B}}\psi_{\mathrm{B}}(\vec{r}), \tag{2.6}$$

which must satisfy the Schrödinger equation,

$$\hat{H}\Psi = \varepsilon\Psi, \tag{2.7}$$

where $\hat{H} = \hat{H}_{\mathrm{Site}} + \hat{H}_{\mathrm{NN}}$. Here $\hat{H}_{\mathrm{Site}}$ and $\hat{H}_{\mathrm{NN}}$ are the on-site Hamiltonian and the nearest-neighbor Hamiltonian, respectively. If we multiply the Schrödinger equation by ψ_{A} from

the left and integrate over the unit cell, we get

$$\langle \psi_A|H|\Psi\rangle = c_A\langle \varphi_A|H_{Site}|\varphi_A\rangle + c_B\langle \varphi_A|H_{NN}|\varphi_B\rangle\left(1+e^{-i\vec{k}\cdot\vec{a}_1}+e^{-i\vec{k}\cdot\vec{a}_2}\right) \quad (2.8)$$

$$= c_A\langle \varphi_A|H_{Site}|\varphi_A\rangle + c_B\gamma\left(1+e^{-i\vec{k}\cdot\vec{a}_1}+e^{-i\vec{k}\cdot\vec{a}_2}\right), \quad (2.9)$$

where γ is the transfer integral between two neighboring sites, defined as

$$\int \varphi_A^*(\vec{r})H_{NN}\varphi_B(\vec{r}-\vec{R})d^3r \quad (2.10)$$

Similarly,

$$\langle \psi_B|H|\Psi\rangle = c_A\gamma\left(1+e^{i\vec{k}\cdot\vec{a}_1}+e^{i\vec{k}\cdot\vec{a}_2}\right) + c_B\langle \varphi_B|H_{Site}|\varphi_B\rangle \quad (2.11)$$

For the eigenvalues of the Hamiltonian,

$$\langle \psi_A|\varepsilon|\Psi\rangle = c_A\varepsilon\langle \varphi_A|\varphi_A\rangle + c_B\varepsilon\langle \varphi_A|\varphi_B\rangle\left(1+e^{-i\vec{k}\cdot\vec{a}_1}+e^{-i\vec{k}\cdot\vec{a}_2}\right). \quad (2.12)$$

Because of the orthogonality of the wavefunctions $\langle \varphi_i|\varphi_j\rangle = \delta_{ij}$

$$\langle \psi_A|\varepsilon|\Psi\rangle = c_A\varepsilon. \quad (2.13)$$

Similarly for site B

$$\langle \psi_B|\varepsilon|\Psi\rangle = c_A\varepsilon. \quad (2.14)$$

Thus, the Schrödinger equation becomes

$$\begin{pmatrix} 0 & f(\vec{k}) \\ -f^\dagger(\vec{k}) & 0 \end{pmatrix}\Psi = \begin{pmatrix} -\varepsilon & 0 \\ 0 & -\varepsilon \end{pmatrix}\Psi, \quad (2.15)$$

where $f(\vec{k}) = -\gamma(1+e^{i\vec{k}\cdot\vec{a}_1}+e^{i\vec{k}\cdot\vec{a}_2}) = -\gamma(1+2e^{\sqrt{3}k_xa/2}\cos(k_ya/2))$ and γ is the nearest-neighbor C-C tight binding intersublattice transfer energy, Equation (2.10) ($\gamma \approx 2.7$eV). The solution for the eigenvalue problem $|H-\varepsilon I| = 0$ leads to the energy dispersion relation for graphene (Figure 2.2),

$$E_{G,2D}^{\pm}(\vec{k}) = \pm\gamma\sqrt{1+4\cos\frac{\sqrt{3}k_xa}{2}\cos\frac{k_ya}{2}+\cos\frac{k_ya}{2}}, \quad (2.16)$$

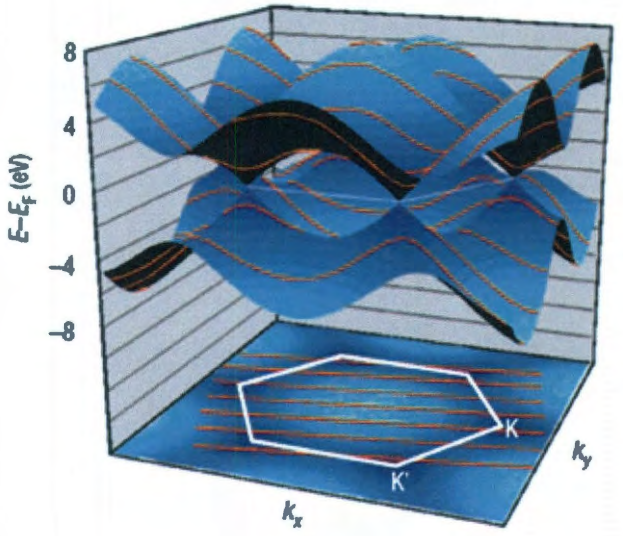

Figure 2.2 : Calculated 2D energy dispersion for graphene [3].

From this equation, we can investigate the energy dispersion relation near the Dirac points, K and K' at the corners of the graphene Brillouin zone (Figure 2.1)

$$K = \frac{2\pi}{\sqrt{3}a}\left(1, \frac{1}{\sqrt{3}}\right) \text{ and } K' = \frac{2\pi}{\sqrt{3}a}\left(1, -\frac{1}{\sqrt{3}}\right) \tag{2.17}$$

At these points, electrons have a linear energy dispersion relation, and thus, act as massless particles. Because these two bands touch at a single Dirac point, graphene is considered to be a zero-gap semiconductor. This 2D linear dispersion relation becomes the basis for deriving the band structure of SWCNTs.

2.2 Single-Wall Carbon Nanotube Band Structure

The atomic structure of a SWCNT is defined by its chiral indices, (n,m), which denote the way graphene is rolled into a SWCNT (Figure 2.3). The axis along which the graphene is

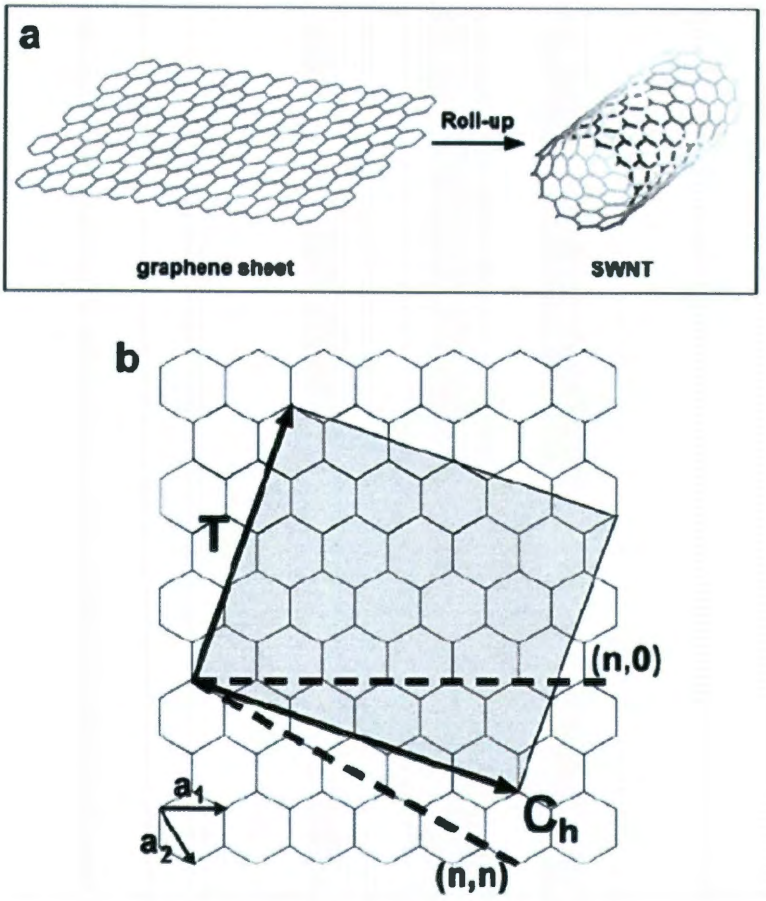

Figure 2.3 : (a) Conceptually, SWCNTs are 1D cylindrical sheets of graphene, (b) rolled along chrial vector C_h [4].

rolled points along the direction of the chiral vector $\vec{C}_h$, defined as

$$\vec{C}_h = m\vec{a}_1 + n\vec{a}_2, \tag{2.18}$$

where $\vec{a}_1$ and $\vec{a}_2$ are graphene's primitive lattice vectors in real space, defined in Equation (2.1), and m and n are non-negative integers ($m \geq n$).

From these chiral indices, SWCNTs are categorized into three main types: zigzag ($m = 0$), armchair ($n = m$), and chiral ($n \neq m$ and $m \neq 0$), as shown in Figure 2.4. The magnitude of the chiral vector is equal to the circumference of the nanotube, and thus, the diameter of

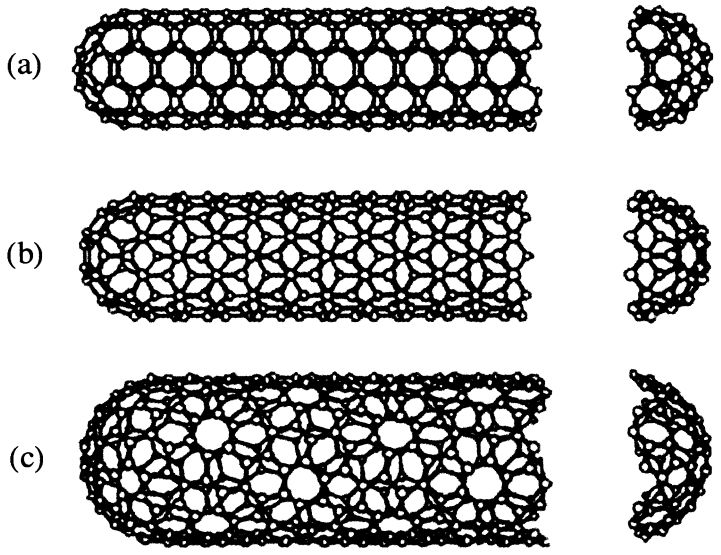

Figure 2.4 : Three different types of SWCNTs (a) armchair (n,n), (b) zigzag $(n,0)$, and (c) chiral (n,m) [4].

the tube, d_t, can be expressed as

$$d_t = \frac{\left|\vec{C}_h\right|}{\pi} = \frac{a}{\pi}\sqrt{m^2+mn+n^2} \tag{2.19}$$

The perpendicular vector to the chiral vector shown in Figure 2.3b, $\vec{T}$, is called the translational vector and is defined as

$$\vec{T} = t_1\vec{a}_1 + t_2\vec{a}_2, \tag{2.20}$$

where $t_1 = (2m+n)/d_R, t_2 = -(2n+m)/d_R$ and d_R is the greatest common divisor of $(2m+n,m+2n)$. The magnitude of the translational vector is equal to the length of the unit cell of the (n,m) nanotube, and is defined as

$$\left|\vec{T}\right| = \frac{\sqrt{3}\left|\vec{C}_h\right|}{d_R}. \tag{2.21}$$

The corresponding reciprocal lattice vectors are

$$K_1 = \frac{1}{N}\left(-t_2\vec{b}_1 + t_1\vec{b}_2\right) \text{ and } K_2 = \frac{1}{N}\left(m\vec{b}_1 - n\vec{b}_2\right). \tag{2.22}$$

The 1D energy dispersion relations for SWCNTs are derived from the 2D band structure of graphene, using the zone-folding method. In the zone-folding method, the wavefunctions are subject to the circumferential periodic boundary condition

$$\psi_k(\vec{r}+\vec{C}_h) = e^{i\vec{k}\cdot\vec{C}_h}\psi_k(\vec{r}) \tag{2.23}$$

and are thus quantized along the cylindrical direction in both real and reciprocal space, i.e.,

$$\vec{K}_1 \cdot \vec{C}_h = 2\pi\mu, \text{ where } \mu \text{ is an integer .} \tag{2.24}$$

Using this quantization condition and the 2D energy dispersion relation, we find that the 1D energy dispersion relation for SWCNTs becomes

$$E_{1D}^{\pm} = E_{G,2D}^{\pm}\left(k\frac{\vec{K}_2}{\left|\vec{K}_2\right|} + \mu\vec{K}_1\right), \text{ where } \mu = 0, 1, ..., N-1, \tag{2.25}$$

where μ is the zone-folding index. The allowed wave vectors in the carbon nanotube reciprocal space are represented by the parallel cutting lines in the graphene Brillouin zone, as shown in Figure 2.5. The continuous wave vectors along the direction of $\vec{K}_2$, are represented by the wavenumber k. If one of the cutting lines passes through graphene's K point, then the SWCNT is metallic ($|m-n| \mod 3 = 0$). Otherwise, the tubes are semiconducting ($|m-n| \mod 3 = 1$ or 2).

Typical energy dispersion relations for metallic and semiconducting tubes can be seen in Figure 2.6. The band gap of semiconducting tubes is the energy separation between the conduction and valence bands, and is related to the diameter by the following equation

$$E_g = \frac{2\gamma a_{C-C}}{d_t}, \tag{2.26}$$

where γ is the transfer energy [(Equation (2.10)], a_{C-C} is the inter-atomic distance, and d_t is the tube diameter. From this 1D energy dispersion relation, many of the linear optical properties of SWCNTs are derived, and will be outlined in the following section.

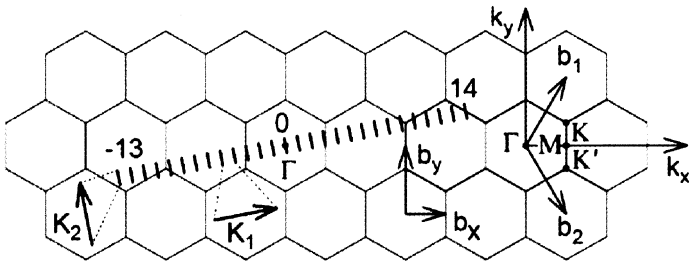

Figure 2.5 : Zone folding of the (4,2) nanotube. The parallel equidistant lines represent the cutting lines of the allowed k states for the (4,2) nanotube [2].

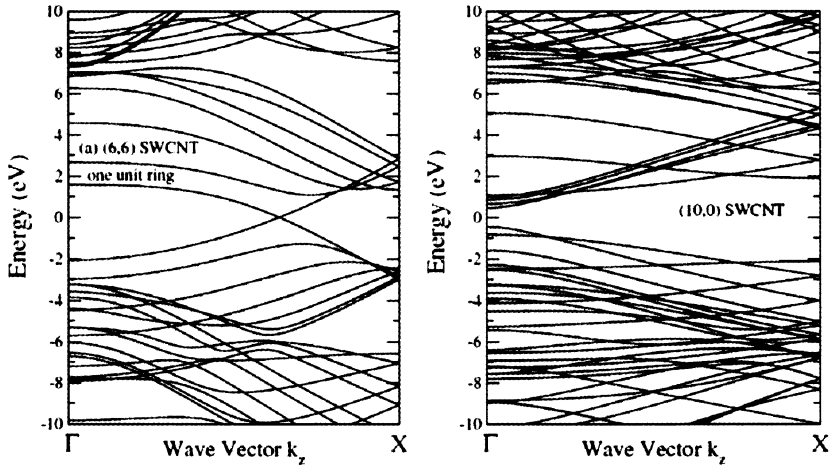

Figure 2.6 : 1D energy dispersion for the(a) metallic (6,6) armchair nanotube, (b) and the semiconducting (10,0) zigzag nanotube [5].

2.3 Linear Optical Properties of Single-Wall Carbon Nanotubes

Linear optical properties of materials refer to such basic processes as absorption, reflection, scattering, and emission, whose intensities increase linearly with the incident electric field. These processes occur under the influence of relatively small light intensities. Once the electric field of light becomes large, the material will have a nonlinear response, which will

be discussed in the next chapter [11]. The linear optical processes are represented by the first term in the following equation:

$$P(t) \propto \chi^{(1)}E(t) + \chi^{(2)}E^2(t) + \chi^{(3)}E^3(t) + ..., \tag{2.27}$$

where $P(t)$ is the induced polarization due to incident electric field, $E(t)$, and $\chi^{(n)}$ is the n^{th}-order susceptibility. $\chi^{(1)}$ is the linear susceptibility that describes the polarization of the material under small electric fields and is defined as

$$\vec{P}(\omega) = \varepsilon_0 \chi^{(1)}(\omega)\vec{E}(\omega), \tag{2.28}$$

where ε_0 is the permittivity in vacuum. The electric displacement $\vec{D}$ is defined as

$$\vec{D} = \varepsilon_0 \vec{E} + \vec{P} \tag{2.29}$$

$$= \varepsilon_0 \varepsilon_r \vec{E}, \tag{2.30}$$

where $\varepsilon_r = 1 + \chi^{(1)}$ is the relative permittivity. The index of refraction of a material is defined as

$$n = \sqrt{\varepsilon_r}. \tag{2.31}$$

As outlined in the last section, when a 2D graphene is rolled along a chiral vector, the SWCNT energy is quantized along the circumferential direction of the tube. Many of the experimentally observable linear interband optical properties of SWCNTs are related to its quasi-1D density of states. The density of states is the total number of states per unit interval of energy [41]. The 1D dispersion relation for linear ($p = 1$) and parabolic ($p = 2$) energy bands can be expressed as

$$E = E_0 + c_k k^p \Rightarrow k = \left(\frac{E - E_0}{c_k}\right)^{1/p}, \tag{2.32}$$

where c_k is a constant related to the effective mass.

The volume of a 1-dimensional k-space containing wavevectors smaller than k is

$$\Omega_1(k) = 2k \Rightarrow \Omega_1(k) = 2\left(\frac{E - E_0}{c_k}\right)^{1/p}. \tag{2.33}$$

By integrating this volume and counting the number of k-states for infinitesimally small energies, we get the density of states for the 1D dispersion relation as

$$D_1(E) = \frac{2}{pc_k^{1/p}}(E - E_0)^{\frac{1}{p}-1} \tag{2.34}$$

For metallic SWCNTs, electrons behave like photons (i.e., massless) due to the linear ($p = 1$) dispersion relation near the Dirac point. Thus, its density of states is constant, $D_{1,lin}(E) = 1/c_k$, near the Dirac point. For semiconducting SWCNTs, electrons have a parabolic dispersion relation near the $k = 0$ point, and thus, the density of states is $D_{1,para}(E) = \frac{1}{2\sqrt{c_k(E-E_0)}}$. As can be seen in Figure 2.7a, the density of states possesses sharp peaks, called van Hove singularities. Metallic tubes also show van Hove singularities, associated with higher subbands, as also shown in Figure 2.7a.

These van Hove singularities give rise to peaks in the interband absorption spectrum. Many of these transitions, specifically the semiconducting S_{11} and S_{22}, and metallic M_{11} transitions, have been studied using absorption and Raman spectroscopy experiments, as well as photoluminescence in the case of semiconducting nanotubes. These optical transitions are strong and sharp, allowing scientists to probe a single type of tubes in these various experiments. These transitions also strongly depend on the diameter (which determines the bandgap) of the tubes, as shown in Figure 2.8.

There are a number of selection rules that define whether a transition is allowed within a SWCNT for absorbing and emitting light [8]. In general, as in any crystalline solids, only direct transitions ($\Delta k = 0$) are allowed between subbands (Figure 2.9). Also, in nanotubes with inversion symmetry (zig-zag tubes and armchair tubes), only even wavefunctions [$\Psi(x) = \Psi(-x)$] exist in the valence and conduction bands, and thus, only even num-

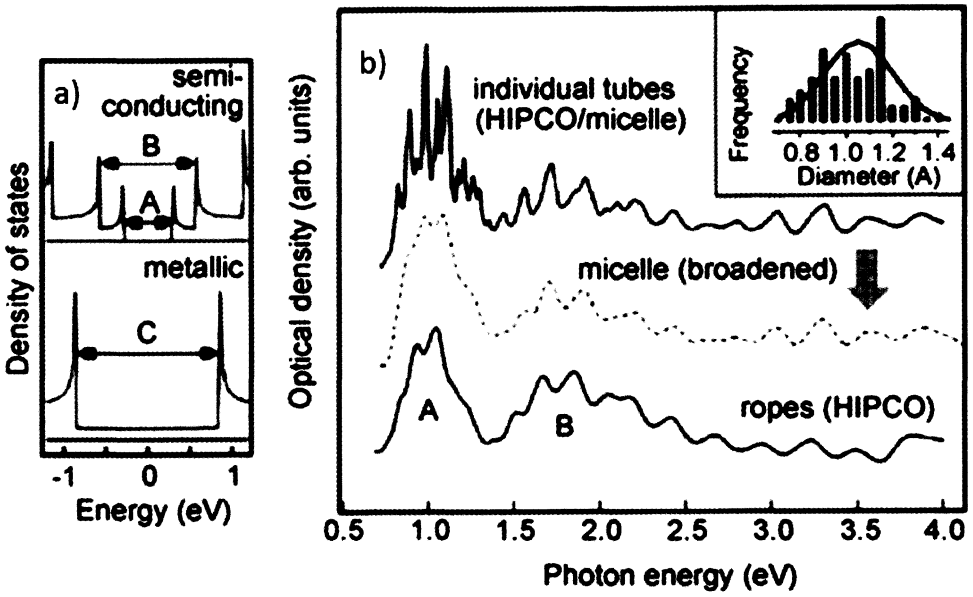

Figure 2.7 : (a) 1D density of states for metallic and semiconducting nanotubes. (b) Optical density (absorption) measured for carbon nanotubes suspended in different surfactant [6].

ber subband transitions are allowed. For light polarized parallel to the SWCNT axis, only transitions between subbands with the same index ($\Delta n = 0$) are allowed. For light polarized perpendicular SWCNT axis, transitions between subbands with a different band index ($\Delta n = \pm 1$) is allowed; however, these transitions are suppressed by the depolarization effect [42].

In absorption experiments, the van Hove singularities are evident due to the sharp features that appear in a typical absorption experiment. Because several tubes have similar diameters, absorption energies across bandgap can be the same for various tubes when measuring a collection of SWCNTs. Thus, in the case of a SWCNT sample, many of the sharp features become broadened, and spectral decomposition is needed in order to determine the SWCNT composition of the sample (Figure 2.7b).

Another linear optical process experimentally investigated is photoluminescence (PL)

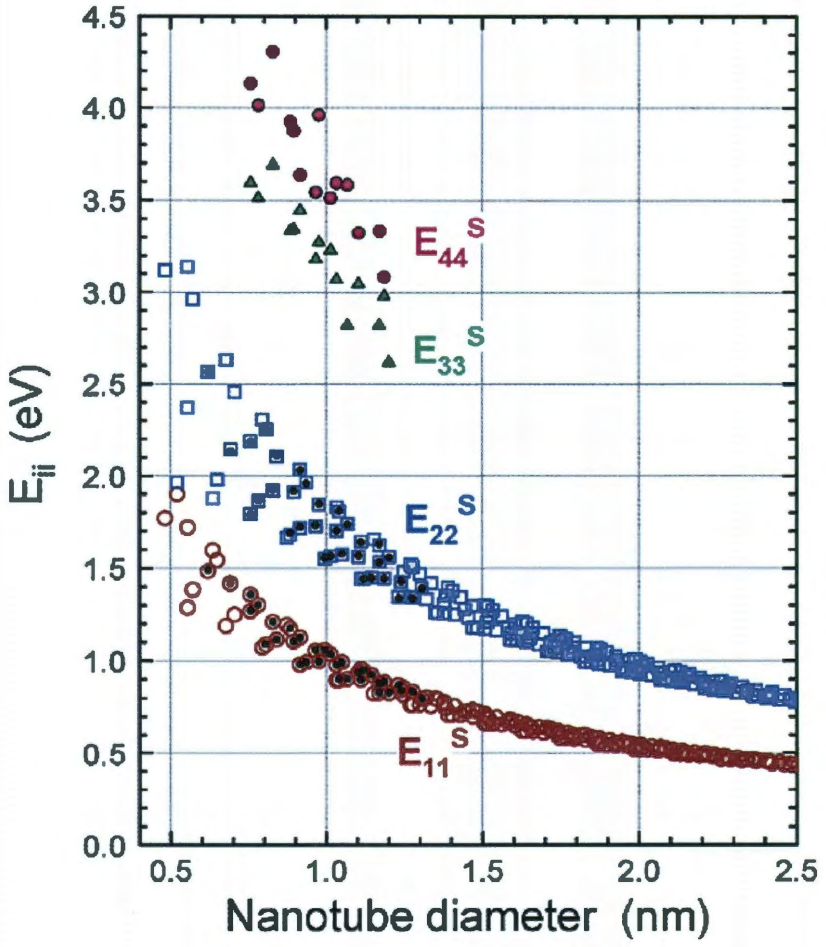

Figure 2.8 : Kataura plot showing the decrease in transition energy with increasing diameter of the nanotubes [7].

in nanotubes [43,44]. In a PL experiment, an electron-hole pair is created, after a photon is absorbed and an electron is excited to a high energy level. This excitation can be done with nonresonant photon energies, or with energies that are resonant with higher SWCNT transitions. After the excitation both the electron and hole relax down to a lower energy level in both the conduction and valence bands and recombine, creating a photon at the energy difference between the lower levels. In a photoluminescence excitation (PLE) experiment,

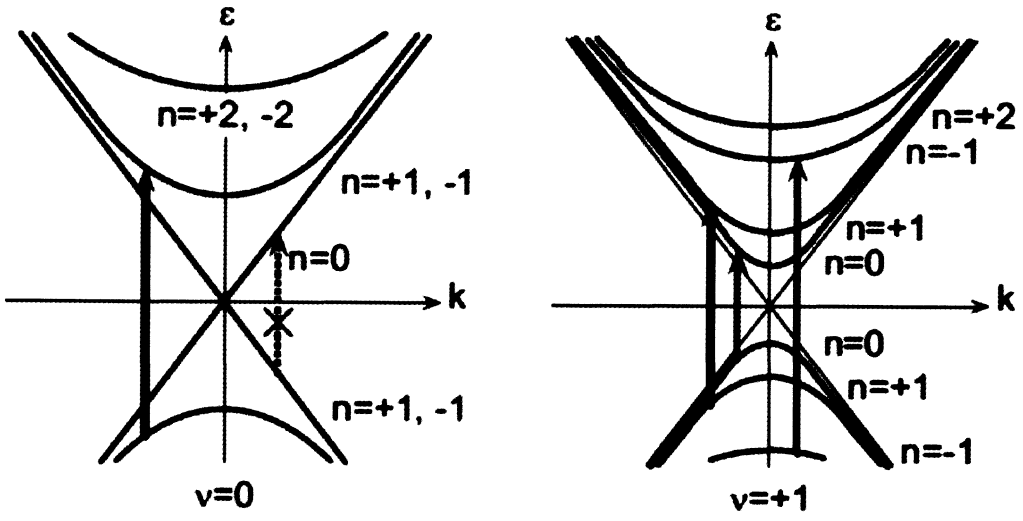

Figure 2.9 : The optical selection rules of (left) metallic ($\nu = 0$) and semiconducting(right) ($\nu = \pm 1$) nanotubes for light incident parallel to the nanotube axis. The indices n correspond to the optical transitions from bands with equal momentum angular momentum [8].

the frequency of the excitation light is varied, and the luminescence from these transitions are monitored, as shown in Figure 2.10. Because nanotubes have a unique set of E_{11} and E_{22} transitions, characterization of samples is more effective than the absorption process, as seen in Figure 2.10. This process, however, does not happen in metallic tubes, because of the absence of a bandgap.

Raman scattering spectroscopy, shown in Figure 2.11, is one of the most popular characterization techniques for nanotubes. In this process, a material is excited with a photon, and energy is absorbed/emmitted by phonons (vibrational/rotational modes) within the material. After the recombination of the electron and hole, the resulting photon is red-shifted or blue-shifted from the original excitation energy, offering much information about the nanotubes. After a SWCNT is resonantly excited, several modes can be measured from the subsequent Raman spectra, like the radial breathing mode (RBM), G, D, and G' modes. The

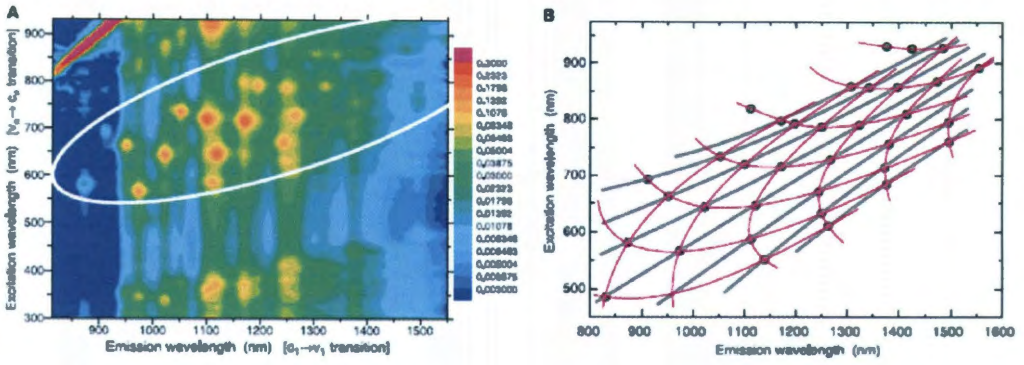

Figure 2.10 : (a) PLE map from sample containing many chirality of tubes. (b)Shows spectral peak positions from the PLE map, with lines that show perceived patterns in the data [9].

RBM corresponds to radial expansion-contraction of the nanotube [45, 46], which makes its frequency significant because it depends on the nanotube diameter d_t (in nanometers) as

$$f_{\mathrm{RBM}}\,(\mathrm{cm}^{-1}) = \frac{223}{d_t} + 10. \tag{2.35}$$

The G mode corresponds to the planar vibrations of carbon atoms. Splitting of the G mode corresponds to vibrations along the axis of the tube (longitudinal optical) and along the circumferential (transverse optical) direction of the tube [2, 47]. The splitting pattern and intensity depend on the tube structure and excitation energy, and they can be used to estimate the tube diameter and whether the tube is metallic or semiconducting. The D mode describes the out-of-plane stretch that breaks the cylindrical symmetry of the nanotube. This happens when defects or dopants are present in the nanotube structure, and thus, the appearance and size of the D band denotes the degree of purity of the measured SWCNT. Stokes and anti-Stokes scattering can be used to further characterize semiconducting nanotubes, where the S_{22} energy transition is blue-shifted for $|m-n| \mod 3 = 1$ nanotubes and red-shifted for $|m-n| \mod 3 = 2$ nanotubes, with increasing temperature.

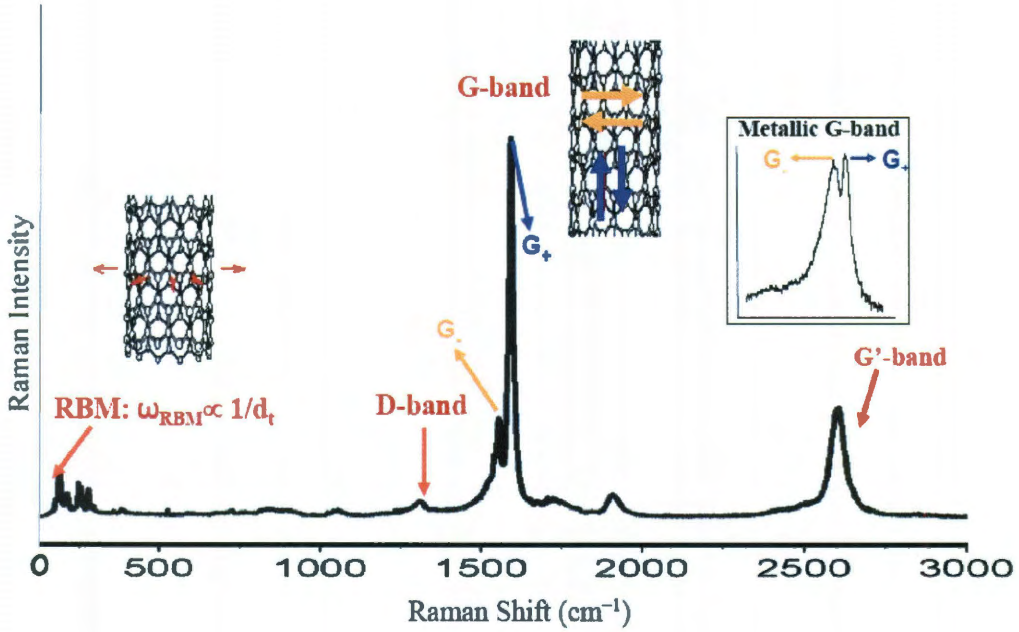

Figure 2.11 : Typical Raman spectrum from HiPco nanotube sample obtained with excitation energy $E_L = 1.96\,\text{eV}$, illustrating the radial breathing, G, D, and G' modes, as well as the intermediate-frequency modes and iTOLA bands in the insets [10].

Chapter 3

Theory of Nonlinear Optical Susceptibilities

3.1 What is nonlinear optics?

When light is incident on a material, the electric field component of light, transverse to the propagation direction, displaces the electrons present in the material. The electrons propagate back and forth around a positive charge creating a dipole moment in the material (Figure 3.1). This dipole moment per unit volume is known as the polarization. The polarization in the material can be described by the following relationship:

$$\tilde{P}(t) = \chi^{(1)}\tilde{E}(t) + \chi^{(2)}\tilde{E}^2(t) + \chi^{(3)}\tilde{E}^3(t) + \ldots \quad (3.1)$$

$$\equiv \tilde{P}^{(1)}(t) + \tilde{P}^{(2)}(t) + \tilde{P}^{(3)}(t) + \ldots \quad (3.2)$$

where $\chi^{(1)}$, $\chi^{(2)}$, and $\chi^{(3)}$ are the optical susceptibilities of the material system [11]. In the first term on the right hand side of the equation, the polarization in the material depends linearly on the strength of the applied electric field. Conventional, or linear, optics, is the study of $\tilde{P}^{(1)}(t)$ effects, like absorption, refraction, etc. as presented in the last chapter.

At sufficiently high incident fields, the restoring force of the electron no longer responds linearly with the applied electric field. The nonlinear polarizations are represented by $\tilde{P}^{(2)}(t) = \chi^{(2)}\tilde{E}^2(t)$ (second-order) and $\tilde{P}^{(3)}(t) = \chi^{(3)}\tilde{E}^3(t)$ (third-order) in the above equation. These higher-order polarizations produce effects that are qualitatively different from those in conventional linear optics. These effects are explored in nonlinear optics.

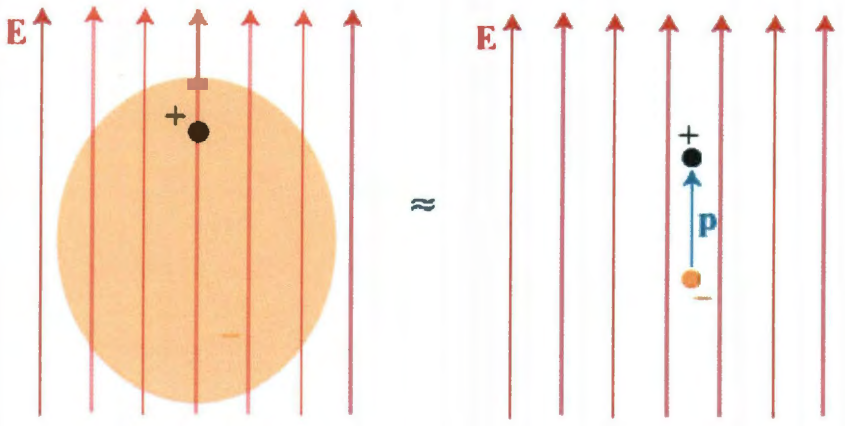

Figure 3.1 : An applied electric field induces a dipole moment in an atom.

3.2 Second-Order Nonlinear Optical Properties

The second term in Equation (3.2) describes second-order processes. Second-order nonlinear optical processes are only present in noncentrosymmetric crystals. Centrosymmetric crystals do not possess second-order properties due to its inversion symmetry. This concept will be further explained in Section 3.4, when we develop the anharmonic oscillator problem for a noncentrosymmetric crystal.

The electric field incident on a medium with two distinct frequency components, ω_1 and ω_2, is represented by

$$\tilde{E}(t) = E_1 e^{-i\omega_1 t} + E_2 e^{-i\omega_2 t} + \text{c.c.}, \tag{3.3}$$

where c.c. is the complex conjugate of the electric fields. When this field is incident on a medium with nonlinear susceptibility $\chi^{(2)}$, the second-order nonlinear polarization is given

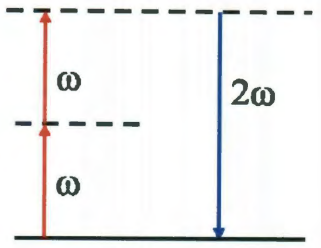

Figure 3.2 : Energy level diagram of the second order nonlinear process SHG. The solid line represents the ground state, while the dashed line represents virtual states [11].

by

$$\tilde{P}^{(2)}(t) = \chi^{(2)}\tilde{E}(t)^2 \tag{3.4}$$

$$= \chi^{(2)}\left[E_1^2 e^{-2i\omega_1 t} + E_2^2 e^{-2i\omega_2 t} + 2E_1E_2e^{-i(\omega_1+\omega_2)t} + 2E_1E_2^* e^{-i(\omega_1-\omega_2)t} + \text{c.c.}\right]$$

$$+2\chi^{(2)}[E_1E_1^* + E_2E_2^*]. \tag{3.5}$$

Each of these terms on the right side of Equation (3.5) corresponds to a second-order nonlinear process. The first two terms of the nonlinear polarization have frequency components, $2\omega_1$ and $2\omega_2$, at twice the frequencies of the input fundamentals. This process is called second harmonic generation (SHG), in which two photons of frequency ω are destroyed to create a photon at twice the frequency, 2ω, shown in Figure 3.2. It should be noted that second harmonic generation can occur with an incident electric field composed of only one frequency component, $\tilde{E}(t) = Ee^{-i\omega t} + \text{c.c.}$.

$$\tilde{P}^{(2)}(t) = \chi^{(2)}\tilde{E}(t)^2 \tag{3.6}$$

$$= \chi^{(2)}EE^* + (\chi^{(2)}E^2e^{-2i\omega t} + \text{c.c.}). \tag{3.7}$$

Other processes are also present in this nonlinear polarization, like sum frequency generation ($\omega_1 + \omega_2$, SFG), in which a photon is created at a frequency equal to the sum of the input frequencies. Similarly, a photon can be created at frequency equal to the difference

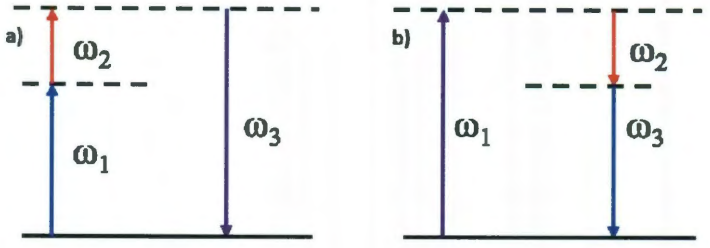

Figure 3.3 : Illustration of second-order nonlinear processes (a) SFG and (b) DFG. Different colors represent the relative frequency of the incident and generated photons [11].

of the input frequencies ($\omega_1 - \omega_2$). This process is called difference frequency generation (DFG). The SFG and DFG processes are shown in Figures 3.3a and 3.3b, respectively. The last term refers to optical rectification, in which a static field, with no time component, is created within the medium.

3.3 Third-order nonlinear optical processes

Third-order nonlinear optical properties are present in all crystal types (lowest observable nonlinear process in centrosymmetric crystals). Similar to the calculations presented in Section 3.2, the frequency components of these third-order nonlinear processes can be understood. If we consider an incident electric-field with three distinct electric field components, ω_1, ω_2, and ω_3, represented by

$$\tilde{E}(t) = E_1 e^{-i\omega_1 t} + E_2 e^{-i\omega_2 t} + E_3 e^{-i\omega_3 t} + \text{c.c.} \tag{3.8}$$

incident on a medium with nonlinear susceptibility $\chi^{(3)}$, the third-order nonlinear polarization is given by

$$\begin{aligned}
\tilde{P}^{(3)}(t) &= \chi^{(3)}\tilde{E}(t)^3 && (3.9)\\
&= \chi^{(3)}[E_1^3 e^{-3i\omega_1 t} + \{\text{other THG terms}\} && (3.10)\\
&\quad +3E_1E_1^*E_1e^{-i\omega_1 t} + \{\text{other SA}\} && (3.11)\\
&\quad +6E_1E_2E_3^*e^{-i(\omega_1+\omega_2-\omega_3)t} + \{\text{other FWM terms}\} + ...]. && (3.12)
\end{aligned}$$

Similar to the second-order processes observed at high input intensities, third-order processes include harmonic generation and sum/difference frequency generation. During third harmonic generation (THG), three photons of the same frequency are destroyed to create a photon at three times the frequency of the incident fundamental beam (Figure 3.4).

The third-order sum/difference frequency generation process is called four wave mixing (FWM), in which three waves of different frequencies mix (various combinations of created and destroyed input photons), to create a fourth wave whose frequency is equal to the sum and/or difference of the three input frequencies as shown in Figure 3.4a. It can be represented by the term

$$P^{(3)}(\omega_4) = 6\chi^{(3)}(\omega_4 = \omega_1 + \omega_2 - \omega_3)E(\omega_1)E(\omega_2)E^*(\omega_3) \qquad (3.13)$$

It can be seen from Equation (3.13) that the frequency terms must satisfy the frequency matching condition

$$\omega_4 = \omega_1 + \omega_2 - \omega_3 \Rightarrow \omega_3 + \omega_4 = \omega_1 + \omega_2 \qquad (3.14)$$

If we assume all of waves to be plane waves of the form

$$E(\omega_q) = A_q(\vec{r})E^{(i\vec{k}_q\cdot\vec{r}-\omega t)}, \text{ where } q = 1,2,3, \text{ and } 4 \qquad (3.15)$$

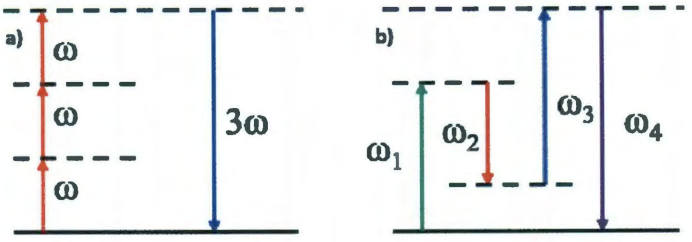

Figure 3.4 : Illustration of third-order nonlinear processes: (a) THG and (b) four wave mixing [11].

then we see that the third-order polarization is

$$P = 6\chi^{(3)} A_1 A_2 A_3^* e^{i(\vec{k}_1+\vec{k}_2-\vec{k}_3)\cdot\vec{r}} \tag{3.16}$$

and that the wavevectors must satisfy the phase matching criterion

$$k_4 = k_1 + k_2 - k_3 \Rightarrow k_3 + k_4 = k_1 + k_2. \tag{3.17}$$

All of the frequency and phase matching criteria must be satisfied in order for this process to take place.

In the degenerate four wave mixing (DFWM) case, where all four waves share the same frequency (degenerate), and two of the waves (called pump waves) are counter propagating, satisfying the equation

$$k_1 + k_2 = 0 \tag{3.18}$$

Then it can be shown that the induced polarization from Equation (3.16) becomes

$$P = 6\chi^{(3)} A_1 A_2 A_3^* e^{-i\vec{k}_3\cdot\vec{r}} \tag{3.19}$$

This term corresponds to an optical wave of complex amplitude, $A_1 A_2 A_3^*$, and wavevector, $-\vec{k}_3$, called the conjugate wave. This conjugate wave is identical to the incident wave everywhere, except for a reversed direction of propagation, and amplification in power, as shown in Figure 3.5.

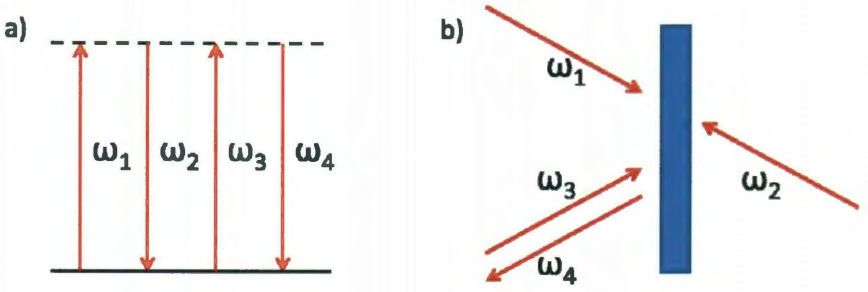

Figure 3.5 : Illustration of the degenerate four-wave mixing process. (a) Energy diagram. (b) Illustration of the DFWM process. Waves of frequency ω_1 and ω_2 act as pump waves. ω_4 is called the conjugate wave of ω_3 [11].

Another term that arises when examining the third-order polarization is

$$P^{(3)}(\omega_1) = 3\chi^{(3)}(\omega_1 = \omega_1 - \omega_1 + \omega_1)\,|E(\omega_1)|^2 E(\omega_1). \tag{3.20}$$

From this equation, we see that there is a part of the nonlinear polarization that influences the propagation of the fundamental frequency ω_1. This term describes the intensity dependent index of refraction, n_2. The index of refraction of any material is given by the equation below.

$$n \equiv n_0 + n_2 I \tag{3.21}$$

From Equation (3.20) we see that the effective (total) susceptibility for a material system is described by the relationship below

$$P(\omega_1) = \chi_{\text{eff}} E(\omega_1), \text{ where } \chi_{\text{eff}} = \chi^{(1)} + 3\chi^{(3)}\,|E(\omega)|^2 \tag{3.22}$$

The susceptibility is related to the index of refraction by the equation

$$n_2 = 1 + 4\pi\chi_{\text{eff}} \tag{3.23}$$

Thus, using Equations (3.21), (3.22), and (3.23) it can be shown that the intensity dependent

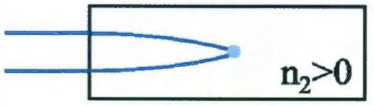

Figure 3.6 : In the nonlinear index of refraction process, the index of refraction depends on the intensity and causes self focusing [11].

index of refraction is defined by

$$n_2 = \frac{12\pi^2}{n_0^2 c}\chi^{(3)} \tag{3.24}$$

If we consider a general pulse shape, in which a beam is more intense at the center, we find that the index of refraction for a material is larger at the center of the beam, and thus, the material acts as a positive lens. The described process is called self focusing, seen in Figure 3.6.

The imaginary part of this complex nonlinear index of refraction is used to describe intensity dependent (saturable) absorption, β, in the equation below.

$$\beta = \frac{\beta_0}{1 + I/I_s} \tag{3.25}$$

3.4 Nonlinear Optical Susceptibility

The most important quantity in Equation (3.2) that we have not thoroughly covered so far is the nonlinear susceptibility, $\chi^{(n)}$. In general, $\chi^{(n)}$ is an $(n+1)$-th rank tensor representing both the polarization dependent nature of the optical interaction as well as the symmetries (or lack thereof) of the nonlinear material.

In order to investigate the complexities of the nonlinear susceptibility we will use the model of a classic harmonic oscillator with an extra nonlinear restoring force term. Since

second harmonic processes only take place in materials who lack inversion symmetry, we will apply our anharmonic model to a noncentrosymmetric medium.

The equation of motion for an electron in a noncentrosymmetric medium, which has a resonance frequency ω_0, excited by an intense electric field is given by

$$\frac{\partial^2 x}{\partial t^2} + 2\gamma\frac{\partial x}{\partial t} + \omega_0^2 x + ax^2 + bx^3 = -\frac{eE(t)}{m} \tag{3.26}$$

where we assume that the damping force is given by

$$F_{\text{damping}} = 2m\gamma\frac{\partial x}{\partial t} \tag{3.27}$$

and where a and b represent the strength of the second-order and third-order nonlinear contributions, respectively, to the restoring force, i.e.,

$$F_{\text{restoring}} = m\omega_0^2 x + max^2 + mbx^3. \tag{3.28}$$

Here the restoring force is represented by a Taylor series expansion of the restoring force in displacement x. Only the first three terms contribute to the overall restoring force.

This restoring force function corresponds to a potential energy of the form

$$U = -\int F_{\text{restoring}} dx = \frac{1}{2}m\omega_0^2 x^2 + \frac{1}{3}max^3 + \frac{1}{4}mbx^4. \tag{3.29}$$

From this relationship it can be seen that in the case of a centrosymmetric medium, where the potential must possess the symmetry $U(x) = U(-x)$, all of the odd (second-order contribution) terms in the potential would vanish.

In the case of third harmonic generations the applied optical field only has one frequency component,

$$E(t) = E(\omega)e^{-i\omega t}. \tag{3.30}$$

We express the displacement of the anharmonic oscillator as a perturbation series

$$x(t) = \underbrace{x^{(1)}}_{\alpha E(t)} + \underbrace{x^{(2)}}_{\alpha E^2(t)} + \underbrace{x^{(3)}}_{\alpha E^3(t)} + \ldots \tag{3.31}$$

where α is an expansion parameter that characterizes the strength of the perturbation.

By substituting Equation (3.31) into the equation of motion, we get

$$\frac{\partial^2 x^{(1)}}{\partial t^2} + \frac{\partial^2 x^{(2)}}{\partial t^2} + \frac{\partial^2 x^{(3)}}{\partial t^2} \tag{3.32}$$

$$-\frac{eE(t)}{m} = +2\gamma\frac{\partial x^{(1)}}{\partial t} + 2\gamma\frac{\partial x^{(2)}}{\partial t} + 2\gamma\frac{\partial x^{(3)}}{\partial t} \tag{3.33}$$

$$+\omega_0^2 x^{(1)} + \omega_0^2 x^{(2)} + \omega_0^2 x^{(3)} \tag{3.34}$$

$$+ \underbrace{a\left(x^{(1)} + x^{(2)} + x^{(3)}\right)^2}_{\text{only } ax^{(1)2} \text{ and } 2ax^{(1)}x^{(2)} \text{ have } E^2 \text{ and } E^3 \text{ dependence, respectively}} \tag{3.35}$$

$$+ \underbrace{b\left(x^{(1)} + x^{(2)} + x^{(3)}\right)^3}_{\text{only } bx^{(1)3} \text{ has } E^3 \text{ dependence}} \tag{3.36}$$

Each term of the same power E^n must satisfy the above relation independently. By sorting out these terms on the left and right sides we get the following relations:

$$\frac{\partial^2 x^{(1)}}{\partial t^2} + 2\gamma\frac{\partial x^{(1)}}{\partial t} + \omega_0^2 x^{(1)} = -\frac{eE(t)}{m} \tag{3.37}$$

$$\frac{\partial^2 x^{(2)}}{\partial t^2} + 2\gamma\frac{\partial x^{(2)}}{\partial t} + \omega_0^2 x^{(2)} + a x^{(1)2} = 0 \tag{3.38}$$

$$\frac{\partial^2 x^{(1)}}{\partial t^2} + 2\gamma\frac{\partial x^{(1)}}{\partial t} + \omega_0^2 x^{(1)} + 2a x^{(1)} x^{(2)} + b x^{(1)3} = 0 \tag{3.39}$$

The $x^{(1)}$ contribution is modeled by the classical harmonic oscillator whose solution is

$$x^{(1)}(t) = x^{(1)}(\omega) e^{-i\omega t} + \text{c.c.} \tag{3.40}$$

where

$$x^{(1)}(\omega) = \frac{-(eE/m)}{D(\omega)} \tag{3.41}$$

and $D(\omega) = \omega_0^2 - \omega^2 - 2i\omega\gamma$. Thus, it is seen that for an electron oscillating about a positive charge, the maximum displacement from equilibrium occurs when the incident electric field has a frequency $\omega = \omega_0$. Because we chose the incident electric field to only have one

frequency component, the only second-order processes that can take place are second harmonic generation and optical rectification. Let us look at the second harmonic generation case. Looking at the second-order equations of motion, we should choose a steady state solution of

$$x^{(2)}(t) = x^{(2)}(\omega)e^{-i2\omega t} + \text{c.c.} \tag{3.42}$$

where

$$x^{(2)}(2\omega) = \frac{-(eE/m)^2}{D(2\omega)D^2(\omega)}. \tag{3.43}$$

Similarly for the third harmonic case, the steady state solution should be

$$x^{(3)}(t) = x^{(3)}(\omega)e^{-i3\omega t} + \text{c.c.} \tag{3.44}$$

where

$$x^{(3)}(3\omega) = \frac{2a^2(eE/m)^3}{D(3\omega)D(2\omega)D^3(\omega)} + \frac{b(eE/m)^3}{D(3\omega)D^3(\omega)}. \tag{3.45}$$

As defined before, the linear susceptibility, $\chi^{(1)}(\omega)$, is defined as

$$P^{(1)}(\omega) = \chi^{(1)}(\omega)E(\omega) \tag{3.46}$$

and the linear contribution for the polarization of N atoms is given by

$$P^{(1)}(\omega) = -Nex^{(1)}(\omega) \tag{3.47}$$

thus, it can be shown that

$$\chi^{(1)}(\omega) = \frac{N(e^2/m)}{D(\omega)}. \tag{3.48}$$

From this equation, we see that when we have an electric field with a frequency component that is equal to the resonant frequency within the material, we attain a very large value of the linear susceptibility.

For the nonlinear susceptibilities given by SHG and THG, $\chi^{(2)}(2\omega)$ and $\chi^{(3)}(3\omega)$ are defined as

$$P^{(2)}(2\omega) = \chi^{(2)}(\omega)E^2(\omega) \text{ and } P^{(3)}(3\omega) = \chi^{(3)}(\omega)E^3(\omega) \tag{3.49}$$

and the nonlinear contribution for the polarization of N atoms is given by

$$P^{(2)}(\omega) = -Nex^{(2)}(2\omega) \text{ and } P^{(3)}(\omega) = -Nex^{(3)}(3\omega) \tag{3.50}$$

Thus, the nonlinear susceptibilities have the scalar form

$$\chi^{(2)}(2\omega) = \frac{Na(e^3/m^2)}{D(2\omega)D^2(\omega)} \tag{3.51}$$

and

$$\chi^{(3)}(3\omega) = \frac{Ne^4}{m^3}\left(\frac{2a^2}{D(3\omega)D(2\omega)D^3(\omega)} + \frac{b}{D(3\omega)D^3(\omega)}\right) \tag{3.52}$$

From Equations (3.51) and (3.52), we can see that these two susceptibilities attain a maximum when the fundamental (ω), second (2ω) harmonic, or third harmonic (3ω) are on resonance with a transition within the material.

3.5 Symmetries of the Nonlinear Susceptibility

[48]

It is also worth noting some of the symmetry properties of the nonlinear susceptibility. The third-order susceptibility for a four wave interaction, $\omega_p = \omega_m + \omega_n + \omega_o$, is defined as

$$P_i(\omega_m + \omega_n + \omega_o) = \sum_{jkl}\sum_{(mno)} \chi^{(3)}_{ijkl}(\omega_p, \omega_m, \omega_n, \omega_o) E(\omega_m)E(\omega_n)E(\omega_o) \tag{3.53}$$

Here $\chi^{(3)}$ is represented as a fourth-rank tensor with 3888 different tensor elements (24 tensors, 81 cartesian components). This number becomes significantly smaller after using certain symmetry properties.

1. Intrinsic Permutation Symmetry

$$\begin{aligned}\chi^{(3)}_{ijkl}(\omega_p;\omega_m,\omega_n,\omega_o) &= \chi^{(3)}_{ikjl}(\omega_p;\omega_n,\omega_m,\omega_o)\\ &= \chi^{(3)}_{iklj}(\omega_p;\omega_n,\omega_o,\omega_m)\end{aligned}$$

$$= \chi^{(3)}_{ilkj}(\omega_p; \omega_o, \omega_n, \omega_m), \tag{3.54}$$

The susceptibility is invariant under all permutations of the last 3 indices and frequency arguments. Both the indices and the frequencies must be changed simultaneously.

2. Full Permutation Symmetry

$$\begin{aligned} \chi^{(3)}_{ijkl}(\omega_p; \omega_m, \omega_n, \omega_o) &= \chi^{(3)}_{jikl}(-\omega_m; -\omega_p, \omega_m, \omega_o) \\ &= \chi^{(3)}_{iklj}(-\omega_n; \omega_m, -\omega_p, \omega_o) \\ &= \chi^{(3)}_{ilkj}(-\omega_o; \omega_m, \omega_n, -\omega_p), \end{aligned} \tag{3.55}$$

The susceptibility is invariant under all permutations. This principle applies to nonresonant media, where all optical frequencies appearing in the formula for the susceptibility are removed far from the transition frequencies of the medium. Both the indices and the frequencies must be changed simultaneously. When interchanging the first index with any of the latter 3 indices, then you must change the sign.

3. Klienman Symmetry

$$\begin{aligned} \chi^{(3)}_{ijkl}(\omega_p; \omega_m, \omega_n, \omega_o) &= \chi^{(3)}_{jikl}(\omega_p; \omega_m, \omega_n, \omega_o) \\ &= \chi^{(3)}_{iklj}(\omega_p; \omega_m, \omega_n, \omega_o) \\ &= \chi^{(3)}_{ilkj}(\omega_p; \omega_m, \omega_n, \omega_o), \end{aligned} \tag{3.56}$$

In the lower frequency limit, under nonresonant conditions, the nonlinear susceptibility is invariant under permutations of the indices. This also holds true for harmonic generation where $\omega_m = \omega_n = \omega_o = \omega$.

4. Spatial Symmetry

There are spatial symmetries that are given by point symmetry class of the medium. The point class for SWCNTs will be discussed in Chapter 6 of this thesis.

Chapter 4

Prior Nonlinear Optical Studies of Single-Wall Carbon Nanotubes

As described in Chapter 2, linear optical properties of SWCNTs have been extensively studied in the last two decades. However, their nonlinear optical properties largely remain unexplored, although some theoretical studies exist. In this chapter, some of the experimental and theoretical studies are reviewed, both on second-order (Section 4.1) and third-order (Sections 4.2 and 4.3) nonlinear optical processes in SWCNTs.

4.1 Second-Order Nonlinear Optical Processes in Carbon Nanotubes

Second-order processes within carbon nanotubes have not been thoroughly investigated, primarily because of the inversion symmetry of the zigzag ($m = 0$) and armchair ($m = n$) nanotubes along the nanotube axis. Chiral nanotubes do not possess intrinsic inversion symmetry, which suggests that $\chi^{(2)}$ should be finite, but there still have not been significant contributions to the study of its second-order processes. The co-existence of right-handed and left-handed chiral SWCNTs with the same chirality indices (n,m) in macroscopic SWCNT samples usually lead to cancellation of $\chi^{(2)}$ processes.

However, Guo *et al.* theoretically investigated the features and magnitude of $\chi^{(2)}$ of chiral SWCNTs [12]. In this theoretical study, a local density approximation plus independent-particle approach was used for describing the electronic band structure and density of states, as well as linear and nonlinear optical susceptibilities. After deriving the second-order

nonlinear optical susceptibility, Guo *et al.* investigated second harmonic generation in five different types of carbon nanotubes as shown in Figure 4.1. This figure takes into consideration the 1D chiral symmetry of nanotubes, and thus, only two elements out of the eighteen elements of the second-order susceptibility tensor are nonzero. These two nonzero elements are $\chi^{(2)}_{xyz}$ and $\chi^{(2)}_{yzx}$, and their relationship is $\chi^{(2)}_{xyz} = -\chi^{(2)}_{yzx}$; thus, only $\chi^{(2)}_{xyz}$ is shown. From these calculations, Guo *et al.* showed that the absolute value of $\chi^{(2)}$ is expected to be ten times greater than that of GaAs, or 15×10^{-5} esu when the photon energy is resonant with an interband optical transition, illustrated in Figure 4.2. It can be seen from these figures that the absolute value of $\chi^{(2)}$ gets smaller as one moves from the (4,2) to the (10,5) nanotube. This is because as the diameter of these tubes becomes larger, the absolute value of $\chi^{(2)}$ approaches zero, or that of graphene. There have only been two experiments that have claimed to have observed second-order nonlinear optical processes in carbon nanotubes, both being second harmonic generation investigations [13, 20]. The difficulty in measuring second-order processes in SWCNTs comes from inversion symmetry mentioned above. Not only do the armchair and zig-zag tubes possess inversion symmetry, but a sample with an ensemble of left and right-handed chiral tubes will have quasi-inversion symmetry.

Su *et al.* experimentally measured resonant second harmonic generation from aligned SWCNTs [13]. The carbon nanotubes were grown by pyrolysis of tripropylamine (TPA) in the channels of the host single crystalline aluminophosphate (AFI) zeolite. Through Raman scattering, it was determined that only three types of nanotubes were present in the sample, (5,0), (3,3), and (4,2) nanotubes, all of diameter 0.4 nm. In order to see the second harmonic signal, the overall macroscopic symmetry had to be broken, and thus, there was an excess of either left or right-handed tubes present in the sample. Su *et al.* observed a resonant enhancement in the second harmonic signal at the expected E_{11} transition en-

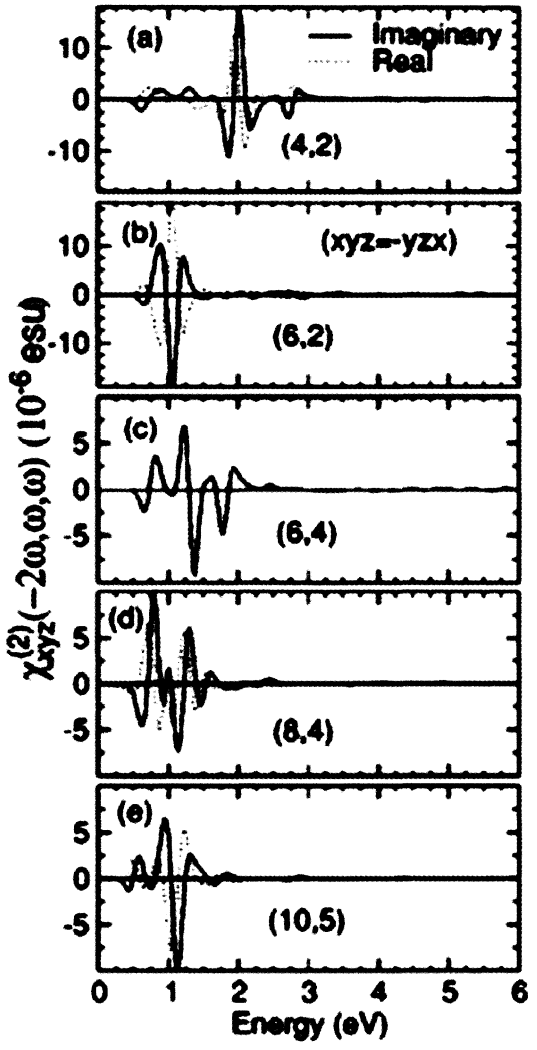

Figure 4.1 : Theoretical calculations of the real and imaginary second-order nonlinear susceptibility in chiral nanotubes [12].

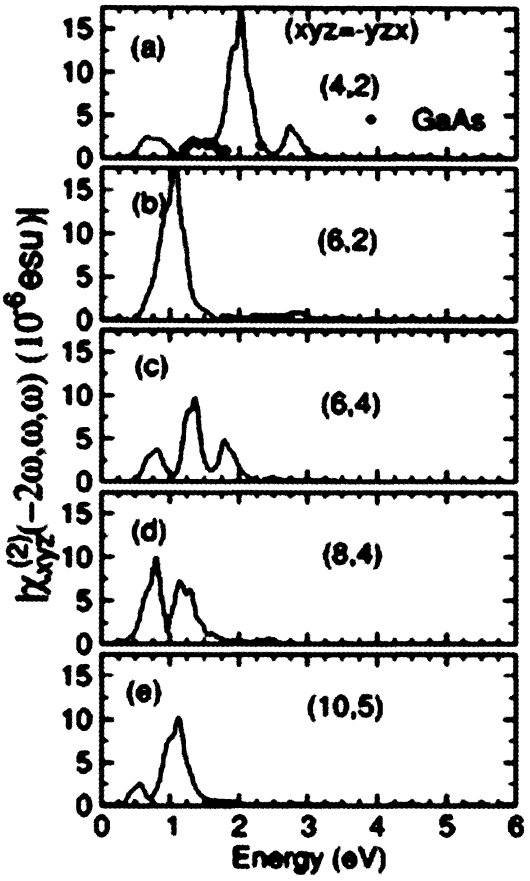

Figure 4.2 : Theoretical calculations of the absolute value of second-order nonlinear susceptibility in chiral nanotubes, with measured values of GaAs (diamonds). When on resonance with the E_{11} transition, the absolute value is ten times that of GaAs [12].

ergy, measuring 2.1×10^{-6} esu for the absolute value of $\chi^{(2)}$, which is in good agreement with the prediction by Guo *et al.* [12]. Polarization dependent measurements were also conducted, to confirm that the theoretically predicted tensor elements were indeed contributing to the overall $\chi^{(2)}$ signal as shown in Figure 4.3. The theoretical fit shown in Figure 4.3 calculates the second-order susceptibility, considering contributions from the $\chi^{(2)}_{xyz}$ and $\chi^{(2)}_{yzx}$ tensor elements. A similar approach was used in our experiments to investigate the nonzero tensor elements of $\chi^{(3)}$ for SWCNTs (see Chapter 7).

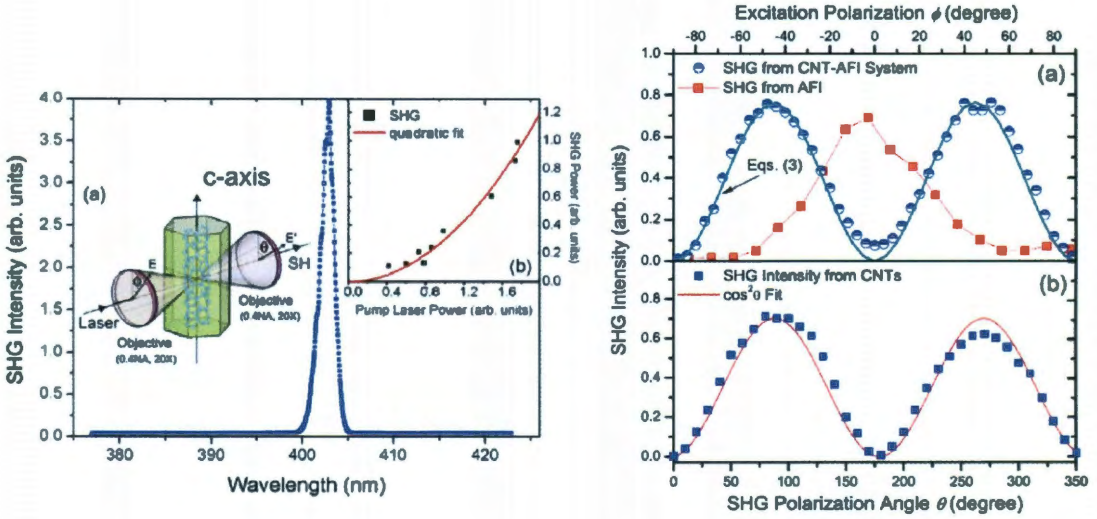

Figure 4.3 : (a) Second harmonic generation produced from 800 nm fundamental. (b) Power dependence of SHG relative to the input fundamental. Theta dependence of the (c) nanotubes with reference, reference, and (d) extracted nanotube contribution [13].

4.2 Third-Order Nonlinear Optical Processes in Carbon Nanotubes: Theoretical Studies

The third-order susceptibility is the lowest-order nonlinear property that happens in all materials, including zig-zag and armchair SWCNTs. Theoretically, the third-order nonlinear optical properties of nanotubes have been investigated by several groups [14,49–53]. These groups use different approaches for theoretically calculating the absolute value of $\chi^{(3)}$, for various nonlinear optical effects.

Margulis *et al.* used the Ajiki-Ando [14] model to calculate the carbon nanotube band structure [54]. The effective-mass approximation used within this model has had success in explaining a number of important physical aspects of nanotubes. They then used the Genkin-Mednis [55] approach to calculate the complex third order nonlinear-optical susceptibility, $\chi^{(3)}$, for several third-order polarization effects. This approach considers that

only the interband and a combined interband/intraband motion of electrons contribute to the nonlinear optical response. Through this approach, only the highest valence band and lowest conduction band contribute to the expression for $\chi^{(3)}$ (two-band approximation). From these calculations they obtained relationships for third harmonic generation, nonlinear index of refraction, two-photon absorption, and the DC optical Kerr effect in carbon nanotubes.

From their calculation of $\chi^{(3)}$, in the case of nonresonant third-order processes, the absolute value of $\chi^{(3)}$ is given by

$$\chi^{(3)} = \frac{4}{5}\frac{(3ed_t)^4}{\pi^2\gamma_0^3}, \tag{4.1}$$

where γ_0 is the $\vec{k}\cdot\vec{p}$ interaction parameter, which is directly proportional to the transfer integral, γ between π states ($\gamma_0 = \sqrt{3}\gamma a/2$, where a is the lattice constant of a graphene sheet). Using this equation it can be shown that a SWCNT whose diameter is 5.5 Å, has a nonresonant $\chi^{(3)}$ equal to 3×10^{-9} esu. It can also be seen that the $\chi^{(3)}$ of the tube has a d_t^4 dependence on the diameter of the tube, and thus, $\chi^{(3)}$ should depend drastically on the size of the tube. This formulation must break down in the graphene limit ($d_t \to \infty$), since $\chi^{(3)}$ is not infinite for graphene.

The results of the third harmonic generation calculations for the three different semiconducting nanotubes, (13,0), (16,0) and (19,0), are presented in Figure 4.4. These calculated spectra demonstrate that the power of the third harmonic exhibits a large enhancement at the pump frequency which corresponds to one-third of the band-gap energy. The comparison of the curves in Figure 4.4 also shows that the efficiency of the third harmonic generation can be considerably increased by varying the diameter of the nanotubes. Thus, for the (19,0) nanotube, $d_t = 1.488$ nm and $E_g = 0.58$ eV, the magnitude of $\chi^{(3)}_{THG}$ under the three-photon resonance conditions achieves the value 1.29×10^{-6} esu, which is two orders of magnitude larger than that under nonresonant conditions.

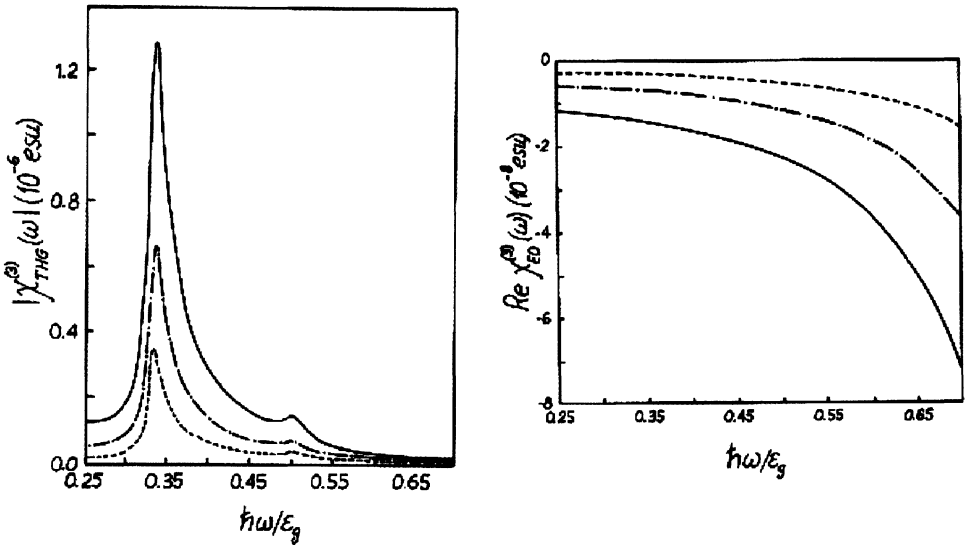

Figure 4.4 : Theoretical calculations of the absolute value of third order nonlinear susceptibility, for (a) THG and (b) optical Kerr effect in nanotubes [14].

The calculations of both the intensity-dependent index of refraction and the two-photon absorption show that the nonlinear refractive index as large as $2 \times 10^8\,\mathrm{cm^2W^{-1}}$ can be achieved in a region where the two-photon absorption is small, as shown in Figure 4.5. Thus, SWCNTs are of interest for utilizing them in a variety of ultrafast-frequency-conversion devices based on third-order processes. For all of these effects, $\chi^{(3)}$ is significantly enhanced under on-resonance conditions. From these calculations, Margulis *et al.* reported an absolute value on the order of 10^{-8} to 10^{-6} esu for $\chi^{(3)}$ in carbon nanotubes, depending on whether the incident light is nonresonant or resonant, respectively ($n_2 \approx 10^{-8}\,\mathrm{cm^2/W}$ for the nonlinear refractive index, and $\beta \approx 10^{-5}$ cm/W for the two-photon absorption coefficient).

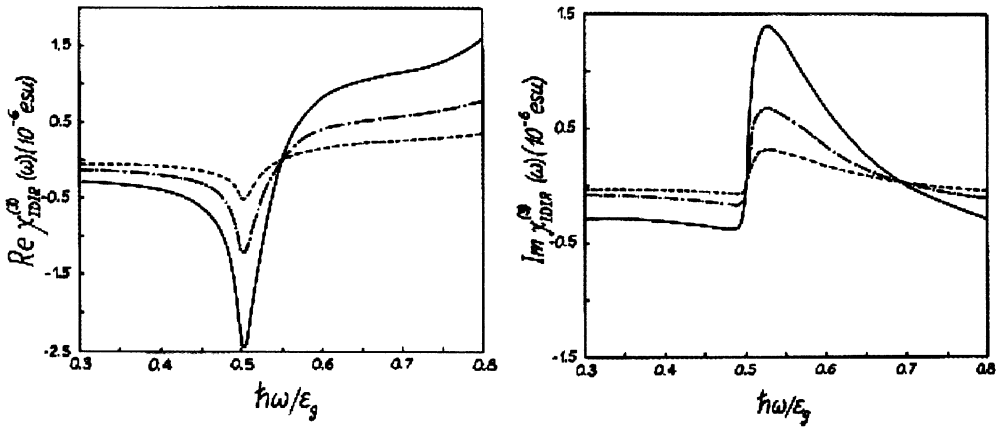

Figure 4.5 : Theoretical calculations of the (a) nonlinear index of refraction and (b) the two photon absorption coefficient [14].

4.3 Third-Order Nonlinear Optical Processes in Carbon Nanotubes: Experimental Studies

Several groups have observed third-order nonlinear optical properties from carbon nanotubes [16–20, 56–69]. The optical limiting properties are of particularly great interest, because of their potential applications [16, 17, 56–60]. Vivien *et al.* used the z-scan method to measure the optical limiting properties of carbon nanotubes, specifically the nonlinear refractive index and the nonlinear absorption of the material [16]. By moving the sample along the propagation z-direction of a focused Gaussian beam, the focal spot position and far field intensity of the Gaussian beam can change (Figure 4.6). In the far field, if a small aperture is placed before the detector, the intensity measured at the detector can change due to the change in focal spot position, caused by the nonlinear index of refraction (which leads to self-focusing of the Gaussian beam). By measuring this change in intensity, a value for the nonlinear index of refraction, n_2, can be found. If an open aperture is placed at the entrance to the detector, an intensity variation can be observed in the far field.

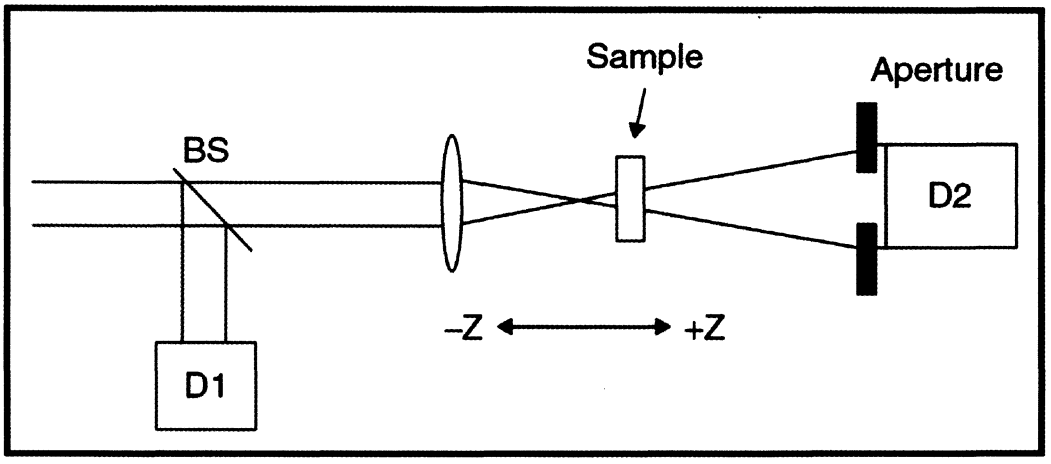

Figure 4.6 : Z-scan schematic for experimentally measuring the nonlinear index of refraction, and nonlinear absorption [15].

This change in intensity is due to nonlinear scattering and absorption, β. As mentioned before, the absolute value of $\chi^{(3)}$ can be calculated from β ($\Im\chi^{(3)}$) and n_2 ($\Re\chi^{(3)}$). In Figure 4.7, Vivien measured the z-scan transmittance for low/high powers and for closed/open apertures. Experimentally, values of $n_2 \approx -10^{-12}$ cm^2/W and $\beta \approx 5 \times 10^{-8}$ cm/W were obtained. These values correspond to $\chi^{(3)} \approx 10^{-10}$ esu, which is an order of magnitude lower than the predicted nonresonant value presented in Margulis *et al.*'s theory [14]. Through similar techniques, other experimentally measured values of $\chi^{(3)}$ have been on the order of $10^{-10} - 10^{-12}$ esu in the nonresonant configuration [56, 57].

In an experiment by Tatsuura *et al.*, the measured nonlinear absorption was resonantly enhanced by the transitions with energies equal to the bandgap [17]. This transition is represented as a peak in the SWCNT absorption spectrum (Figure 4.8a, solid line). The nonlinear absorption was measured via the z-scan method, where the incident pump energy was 0.94 eV, which is resonant with the linear absorption peak (Figure 4.8b). The calculated $\chi^{(3)}$ was found to be 8.5×10^{-6} esu, which was two orders of magnitude larger than that of

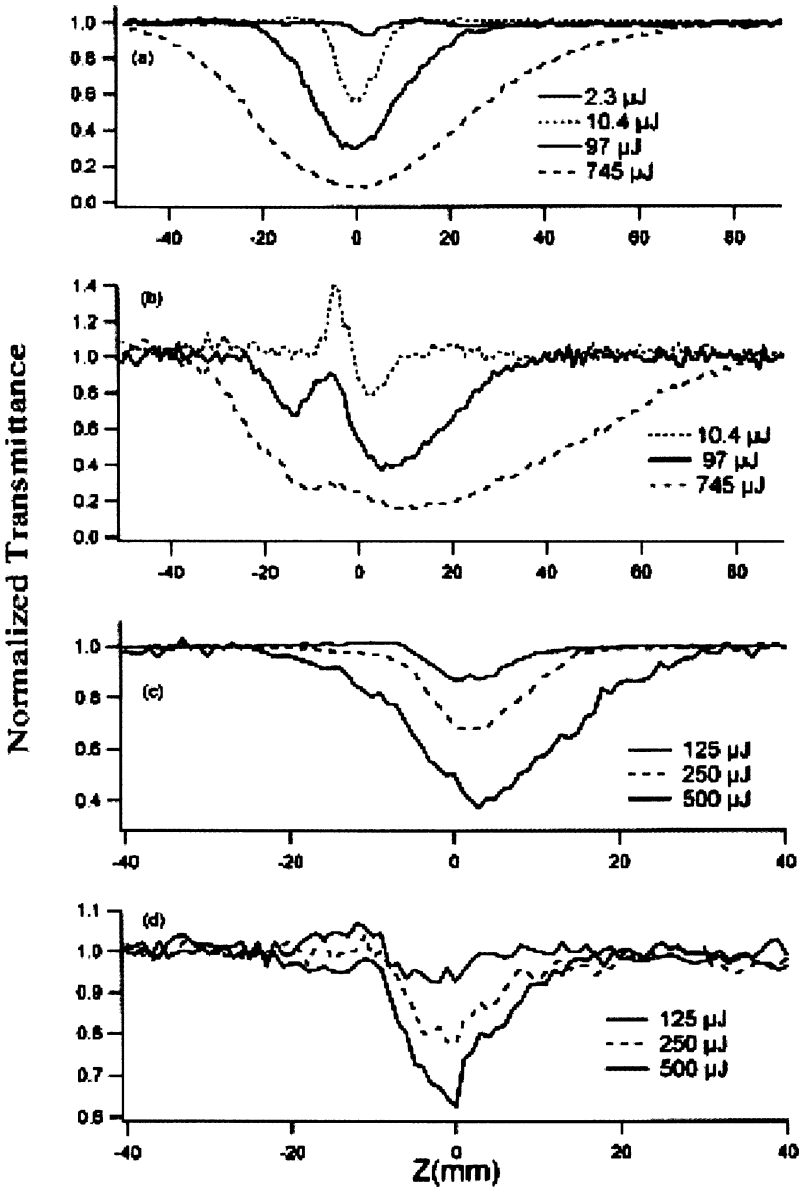

Figure 4.7 : Z scan measurements at different input energies for (a) 532 nm, large aperture; (b) 532 nm, small aperture; (c) 1064 nm, large aperture; and (d) 1064 nm, small aperture [16].

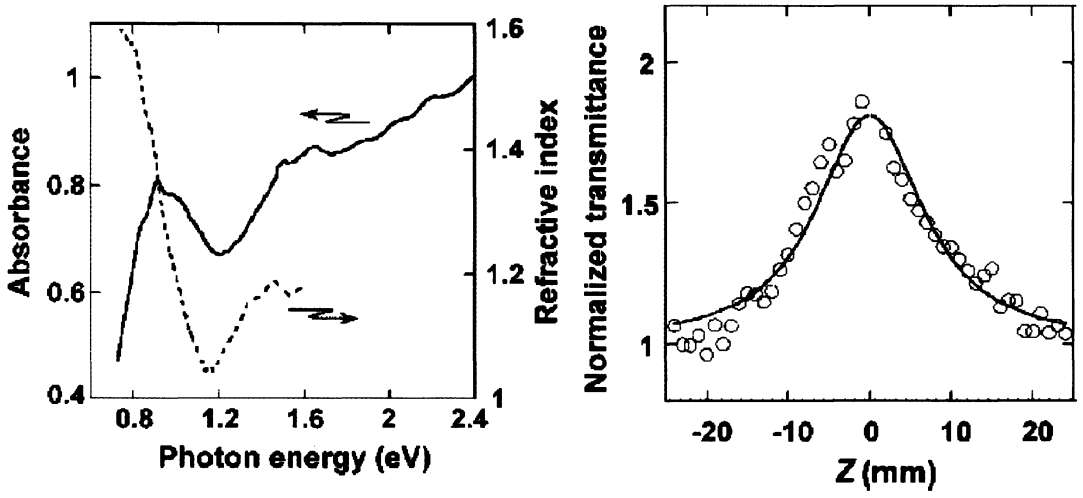

Figure 4.8 : (a) Absorption (solid line) and index of refraction (dashed line) of the spray coated SWCNT film. (b) Normalized transmittance of the of the resonant fundamental pump [17].

the measured nonresonant values, as predicted by Margulis *et al.* [14].

Another third-order process that has been researched by a few groups has been four wave mixing (FWM) in SWCNTs [18, 68, 69]. Kim *et al.* used a specific type of FWM process called coherent anti-Stokes scattering (CAS) microscopy [18]. In this technique, an ultrafast pump (ω_{pump}) and Stokes (ω_s) pulse pair excited the SWCNT, and radiation was detected at the anti-Stokes frequency ($\omega_{as} = 2\omega_{pump} - \omega_s$). The strength of the measured signal changed with the temporal overlap of the pump and Stokes pulse, and with the resonant position of the pump. The intensity of the measured coherent anti-Stokes signal also changed with the orientation of the carbon nanotube axis, relative to the polarization of the pump, showing a $\cos^6\phi$ dependence, shown in Figure 4.9, which could lend some insight into the nonzero tensor elements of $\chi^{(3)}$.

Another experimental study, done on four wave mixing, by Lui *et al.*, suggests that

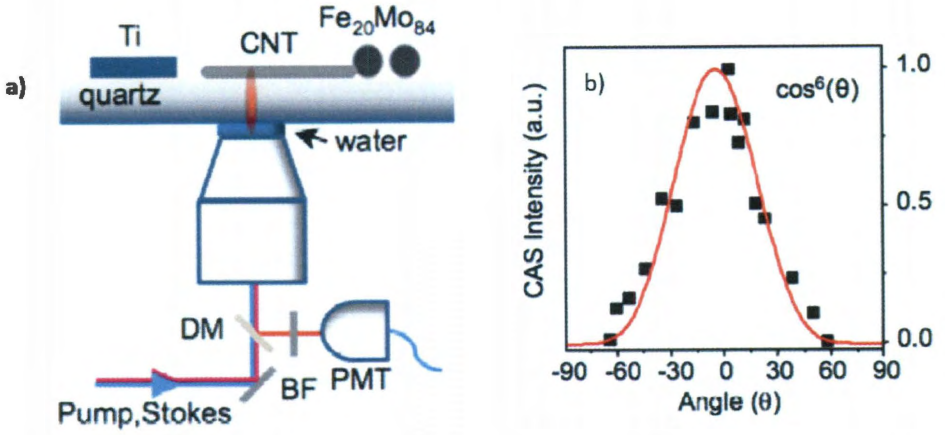

Figure 4.9 : (a) Schematic of fourwave mixing experiment; (b) Orientation dependence of the coherent anti-stokes signal [18].

there are other nonzero $\chi^{(3)}$ tensor elements that contribute to the overall $\chi^{(3)}$ [64]. The paper demonstrates through measurements that not only does the dominant $\chi^{(3)}_{zzzz}$ (all of the incident electric fields are polarized along the direction of conjugation, z) tensor component contribute to the overall $\chi^{(3)}$ signal, but there is some contribution from weaker tensor components. In the nonresonant case, these weaker tensor components are measured to have $\sim$1/3 of the intensity of the dominant tensor component.

There have only been two experiments reported for third harmonic generation in carbon nanotubes:

Stanciu *et al.* observed third harmonic generation in multi-wall carbon nanotube films (deposited by drying ethanol suspensions on silicon substrates), which was spectrally resolved by a monochromator at the expected third harmonic wavelength [19]. The intensity of the third harmonic, however, did not obey the critical power dependence that third-order processes have with the fundamental intensity, $I_{3\omega} = I_{\omega}^3$ (Figure 4.10). Thus, only qualita-

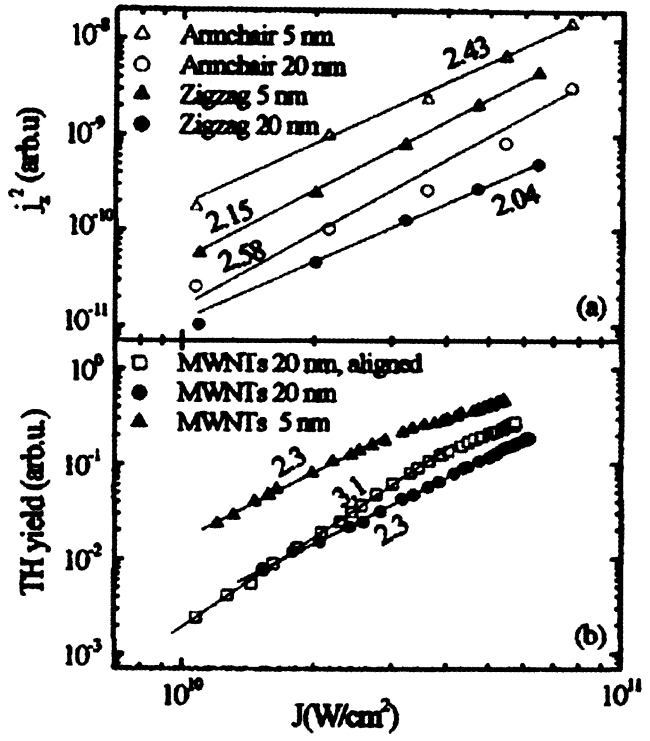

Figure 4.10 : Intensity dependence of the measured third harmonic signal versus the incident fundamental, where the the power, p, in the relationship $I_{3\omega} \propto I_{3\omega}^{p}$ is given. Bending in this data suggests that saturation of the third harmonic signal is possible [19].

tive data was given on the observation of the third harmonic.

Dominicis *et al.* also performed a third harmonic generation experiment on SWCNTs prepared via a catalyst-free method [20], and presented some power dependence data, as seen in Figure 4.11. The third harmonic observed in this paper was performed under resonant conditions, but the absolute value of $\chi^{(3)}$ was not quoted.

Thus, there have not been any studies that experimentally measure the absolute value of $\chi^{(3)}$ for carbon nanotubes via third harmonic generation in any wavelength range. There have also not been any investigations into the relevant $\chi^{(3)}$ tensor elements that contribute to the overall $\chi^{(3)}$ signal.

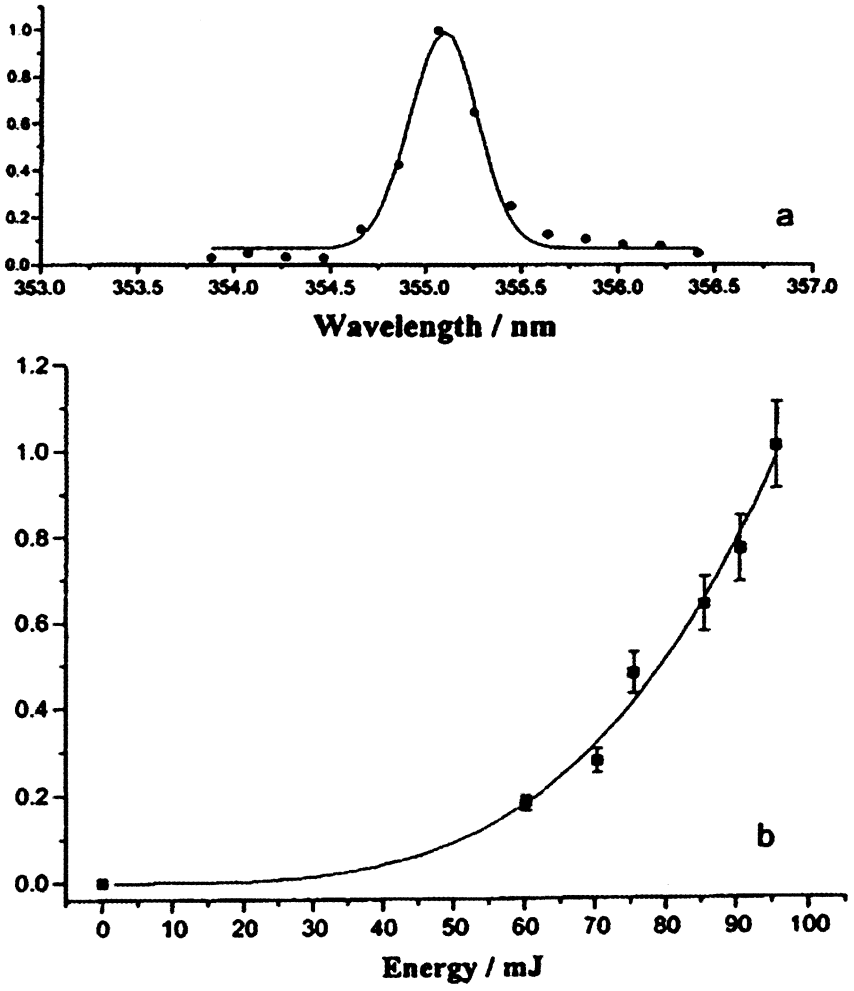

Figure 4.11 : (a) Spectrally resolved resonantly enhanced third harmonic signal (λ_{fund} = 1064 nm). (b) The yield of the third harmonic as a function of the fundamental [20].

Chapter 5

Experimental Procedure

5.1 Highly Aligned SWCNT Sample Preparation and Characterization

There are many types of carbon nanotube samples that are used for optical experiments. Researchers have used solutions, films, as well as individual nanotubes for measurements, all of which have their advantages and disadvantages. In this work, we use highly aligned SWCNT films on sapphire. The highly aligned carbon nanotube carpets are grown via placing a catalyst-lined substrate in a chemical vapor deposition reactor [21]. The lines of catalysts are separated by a distance of 50 μm, and the self-supporting carbon nanotubes are grown vertically to a height specified by growth time, as shown in Figure 5.1. The vertically aligned carpet is then separated from the catalyst substrate via a wet or dry etching process, to break the Fe-C bonds. Once the SWCNTs have been lifted, they easily adhere to any substrate surface, creating a horizontally aligned film of SWCNTs with little to zero overlap with the adjacent rows, depending on the initial growth height, as shown in Figure 5.1.

The SWCNTs in the samples are highly aligned, as shown in Figure 5.2, where the highly aligned nanotube film acts as a perfect polarizer for terahertz light [22, 23]. In this experiment, linearly polarized terahertz radiation is incident on the highly aligned SWCNT film. When the film is aligned perpendicular to the polarization of the terahertz radiation, there is zero absorption from the film. However, when the SWCNTs are parallel to the terahertz polarization, the absorption is finite and large, demonstrating a large absorption

Figure 5.1 : (a) SEM image of vertically aligned SWCNT carpets; (b) SEM image of horizontally aligned SWCNT film after transfer to substrate. Sample shows minimal overlap [21].

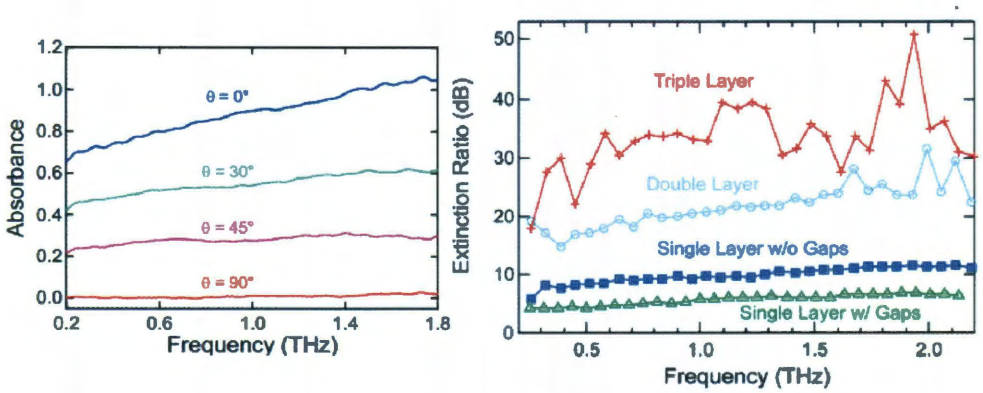

Figure 5.2 : Terahertz absorption anisotropy for highly aligned SWCNT film on sapphire. The figure on the left shows the absorption versus carbon nanotube angle. When the nanotubes are aligned parallel to the incident terahertz radiation, the absorption is finite. There is no absorption when the nanotube axis is perpendicular to the incident electric field [22]. The figure on the right shows the extinction ratio of single, double, and triple-layer SWCNT films [23].

anisotropy from the highly aligned film.

5.2 Experimental Setup for Harmonic Generation

5.2.1 Overview

In these experiments harmonic generation in samples with highly aligned SWCNTs was measured. The spectra of the harmonic signal were measured with a detector at the exit of a monochromator, and the orientation dependence of this harmonic signal was also measured, relative to a linearly polarized fundamental. A schematic of the experimental setup is shown in Figure 5.3. Intense mid-infrared light pulses with a pulse-width of 300 fsec and a repetition rate of 1 kHz, from a Ti:Sapphire-pumped optical parametric amplifier (OPA), served as the fundamental source. This mid-infrared light passed through a series of long-pass filters to remove any unwanted light from the OPA. Most of the light passed through a 1-mm thick CaF_2 window, which served as a beam splitter (97:3), and was incident on the sample. The small portion of reflected light served as a reference. The harmonic signal, generated in the sample, passed through a linear polarizer to measure the third harmonic signal parallel and perpendicular to the incident fundamental field. The linearly polarized third harmonic passed through a monochromator, which served as a filter that only passed the third harmonic signal. The signal was measured with a photomultiplier tube (PMT). The sample was mounted on a rotational mount for orientation dependent measurements.

5.2.2 Chirped Pulse Amplifier and Optical Parametric Amplifier

Light at the fundamental frequency was produced from a Quantronix Optical Parametric Amplifier, which was pumped by a Clark-MXR Chirped Pulse Amplifier (CPA). The CPA is made up of three different lasers. First, you have the seed laser pulse. The seed laser pulse is a low intensity, short pulse that is emitted from an oscillator laser. The seed pulse is then stretched (chirped) using a pair of gratings and sent through an optically pumped gain

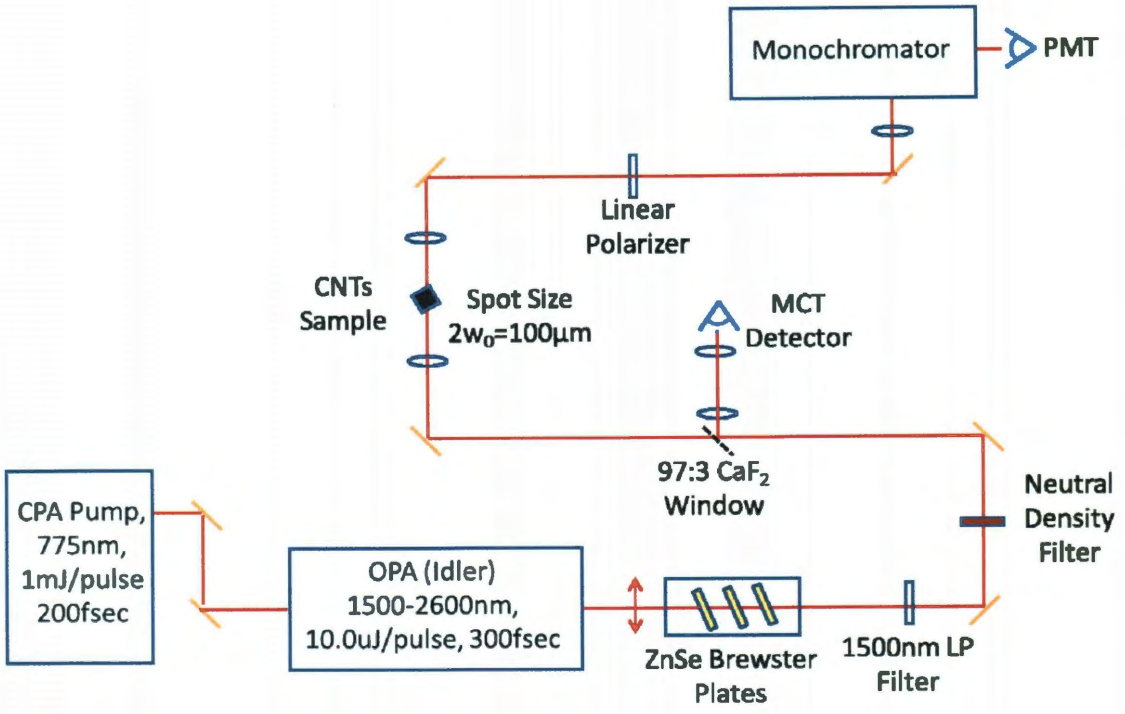

Figure 5.3 : Experimental setup for harmonic generation.

medium (Ti:Sapphire). The second laser is a high power Q-switched neodymium-doped yttrium aluminium garnet (Nd:YAG) laser, whose frequency ($\lambda = 1064$ nm) is doubled using a Lithium Triborate (LBO) crystal. This laser pumps the gain medium. The stretched seed laser pulse oscillates back and forth through the gain medium, within the regenerative amplifier cavity, creating an intense pulse. Lastly, this stretched pulse is compressed using a pair of gratings, to create ultra-intense (1 mJ/pulse), ultra-short ($\sim$150 fsec) pulses (Figure 5.4).

The CPA pumps the optical parametric amplifier (OPA). This pump photon passes through a crystal and is divided into two photons, through a second-order nonlinear optical process called optical parametric generation. The OPA uses a barium borate (BBO)

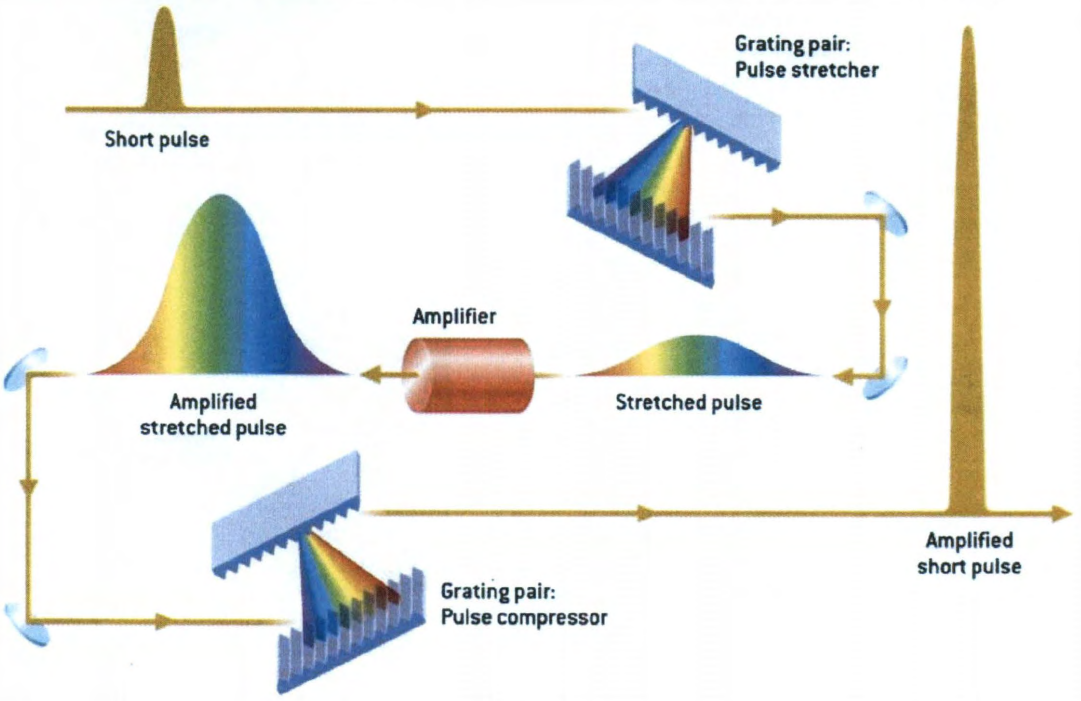

Figure 5.4 : Schematic of a chirped pulse amplifier. A low-intensity, short pulse is stretched, amplified, and compressed into a high-intensity, ultra-short pulse [24].

crystal, to create two pulses (signal and idler) whose sum total photon energy is equal to the energy of the pump. By changing the orientation or temperature of the crystal, the signal and idler wavelengths become widely tunable over a range from 1.2 to 2.7 μm. These beams again pass through the optically pumped crystal and are amplified. The signal and idler pulses are then propagated through a selection of nonlinear mixer crystals, which make the OPA source widely tunable over 0.3 μm to 20 μm, with pulse energies ranging from 1 μJ to 100 μJ, and pulse width of $\approx$ 300 fsec.

5.2.3 Detectors

To measure the intensity of the generated harmonic signal, a Hamamatsu R928 photomultiplier tube (PMT) was used. The optimal detectivity range for this detector is 185 to 900 nm, dependent on the ability of the incident photon to eject an electron from the photocathode material (photoelectric effect is more efficient with high energy photons in the ultraviolet, visible, and near-infrared). Thus, this detector would not see any scattered signal or idler fundamental (1.2 to 2.7 μm). The ejected electrons are directed by the focusing electrode toward the electron multiplier, where electrons are multiplied by the process of secondary emission. In this secondary emission process, one ejected electron at the cathode can turn into millions by the time it reaches the anode, resulting in a sharp current pulse, which makes it possible to count a single photon using this system.

To measure the intensity of the fundamental, a liquid nitrogen cooled mercury cadmium telluride (MCT) detector was used, whose optimum detectivity range is from 1.5 to 12 μm. The detection range of this photovoltaic device is dependent on the bandgap of the material. In this detector, when a photon is incident on the active material, an electron is excited across the bandgap, leaving a hole. The holes move toward the anode, and electrons toward the cathode, and a photocurrent is produced. Because more photons are necessary to create this photocurrent, this detector tends to be much less sensitive than the PMT, but it does allow for detection in the visible, near and mid-infrared regions.

5.2.4 Lock-in Amplifier

Both the third harmonic and reference signals were measured using a lock-in amplifier. The lock-in amplifier takes the input signal and multiplies it by the reference signal (TTL signal from CPA), both of the same frequency and integrated over a time longer than the frequency, delivering an averaged DC signal (slowly varying AC signal). If the signal is out

of phase with the reference, then that can also be determined using the lock-in amplifier. Any component (noise) that is not of the same frequency as the signal has an average value of zero, allowing for an excellent signal to noise ratio, when using a lock-in.

5.2.5 Filters

A series of ZnSe plates oriented at Brewster's angle served as the filter for the vertically polarized signal and horizontally polarized idler exiting the OPA. The Fresnel equations predict that light with the p polarization (electric field polarized in the same plane as the incident ray and the surface normal) will not be reflected if the angle of incidence is $\theta_B = \tan^{-1}(n_2/n_1)$, where θ_B is the Brewster angle and n_1 and n_2 are the indices of air and ZnSe, respectively. Thus, by using this crystal, separation of the signal and idler is possible.

A 1500 nm long-pass filter was used to filter out any of the signal or pump (775 nm) wavelengths. A silicon substrate ($E_g = 1.11\,\text{eV} \Rightarrow \lambda = 1117\,\text{nm}$) was used to filter out any of the remaining pump (the PMT is very sensitive to the pump wavelength).

A variable neutral density filter was used to vary the power of the incident fundamental radiation for the power dependence measurements. This filter was made of a fused silica glass substrate, with a reflective, metal (Inconel) coating, allowing for variable optical density from 0 to 4.

The Acton SP2150 monochromator served as a bandpass filter for the third harmonic signal. Light incident on a grating, whose groove separation is d, will have constructive interference maxima at $d\sin\theta_{max} = m\lambda$, where m is an integer. Thus, if there is a slit small enough to only pass light at a certain angle, then only certain wavelengths, specifically the third harmonic signal, will pass through the monochromator.

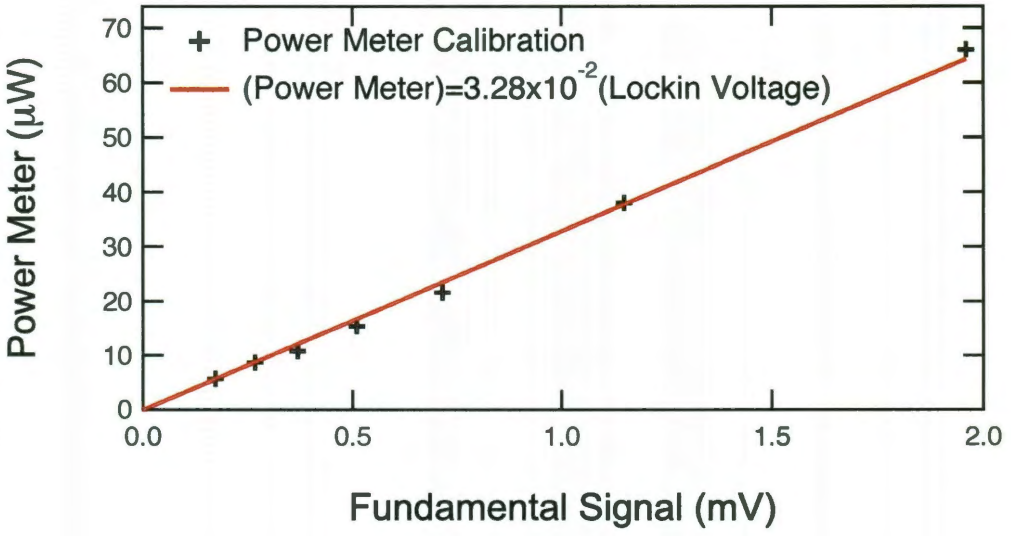

Figure 5.5 : Relation between the reference signal measured with the MCT detector and the power incident on the sample, measured with the power meter.

5.2.6 Calibration of the Fundamental

A small fraction of the fundamental was reflected using a CaF_2 window (97% transmission) to measure the relative intensity of the fundamental incident on the sample. This power was reduced further with neutral density filters so that we would not saturate our MCT detector. We calibrated the MCT by comparing the intensity (in volts on the lock-in amplifier) read by the MCT to the power at the sample, measured by a power meter. The calibration at 2100 nm is shown in Figure 5.5

5.2.7 Rotational Mount for Orientation Dependent Measurements

The sample was placed on a rotational mount for the THG experiment. Data was taken at normal incidence, as we rotate the sample through an angle, ϕ, starting from a position where the horizontally polarized fundamental is parallel to the SWCNT axis, as shown in Figure 5.6.

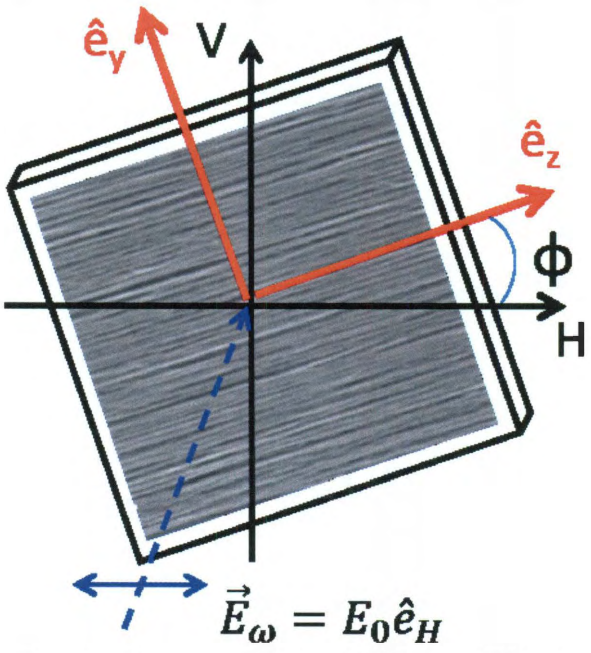

Figure 5.6 : Normal incidence view of a horizontally polarized fundamental incident on the sample, for third harmonic generation from highly aligned SWCNTs on sapphire.

Chapter 6

Experimental Results and Discussion I: Power Dependence of Third Harmonic Generation

Currently, there is a significant demand for thin-film nonlinear optical materials, which can be easily integrated into opto-electronic devices. Through theoretical and experimental findings, it has been pointed out that SWCNTs have a strong nonlinear third-order optical susceptibility, $\chi^{(3)}$, as reviewed in Chapter 5. Thus, it is of great interest to us accurately determine the nonlinear susceptibility $\chi^{(3)}$ of SWCNTs.

6.1 Derivation of the Third Harmonic Generation Efficiency

Here, we derive the third harmonic generation efficiency based on standard theory of nonlinear optics [11, 70, 71]. We start with Maxwell's equations (in CGS units) to describe the generation of the third harmonic frequency component as the fundamental travels through the material:

$$\vec{\nabla} \cdot \vec{D} = 4\pi\rho \tag{6.1}$$

$$\vec{\nabla} \cdot \vec{B} = 0 \tag{6.2}$$

$$\vec{\nabla} \times \vec{E} = -\frac{1}{c}\frac{\partial \vec{B}}{\partial t} \tag{6.3}$$

$$\vec{\nabla} \times \vec{H} = -\frac{1}{c}\frac{\partial \vec{D}}{\partial t} + \frac{4\pi}{c}\vec{J}. \tag{6.4}$$

Let us consider a region with no free charges ($\rho = 0$), and no free currents ($\vec{J} = 0$). Let us also consider that the material is nonmagnetic ($\vec{B} = \vec{H}$), so that Maxwell's equations reduce

to

$$\vec{\nabla}\cdot\vec{D}=0 \tag{6.5}$$

$$\vec{\nabla}\cdot\vec{B}=0 \tag{6.6}$$

$$\vec{\nabla}\times\vec{E}=-\frac{1}{c}\frac{\partial\vec{B}}{\partial t} \tag{6.7}$$

$$\vec{\nabla}\times\vec{B}=-\frac{1}{c}\frac{\partial\vec{D}}{\partial t} \tag{6.8}$$

If we take the curl of Equation (6.7), then we get

$$\vec{\nabla}\times\vec{\nabla}\times\vec{E}=-\frac{1}{c}\frac{\partial}{\partial t}\vec{\nabla}\times\vec{B}=-\frac{1}{c^2}\frac{\partial^2}{\partial t^2}\vec{D}. \tag{6.9}$$

Here, $\vec{D}$ is related to $\vec{E}$ as

$$\vec{D}=\vec{E}+4\pi\vec{P}, \tag{6.10}$$

and thus, Equation (6.9) becomes

$$\vec{\nabla}\times\vec{\nabla}\times\vec{E}+\frac{1}{c^2}\frac{\partial^2}{\partial t^2}\vec{E}=-\frac{4\pi}{c^2}\frac{\partial^2}{\partial t^2}\vec{P}. \tag{6.11}$$

Using the identity $\vec{\nabla}\times\vec{\nabla}\times\vec{E}=\vec{\nabla}(\vec{\nabla}\cdot\vec{E})-\vec{\nabla}^2\vec{E}$, we get the electromagnetic wave equation

$$\vec{\nabla}^2\vec{E}+\frac{1}{c^2}\frac{\partial^2}{\partial t^2}\vec{E}=-\frac{4\pi}{c^2}\frac{\partial^2}{\partial t^2}\vec{P}. \tag{6.12}$$

Note that the electromagnetic wave equation (6.12) is valid for both linear and nonlinear interactions.

If we recall from Section 3.1

$$\vec{P} = \chi^{(1)}\vec{E}+\chi^{(2)}\vec{E}^2+\chi^{(3)}\vec{E}^3+... \tag{6.13}$$

$$\equiv \vec{P}^{(1)}+\vec{P}^{(2)}+\vec{P}^{(3)}+..., \tag{6.14}$$

we can seperate our polarization into its linear and nonlinear parts. Thus, the wave equation becomes

$$\vec{\nabla}^2\vec{E}+\frac{1+4\pi\chi^{(1)}}{c^2}\frac{\partial^2}{\partial t^2}\vec{E}=-\frac{4\pi}{c^2}\frac{\partial^2}{\partial t^2}\vec{P}^{NL}, \tag{6.15}$$

where $\vec{P}^{NL} = \vec{P}^{(2)} + \vec{P}^{(3)} + ...$ If $\chi^{(3)}\vec{E}^3$ is the significant nonlinear source term, then the nonlinear wave equation becomes

$$\vec{\nabla}^2\vec{E} + \frac{n_\omega}{c^2}\frac{\partial^2}{\partial t^2}\vec{E} = -\frac{4\pi}{c^2}\frac{\partial^2}{\partial t^2}\chi^{(3)}\vec{E}^3, \tag{6.16}$$

where n_ω is the index of refraction of the fundamental. From this wave equation, we can predict the efficiency of the third harmonic generation process. We assume that the total field is a plane wave propagating in the z direction and has the form

$$E(z,t) = \frac{1}{2}\left[A_\omega(z)e^{-i(\omega t - k_\omega z)} + A_{3\omega}(z)e^{-i(3\omega t - k_{3\omega} z)} + \text{c.c.}\right] \tag{6.17}$$

where A_ω is the amplitude of the propagating fundamental field, and the propogation constants are given by $k_\omega = \omega n_\omega / c$ and $k_{2\omega} = 2\omega n_{2\omega}/c$, where n_ω and $n_{2\omega}$ are the refractive index for the fundamental and second harmonic, respectively. By substituting the total field into the wave equation and equating terms of the same frequency, we get the following coupled wave equations

$$2ik_\omega\frac{\partial A_\omega}{\partial z} = \frac{4\pi\omega^2}{c^2}\chi^3(\omega, 3\omega, -\omega, -\omega)A_{3\omega}A_\omega^{*2}e^{i\Delta kz} \tag{6.18}$$

$$2ik_{3\omega}\frac{\partial A_{3\omega}}{\partial z} = \frac{4\pi(3\omega)^2}{c^2}\chi^3(3\omega, \omega, \omega, \omega)A_\omega^3 e^{-i\Delta kz}, \tag{6.19}$$

where $\Delta k = k_{3\omega} - 3k_\omega$ is the phase mismatch between the third harmonic and the fundamental. Equations (6.19) and (6.19) can be rewritten as

$$\frac{dA_\omega}{dz} = \frac{3\pi i\omega}{n_\omega c}\chi^{(3)}A_{3\omega}A_\omega^{*2}e^{i\Delta kz} \tag{6.20}$$

$$\frac{dA_{3\omega}}{dz} = \frac{3\pi i\omega}{n_{3\omega}c}\chi^{(3)}A_\omega^3 e^{-i\Delta kz}. \tag{6.21}$$

If we consider the incident field to be constant during the interaction, then

$$\frac{dA_\omega}{dz} = 0. \tag{6.22}$$

The solution for $A_{3\omega}$ a medium that extends from $z = 0$ to $z = L$ is given by

$$A_{3\omega}(z) = \int_0^L \frac{3\pi i\omega}{n_{3\omega}c}\chi^{(3)}A_\omega^3 e^{-i\Delta kz} \tag{6.23}$$

i.e., the amplitude of the third harmonic field is given by

$$A_{3\omega}(z) = \frac{3\pi\omega}{n_{3\omega}c}A_\omega^3\chi^{(3)}\frac{1-e^{-i\Delta kL}}{\Delta k}. \tag{6.24}$$

The intensity of the third harmonic wave is given by the magnitude of the time-averaged Poynting vector, which is given by

$$I_{3\omega} = \frac{n_{3\omega}c}{8\pi}|A_{3\omega}|^2 \tag{6.25}$$

Thus, we obtain

$$I_{3\omega} = \frac{576\pi^4}{n_{3\omega}n_\omega^3\lambda_\omega^2 c^2}\left|\chi^{(3)}\right|^2 I_\omega^3 L^2\frac{\sin^2(\Delta kL/2)}{(\Delta kL/2)^2}, \tag{6.26}$$

where $I_\omega = \frac{n_\omega c}{8\pi}|A_\omega|^2$ is the intensity of the fundamental wave. From this equation we can see that the third harmonic intensity is a symmetric function about $\Delta k = 0$ with a maximum at $\Delta k = 0$, as shown in Figure 6.1. In the case where the fundamental and third harmonic are perfectly phase matched ($\Delta k = 0$) or quasi-phase matched ($\Delta kL/2 \ll \pi/2$), the third harmonic intensity increases quadratically with the length of the sample, L (Figure 6.2). However, in the case where the third harmonic and fundamental are phase mismatched, the third harmonic appears in the form of damped oscillations when traveling through the length of the sample. Equation (6.26) has been used to calculate the absolute value of $\chi^{(3)}$ for several materials via third harmonic generation.

6.2 Experimental Results

In order to ensure that the only produced harmonic is indeed coming from the SWCNT film, a substrate with relatively low $\chi^{(2)}$ and $\chi^{(3)}$ is needed [72]. Thus, measurements from

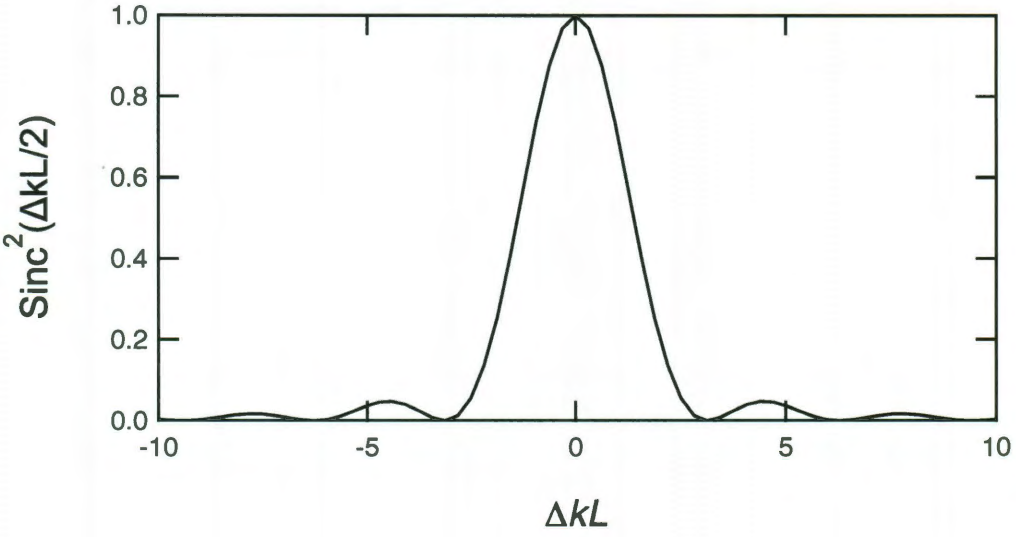

Figure 6.1 : The normalized third harmonic intensity as a function of wave vector mismatch. This intensity symmetric function around $\Delta k = 0$, $\text{sinc}^2(\Delta kL/2) = \frac{\sin^2(\Delta kL/2)}{(\Delta kL/2)^2}$, and has relative maximum and minimum values at areas when the third harmonic are completely in phase or completely out of phase, respectively.

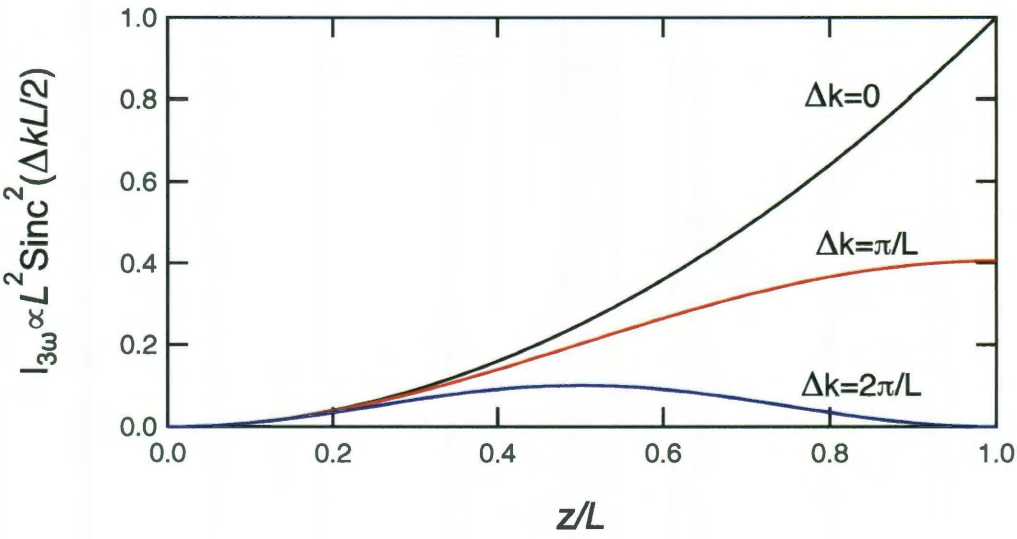

Figure 6.2 : The normalized third harmonic intensity as a function of distance for a medium of length L, for several values of phase mismatch, Δk. When completely phase matched, the third harmonic intensity proportional to the square of the distance traveled in the sample. At finite values of the phase mismatch, we can see that the third harmonic intensity oscillates as a function of interaction length.

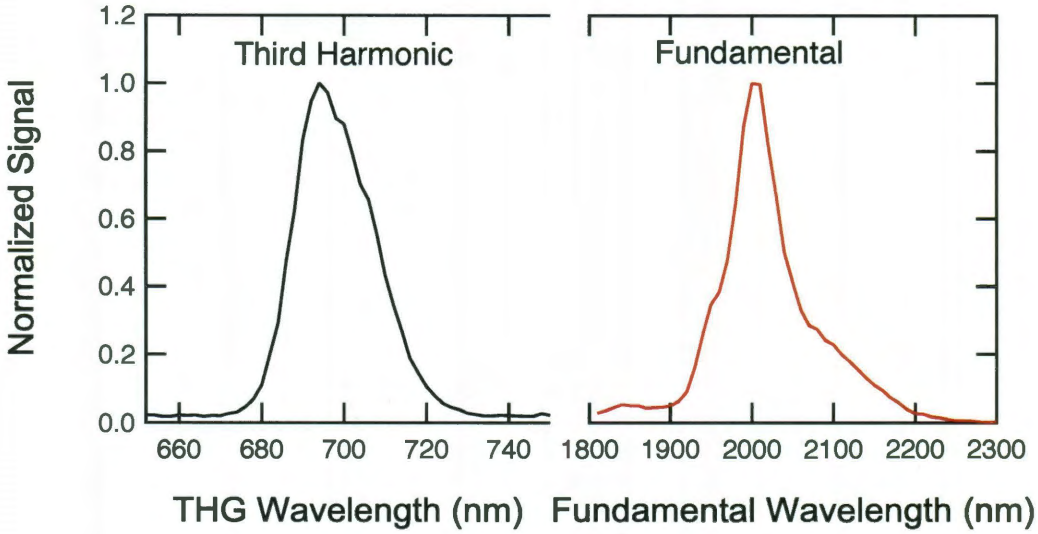

Figure 6.3 : (a) Generated third harmonic from highly aligned SWCNTs on sapphire and (b) its fundamental. The SWCNTs are aligned parallel to the incident fundamental and the induced THG is polarized parallel to the fundamental.

a sample of highly aligned SWCNTs on sapphire was used ($\chi^{(2)} = 0, \chi^{(3)} = 2.2$ esu [73]). Figure 6.3 shows a spectrally resolved third harmonic signal and its fundamental generated from our SWCNT sample. Changing the fundamental input wavelength caused a subsequent shift in the third harmonic signal, as shown in Figure 6.4, which confirms that we are indeed measuring a third harmonic signal. We also did not observe any third harmonic signal from the bulk sapphire substrate, and thus, the total measured signal can be attributed to the nanotube film. Figure 6.5 shows the power dependence for the SWCNT sample on a log/log plot. We can see that the third harmonic signal has a cubic power dependence with the fundamental. At lower powers, our signal was lost in the dark noise of the PMT as shown by the the deviation away from the fitting line.

In a separate experiment, we investigated the power dependence of the third harmonic signal in our SWCNT film at higher incident fields. To perform this experiment, we reduced

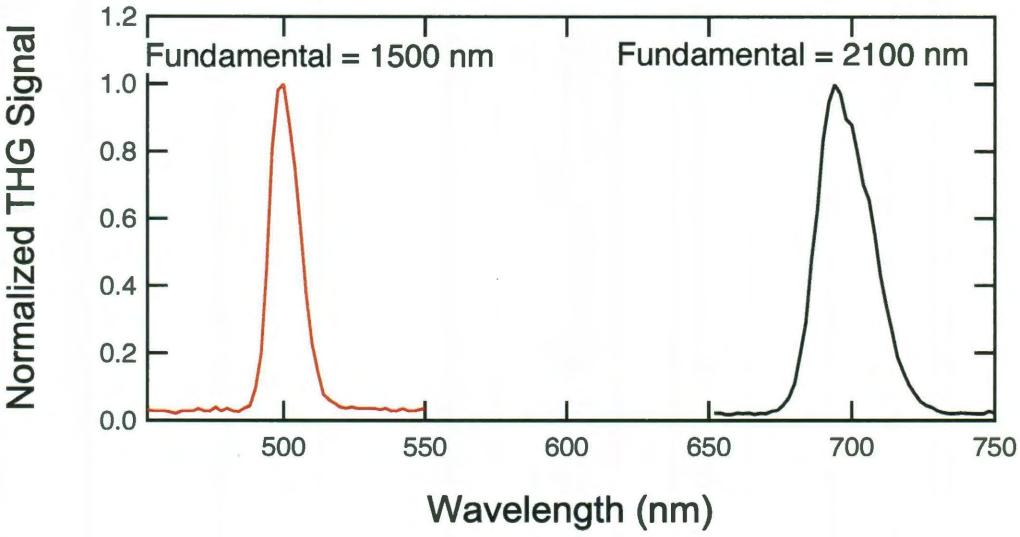

Figure 6.4 : Shift in third harmonic signal due to a shift in the fundamental from 2.1 to 1.5 μm. The SWCNTs are aligned parallel to the incident fundamental and the induced THG is polarized parallel to the fundamental.

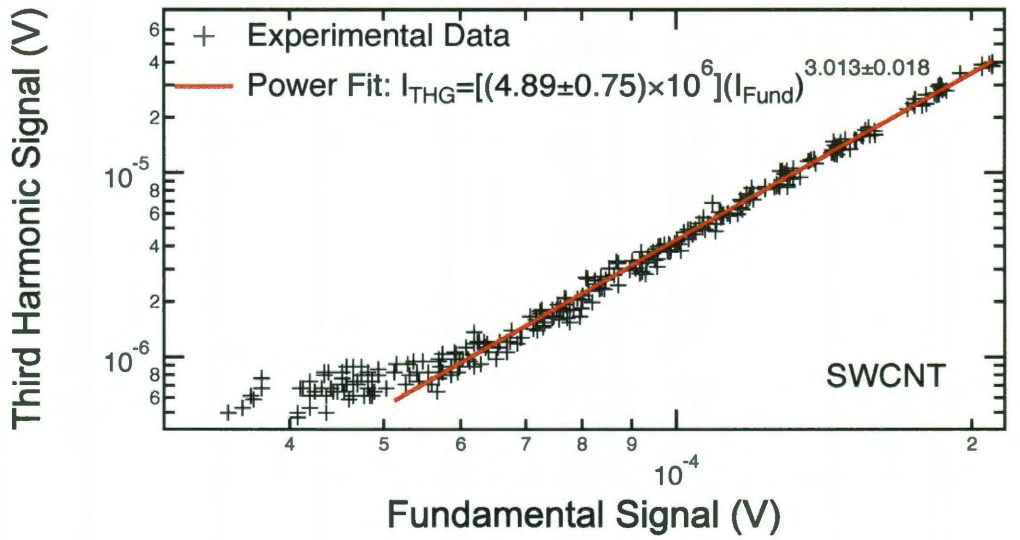

Figure 6.5 : Power dependence of the 700 nm third harmonic versus the 2100nm fundamental for the 2 μm thick highly-aligned SWCNTs sample. Third harmonic shows cubic power dependence with the incident fundamental, as shown by the slope of the log/log plot.

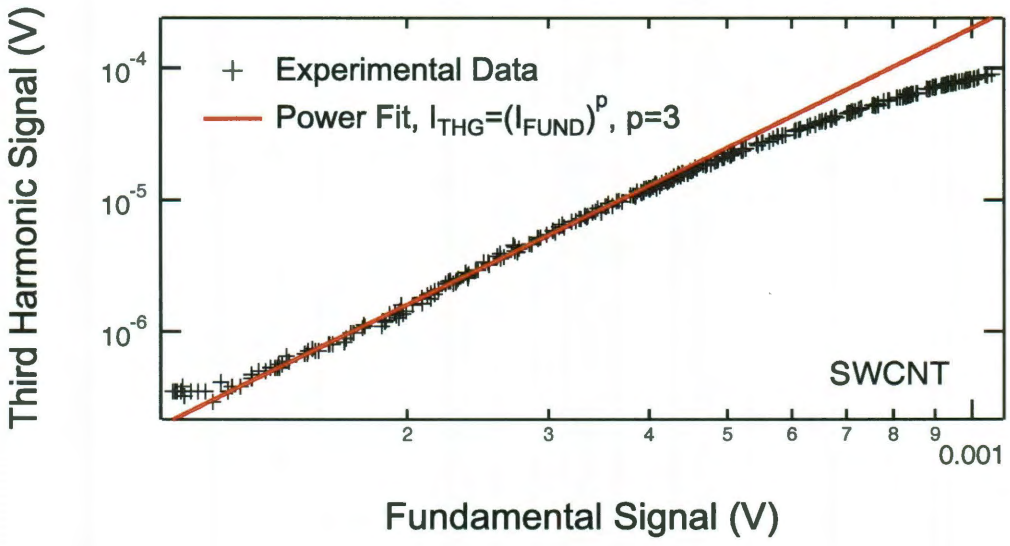

Figure 6.6 : Power dependence of the third harmonic versus the fundamental for the 2μm thick highly-aligned SWCNTs sample, at high incident fields. The third harmonic begins to saturate at a fundamental fluence of 1.8×10^{-4} J/cm^2.

voltage applied to the PMT detector, which the sensitivity, so that it would not be damaged. Figure 6.6 shows a saturation of the third harmonic signal at higher incident fields. If we use Figure 5.5 to calibrate our MCT with the power at the sample, we find that the third harmonic intensity begins to saturate at a fluence 1.8×10^{-4} J/cm^2 or peak intensity of 5.9×10^8 W/cm^2 (fundamental: repetition rate 1 kHz; focal spot size = $\pi(50\mu\text{m})^2$; saturation average power = 14μW; pulse width = 300 fsec).

To determine the absolute value of $\chi^{(3)}$ for carbon nanotubes, we compared the relative value of the third harmonic produced by the SWCNT sample to that of a fused silica film, whose $\chi^{(3)}$ value is known [74]. The power dependence for the third harmonic signal produced by the fused silica substrate is shown in Figure 6.7. Our data shows excellent power dependence, scaling with the cube of the fundamental.

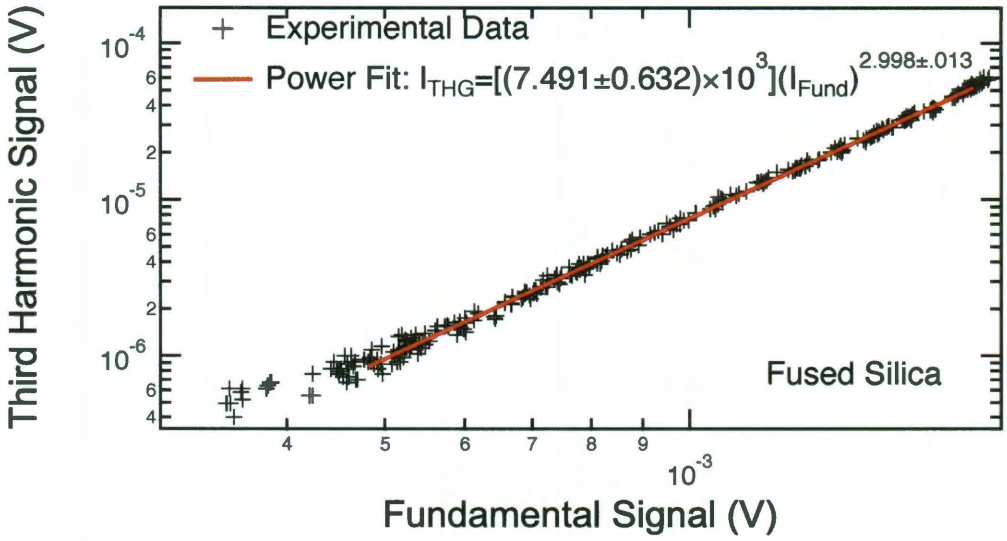

Figure 6.7 : Power dependence of the 700 nm third harmonic versus the 2100 nm fundamental for the 26.5 μm thick fused silica reference sample. Third harmonic shows cubic power dependence with the incident fundamental, as shown by the slope of the log/log plot.

6.3 Determination of the Third-Order Susceptibility

The absolute value of $\chi^{(3)}$ for the highly aligned carbon nanotube sample can be calculated by comparing our third harmonic intensity to the intensity of a reference material with known $\chi^{(3)}$. From Section 6.1, we learned that the third harmonic intensity is dependent on the thickness of the sample and the phase mismatch between the third harmonic and the pump fields. Before determining $\chi^{(3)}$ we made sure that the signal that we are measuring from the fused silica reference is within the coherent length. The coherence length of a material can be calculated by taking the inverse of the phase mismatch in reciprocal space via the equation

$$L_c = \frac{\pi}{\Delta k} = \frac{\pi}{|3k_\omega - k_\omega|} = \frac{\lambda}{3|n_\omega - n_{3\omega}|} \tag{6.27}$$

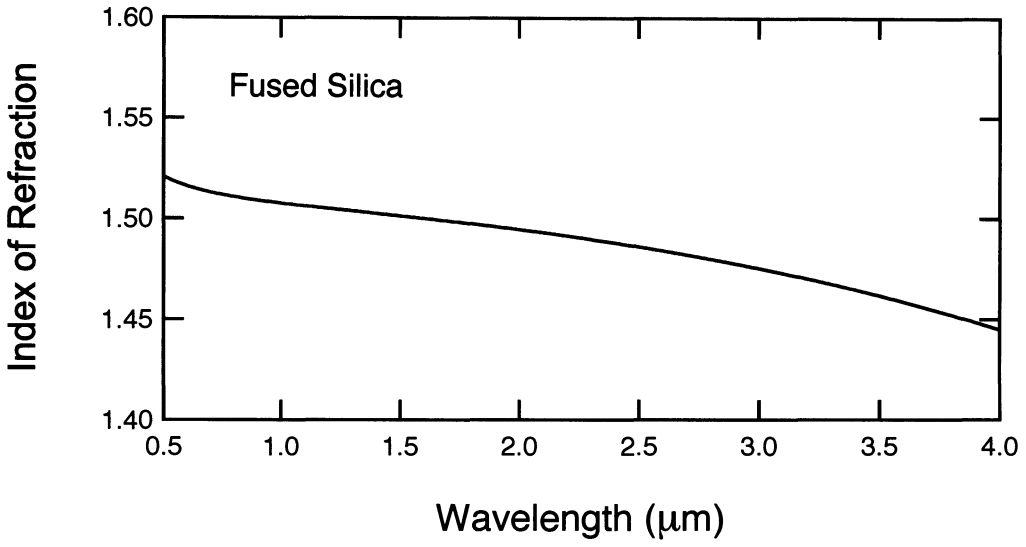

Figure 6.8 : Index of refraction for fused silica given by the Sellmeier equation Equation (6.28), with coefficients $B_1 = 0.69617$, $B_2 = 0.40794$, $B_3 = 0.89748$, $C_1 = 4.67914826 \times 10^{-3}\mu m^2$, $C_2 = 1.35121 \times 10^{-2}\mu m^2$, $C_3 = 97.934\mu m^2$ [25]. The Sellmeier equation deviates from the actual refractive index by less than 5×10^{-6} over the wavelengths range of 365 nm to 2.3 μm

The index of refraction for fused silica is given by the Sellmeier equation, which gives the index of refraction versus wavelength for a transparent material, given by

$$n^2(\lambda) = 1 + \frac{B_1\lambda^2}{\lambda^2 - C_1} + \frac{B_2\lambda^2}{\lambda^2 - C_2} + \frac{B_3\lambda^2}{\lambda^2 - C_3}. \tag{6.28}$$

$B_{1,2,3}$ and $C_{1,2,3}$ are experimentally determined Sellmeier coefficients, based on absorption resonances of B_i at a wavelength $\sqrt{C_i}$, where $B_1 = 0.69617$, $B_2 = 0.40794$, $B_3 = 0.89748$, $C_1 = 4.67914826 \times 10^{-3}\mu m^2$, $C_2 = 1.35121 \times 10^{-2}\mu m^2$, $C_3 = 97.934\mu m^2$ [25]. Plots for the index of refraction and subsequent coherence length for fused silica are shown in Figures 6.8 and 6.9, respectively. From the index of refraction, we can see that the third harmonic and the fundamental waves propagating through our sample will be phase mismatched, and that the optimal wavelength for which the fundamental and its third harmonic have the least phase mismatch occurs at $\lambda \approx 2100$ nm, and thus, this is the fundamental

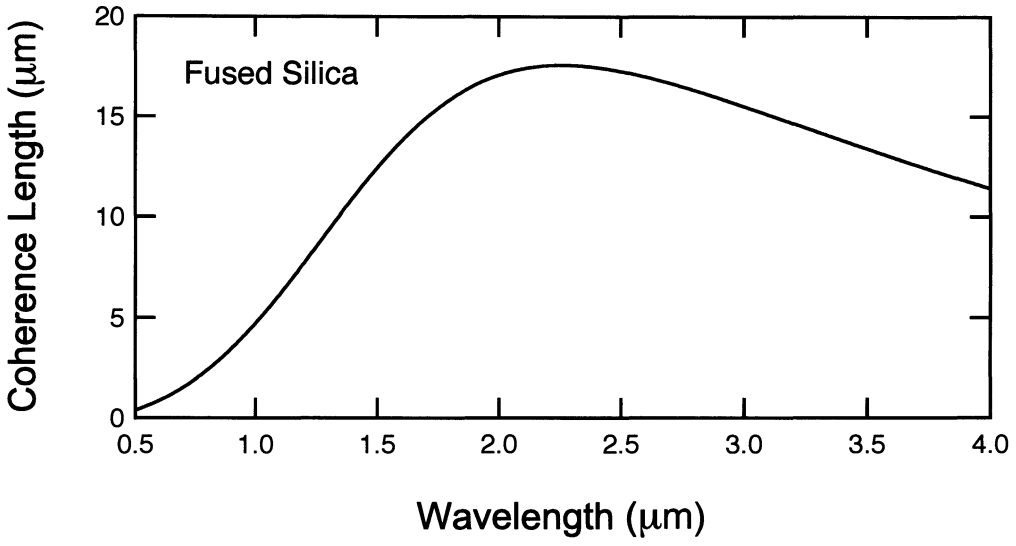

Figure 6.9 : Coherence length of fused silica for a given fundamental wavelength, based on the phase mismatch between the fundamental and its third harmonic. Coherence length is the length at which the third harmonic and fundamental are in phase.

wavelength that we chose for our experiment. The coherence length at 2100 nm is 17 μm. We should choose a reference thickness on the order of one coherence length.

Another important consideration is to make sure that the sample thickness is within the group velocity walk-off length of the fundamental and third harmonic. The group velocity walk-off length for the third harmonic and fundamental is given by

$$L_{WO} = (v_\omega - v_{3\omega})t = \frac{v_\omega + v_{3\omega}}{2}\tau \tag{6.29}$$

where τ is the width of the fundamental pulse and the group velocities v_ω and $v_{3\omega}$ are defined as

$$v_g = \frac{\partial \omega_i}{\partial k} = \frac{c}{n + \lambda_i \frac{\partial n}{\partial \lambda_i}}. \tag{6.30}$$

The walk-off length of the fundamental and the third harmonic is shown in Figure 6.10. The maximum group walk-off is approximately 40 μm.

Using Fourier transform infrared spectroscopy (FTIR) we measured the actual thickness

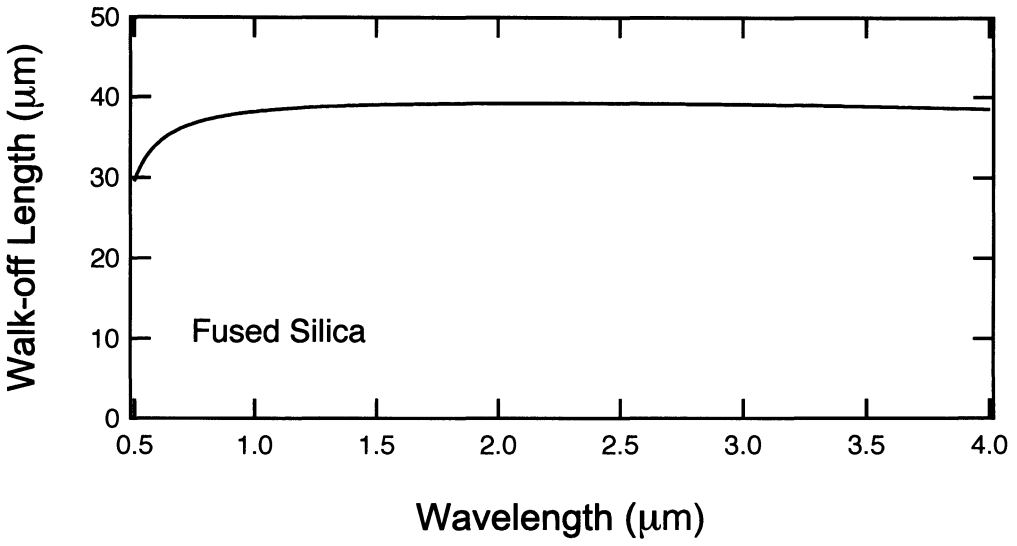

Figure 6.10 : Walk-off length versus the incident fundamental wavelength for fused silica. Walk-off length is the length at which the fundamental and its third harmonic are no longer interacting.

of the fused silica reference. The oscillations that occur in the fused silica reference are called Fabry-Perot fringes, caused by multiple reflections off of the faces of the fused silica substrate (Figure 6.11). The thickness of the fused silica sample is calculated from

$$d = \frac{v}{2\Delta\nu}, \tag{6.31}$$

where $\Delta\nu$ is the frequency of the oscillations (Hz), and v is the speed of light inside of the material. Thus, from Figure 6.11, the thickness of the fused silica reference is 26.5 μm (121 cm^{-1}, 7.25×10^{12} Hz), which is within the calculated walk-off length and on an order of the coherence length. Figure 6.12 shows the calculated normalized third harmonic signal in fused silica versus sample thickness from Equation (6.26). Fringes appear as a result of the phase mismatch between the fundamental and third harmonic. As you can see, there is a maximum in the third harmonic signal at $L_c = 17\mu$m. This difference between the third harmonic signal at the peak ($L_c = 17\mu$m) and the third harmonic signal at 25μm was taken

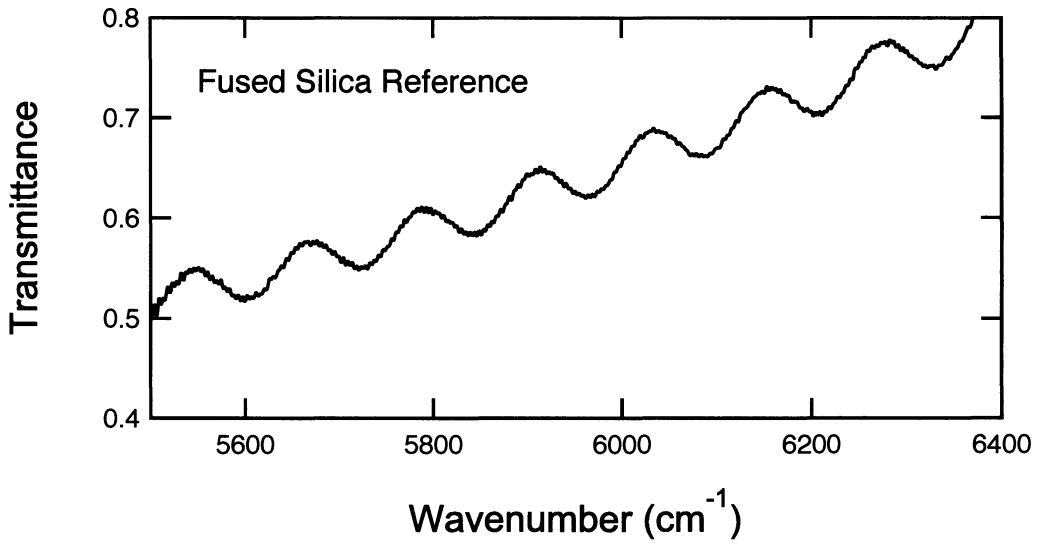

Figure 6.11 : Transmission of the near IR radiation through a thin fused silica film measured with the FTIR. Oscillations occur from constructive and destructive interference of the incident radiation caused by multiple reflections within the thin film.

into account, when calculating the absolute value of $\chi^{(3)}$ for the SWCNTs, as shown below.

The sample thickness was determined using vertical scanning interferometry, as shown in Figure 6.13. From this figure, we saw that the thickness of the SWCNT film varied from 1.7 μm in areas where two adjacent rows overlap to 1.5 μm in areas where there is no overlap. From this information, we used a thickness of 1.6 μm in our determination of $\chi^{(3)}$.

In order to calculate the third harmonic for both samples, we used Equation (6.26). Because the SWCNT film is made of mostly air, we assume the index of refraction to be 1 for both the fundamental and third harmonic frequencies, and thus, the phase mismatch for the third harmonic and fundamental was zero.

$$I_{3\omega,\mathrm{CNT}} = \frac{576\pi^5}{\lambda_\omega^2 c^2}\left|\chi^{(3)}_{\mathrm{CNT}}\right|^2 I^3_{\omega,\mathrm{CNT}} L^2_{\mathrm{CNT}} \tag{6.32}$$

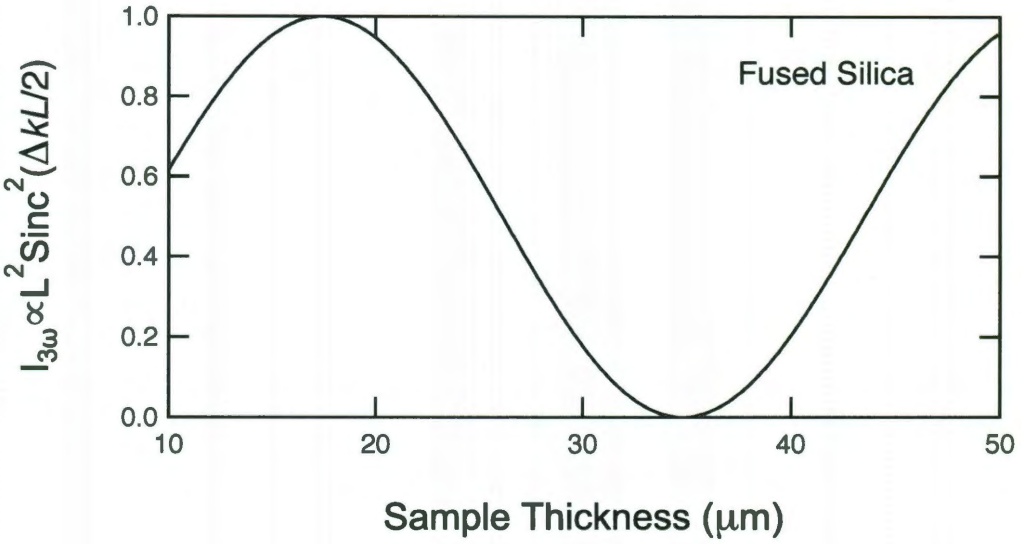

Figure 6.12 : Third harmonic intensity as a function of thickness of the fused silica reference. One full maker fringe is produced when the thickness of the fused silica reference is varied. When the thickness is equal to the coherence length, we observe a maxima.

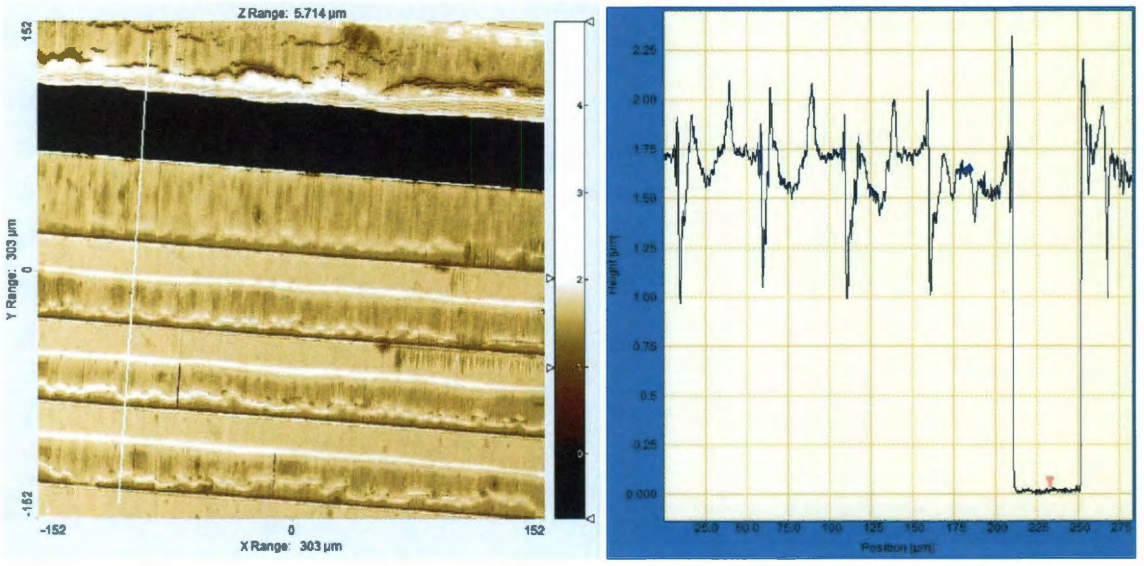

Figure 6.13 : The left figure is a vertical scanning interferometry image of the highly-aligned SWCNT sample thickness. The figure on the right shows the cross section taken along the white line in the figure on the left.

and for the fused silica reference, we find that

$$I_{3\omega,\mathrm{FS}} = \frac{576\pi^5}{n_{3\omega,\mathrm{FS}} n_{\omega,\mathrm{FS}}^3 \lambda_\omega^2 c^2} \left|\chi_{\mathrm{FS}}^{(3)}\right|^2 I_{\omega,\mathrm{FS}}^3 L_{\mathrm{FS}}^2 \frac{\sin^2(\Delta k L_{FS}/2)}{(\Delta k L_{\mathrm{FS}}/2)^2}. \tag{6.33}$$

Thus, if we take the ratio of the third order susceptibilities, we get

$$\frac{\chi_{\mathrm{CNT}}^{(3)}}{\chi_{\mathrm{FS}}^{(3)}} = \sqrt{n_{3\omega,\mathrm{FS}} n_{\omega,\mathrm{FS}}^3} \sqrt{\frac{I_{\omega,\mathrm{FS}}^3}{I_{\omega,\mathrm{CNT}}^3}} \sqrt{\frac{I_{3\omega,\mathrm{CNT}}}{I_{3\omega,\mathrm{FS}}}} \frac{L_{\mathrm{CNT}}}{L_{\mathrm{FS}} \mathrm{sinc}(\Delta k L_{\mathrm{FS}}/2)} \tag{6.34}$$

Finally, if we solve the equation for $\chi_{\mathrm{CNT}}^{(3)}$, we get

$$\chi_{CNT}^{(3)} = \sqrt{n_{3\omega,\mathrm{FS}} n_{\omega,\mathrm{FS}}^3} \sqrt{\frac{I_{\omega,\mathrm{FS}}^3}{I_{\omega,\mathrm{CNT}}^3}} \chi_{\mathrm{FS}}^{(3)} \sqrt{\frac{I_{3\omega,\mathrm{CNT}}}{I_{3\omega,\mathrm{FS}}}} \frac{L_{\mathrm{CNT}}}{L_{\mathrm{FS}} \mathrm{sinc}(\Delta k L_{\mathrm{FS}}/2)}. \tag{6.35}$$

Because each of the plots (Figure 6.5 and Figure 6.7) can be fit with a power function,

$$I_{3\omega} = A I_{3\omega}^3, \tag{6.36}$$

we compare the coefficients, A, to calculate the value of $\chi^{(3)}$ for the SWCNT film, using the relationship

$$\frac{A_{CNT}}{A_{FS}} = \frac{I_{3\omega,CNT}}{I_{3\omega,FS}} \frac{I_{3\omega,FS}^3}{I_{3\omega,CNT}^3}. \tag{6.37}$$

By inserting all of our known quantities into Equation (6.35) we find that the absolute value of $\chi^{(3)}$ for the film is 5.53×10^{-12} esu.

6.4 Discussion

The thicknesses of the sample and reference are very crucial to the magnitude of the third-order susceptibility. Thus far, we have assumed that the macroscopic thickness of the highly-aligned SWCNT sample to be approximately 1.6μm, but the actual thickness should be much smaller. The carbon density of our film was measured to be $60\,\mathrm{mg/cm^3}$ [26]. As you can see from the lack of sharp peaks in the absorption spectra of our samples, we

have a large diameter distribution. Our carbon nanotube diameters range from 2 to 6 nm in our film. Using the diameter distribution of carbon nanotubes in our film, shown in Figure 6.14b, we find that the average diameter of the tubes in our sample is 2.5 nm. By calculating the carbon density for the (19,19) carbon nanotube ($d_t = 3$ nm) in a densely packed hexagonal lattice (860 mg/cm^3), we found that the carbon density of our film corresponds to a 7 percent filling factor in a crystal with hexagonal packing. This is illustrated in Figure 6.15, where seven carbon nanotubes, shown in red, occupy a unit in a 100 space array. If we normalize the measured film thickness to that of a fully dense SWCNT film, we find that the effective thickness of our sample is 112 nm. This value is over one order of magnitude smaller than our previously used thickness. Thus, it is possible that the $\chi^{(3)}$ for the highly-aligned SWCNT film could be as much as an order of magnitude higher than the value we presented in the last section (5.53×10^{-12} esu). Given the effective thickness of the film, we find that the new absolute value of $\chi^{(3)}$ is 7.9×10^{-11} esu, which is extremely high for any material.

Another important question is whether the measured $\chi^{(3)}$ has any resonant enhancement due to interband transitions. From Figure 6.14b, we can see that there are a wide range of diameter tubes in our sample. Because, we excited our sample with 2100 nm light (4760 cm^{-1}), our fundamental wavelength were on resonance with the semiconductor E_{22} transition of a small collection of tubes within our sample. Thus, the measured third-order susceptibility of our sample was resonantly enhanced by those tubes. Even if we change the wavelength of our incident field, our sample would still be on resonance with a different collection of tubes within our sample. We need to consider a weighted average of the resonantly enhanced $\chi^{(3)}$ and the non-resonant $\chi^{(3)}$ from the carbon nanotubes in the film. However, we do not have enough information to draw quantitative conclusions on this point. If we were able to obtain a sample with a single chirality of highly aligned tubes,

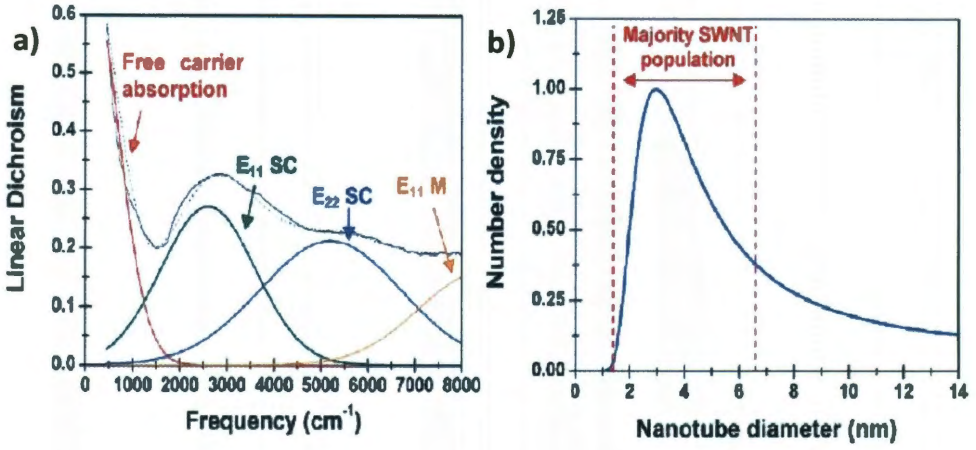

Figure 6.14 : (a) Linear absorption for the carbon nanotubes sample when it is polarized parallel to the incident fundamental. The relative contributions from the semiconductor optical transitions (E_{11} and E_{22}) and the free carrier absorption. (b) SWCNT diameter distribution extrapolated from fit in (a). [26]

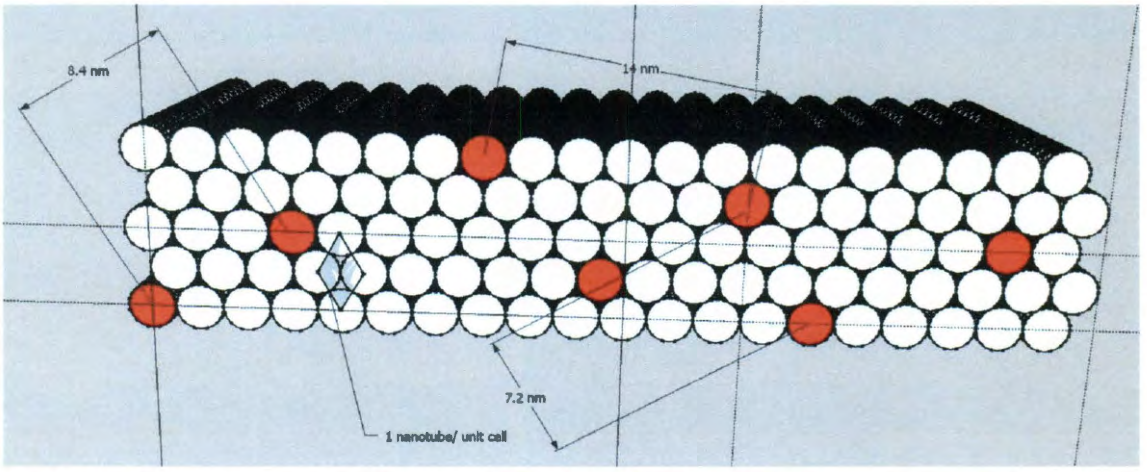

Figure 6.15 : Illustration of a hexagonal packed array, where carbon nanotubes have a 7% filling factor. By courtesy of Dr. Sèbastien Nanot.

then we could get a significant resonant enhancement of $\chi^{(3)}$ [14].

6.5 Conclusion

We found the power dependence of the third harmonic signal for the highly-aligned SWCNT film to scale with the cube of the fundamental, as expected for a third-order nonlinear optical process. This signal saturates at fluences greater than 1.8×10^{-4} J/cm^2. After comparing the ratio $I_{3\omega}/I_{\omega}^3$ of the SWCNT film to that of fused silica, whose $\chi^{(3)}$ is known, we were able to obtain a value of 5.53×10^{-12} esu for the absolute value of the third-order susceptibility for single-wall carbon nanotubes, which is similar to the $\chi^{(3)}$ values found from other methods. Considering that our sample is mostly air, with a filling factor of 7%, and all of the SWCNTs form bundles, the effective thickness of our sample can be as many as two orders of magnitude smaller than our nominal thickness, allowing us to obtain a $\chi^{(3)} = 7.9 \times 10^{-11}$ esu for our film. Because of the large diameter distribution in our sample, we believe that there are both resonant and non-resonant contributions to this value. With an appropriate sample of single chirality nanotubes, it is possible to increase this measured $\chi^{(3)}$ value by orders of magnitude.

Chapter 7

Experimental Results and Discussion II: Polarization Dependence of Third Harmonic Generation

In the previous chapter, we found that the highly aligned SWCNT film possesses a large $\chi^{(3)}$ value, leading to strong third harmonic generation. Furthermore, after rotating our sample by 90 degrees, we noticed that the third harmonic power went to zero, prompting us to investigate the reason for this anisotropy. Thus, orientation (ϕ) dependence was also systematically taken.

7.1 Experimental results

In this experiment, a third harmonic field is created by a linearly polarized fundamental electric field, which was normal incident onto the SWCNTs film. The direction of polarization was kept constant, while the sample was rotated through an angle ϕ, where $\phi = 0$ when the carbon nanotube axis is parallel to the incident fundamental, as shown in Figure 7.1. The generated third harmonic was detected in a transmission geometry. The measured third harmonic signal had both parallel and perpendicular polarization components relative to the incident fundamental polarization. Experimental results can be seen in Figures 7.2 and 7.3.

From these figures, there are some notable features to be discussed. There are anisotropies in the third harmonic signal for both polarizations. In the case where the measured third harmonic signal is polarized parallel to the incident fundamental (Figure 7.2), the intensity

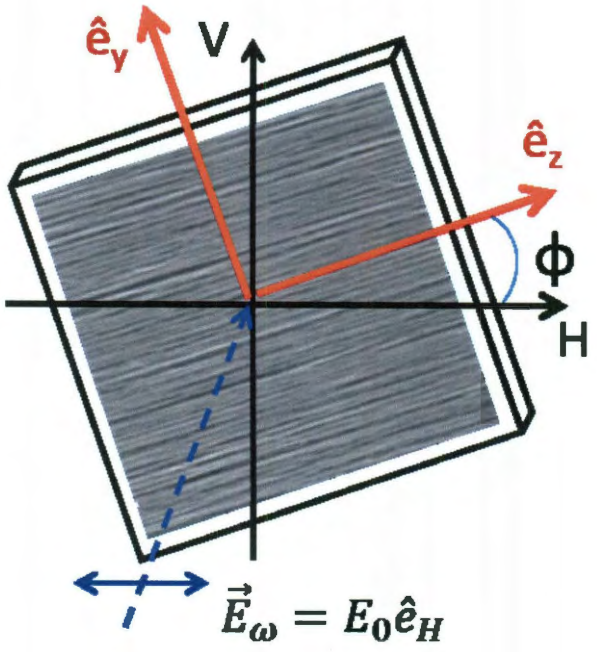

Figure 7.1 : Normal incidence view of a horizontally polarized fundamental incident on the sample, for third harmonic generation from highly aligned SWCNTs on sapphire.

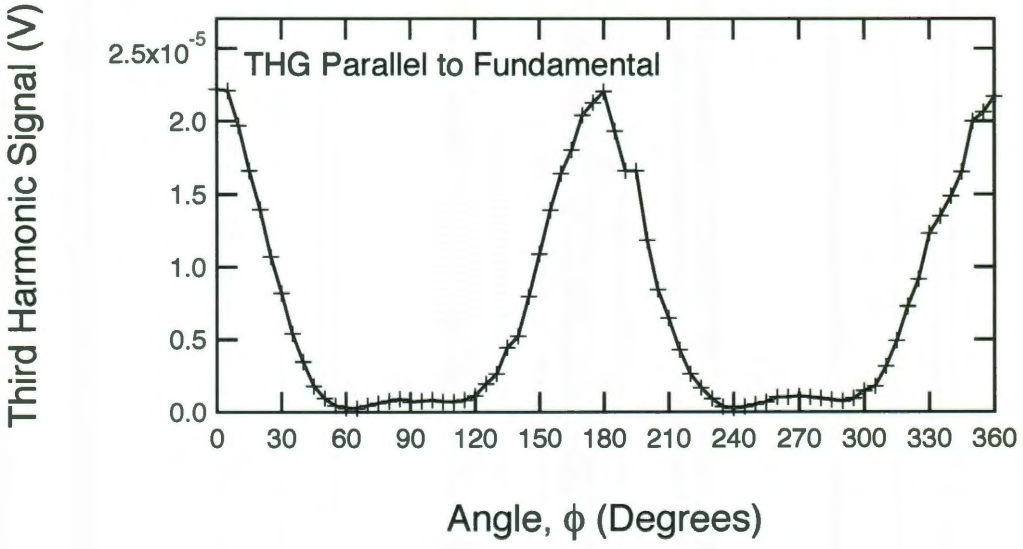

Figure 7.2 : ϕ dependence of the third harmonic signal, generated from the SWCNT film on sapphire. The third harmonic signal is polarized parallel to the fundamental. $\phi = 0$ corresponds to light polarization parallel to the nanotube axis.

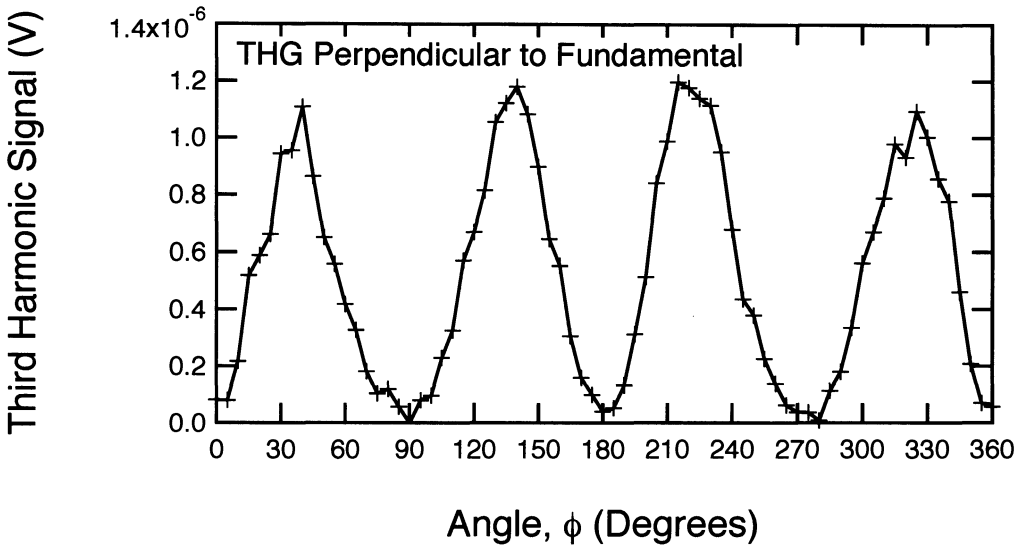

Figure 7.3 : ϕ dependence of the third harmonic signal, generated from the SWCNT film on sapphire. The third harmonic signal is polarized perpendicular to the fundamental. $\phi = 0$ corresponds to light polarization parallel to the nanotube axis.

measured when the fundamental is polarized parallel to the carbon nanotube axis is almost *two orders of magnitude larger* than that of the case where the fundamental is perpendicular to the nanotubes. This indicates that there is a strong interaction between the incident field and the nanotubes, when interacting with the axial direction of the tube. In the case where the measured third harmonic signal is polarized perpendicular to the incident fundamental, we see more oscillations than in the parallel case. Here, when the light is polarized parallel to the nanotube axis, the induced third harmonic signal is nearly zero. In both the parallel and perpendicular cases, the induced third harmonic is always zero, or nearly zero, when the incident fundamental is perpendicular to the axial direction of the nanotube. This data can give us significant insight into the relevant nonzero $\chi^{(3)}$ tensor elements for carbon nanotubes, as we discuss in the next section.

7.2 Determination of the Relevant Nonzero Tensor Components of $\chi^{(3)}$

In order to explain the anisotropic features found in our polarization dependent data, we must find out which components of the third-order susceptibility tensor contribute to the measured third harmonic signal. If we recall the intensity of the generated third harmonic field from the last chapter, and the definition of the third-order susceptibility presented in Chapter 3, the ith-component of the generated third harmonic field after traveling through a medium of length L is defined as

$$E_i(3\omega) = \frac{24\pi^2}{\sqrt{n_{3\omega}n_{\omega}^3}\lambda_{\omega}c} L \frac{\sin(\Delta kL/2)}{\Delta kL/2} \left[\sum_{j,k,l} \chi^{(3)}_{ijkl}(3\omega;\omega,\omega,\omega) E_j(\omega)E_k(\omega)E_l(\omega) \right] e^{i\Delta kL}. \tag{7.1}$$

where the quantity in the bracket is the polarization of the third harmonic, and $E_{j,k,l}(\omega)$ is the fundamental field in the j, k, and l directions. For simplicity we write

$$E_{3\omega,i} = A_{\mathrm{CNT}} \left[\sum_{j,k,l} \chi^{(3)}_{ijkl} E_{\omega,j}E_{\omega,k}E_{\omega,l} \right], \tag{7.2}$$

where A_{CNT} is a constant containing information about the fundamental-third harmonic interaction,

$$A_{\mathrm{CNT}} = \frac{24\pi^2}{\sqrt{n_{3\omega}n_{\omega}^3}\lambda_{\omega}c} L \frac{\sin(\Delta kL/2)}{\Delta kL/2} e^{i\Delta kL}. \tag{7.3}$$

In our experiment, the incident fundamental is initially polarized parallel to the axes (z axis) of the nanotubes within our highly aligned SWCNT film at $\phi = 0°$, as shown in Figure 7.1. When the sample is rotated, not all of the incident field is along the z axis of the SWCNTs. Thus, we have to project this fundamental onto the axial and radial directions of the carbon nanotubes. This can be done via the relation

$$\begin{pmatrix} \hat{e}_H \\ \hat{e}_V \end{pmatrix} = \begin{pmatrix} \cos\phi & -\sin\phi \\ \sin\phi & \cos\phi \end{pmatrix} \begin{pmatrix} \hat{e}_z \\ \hat{e}_y \end{pmatrix} \tag{7.4}$$

where $\hat{e}_H$ and $\hat{e}_V$ are unit vectors denoting the horizontal and vertical directions (relative to the optical table) of the incident field coordinate system, respectively. $\hat{e}_z$ and $\hat{e}_y$ are unit vectors denoting the axial and radial directions of the nanotube coordinate system. Thus, we can write the horizontally polarized fundamental $\vec{E} = E\hat{e_H}$ in terms of the nanotube coordinate system,

$$\vec{E} = E(\cos\phi\,\hat{e}_z - \cos\phi\,\hat{e}_y). \tag{7.5}$$

For a carbon nanotube, the non-zero components of the third-order nonlinear optical susceptibility $\chi^{(3)}$ are given by the relationship [75, 76]

$$\alpha\chi^{(3)}_{zzzz} = \chi^{(3)}_{zzyy} = \chi^{(3)}_{zyzy} = \chi^{(3)}_{zyyz} = \chi^{(3)}_{zzxx} = \chi^{(3)}_{zxzx} = \chi^{(3)}_{zxxz} \equiv \chi^{(3)}_{\mathrm{CNT}}, \tag{7.6}$$

where α ($0 < \alpha < 1$) represents the ratio of the contribution of the weaker tensor components to the dominant tensor component, $\chi^{(3)}_{zzzz}$. For the $\chi^{(3)}_{zzzz}$ component, the induced third harmonic along the axis of the tube is given by

$$E_{3\omega,z} = A_{\mathrm{CNT}}\chi^{(3)}_{zzzz}E_{\omega,z}E_{\omega,z}E_{\omega,z} \tag{7.7}$$

$$= A_{\mathrm{CNT}}\chi^{(3)}_{zzzz}E^3\cos^3\phi. \tag{7.8}$$

If we use the same formulation for the weaker tensor components, we find that the total third harmonic generated along the axis of the tube is

$$E_{3\omega,z} = A_{\mathrm{CNT}}\chi^{(3)}_{NT}E^3(\cos^3\phi + 3\alpha\cos\phi\sin^2\phi). \tag{7.9}$$

In order to find out the components of this induced third harmonic field polarized parallel and perpendicular to the fundamental, we must rotate the nanotube coordinate system back to the coordinate system of the incident fundamental using the relationship

$$\begin{pmatrix} \hat{e}_z \\ \hat{e}_y \end{pmatrix} = \begin{pmatrix} \cos\phi & \sin\phi \\ -\sin\phi & \cos\phi \end{pmatrix} \begin{pmatrix} \hat{e}_H \\ \hat{e}_V \end{pmatrix}. \tag{7.10}$$

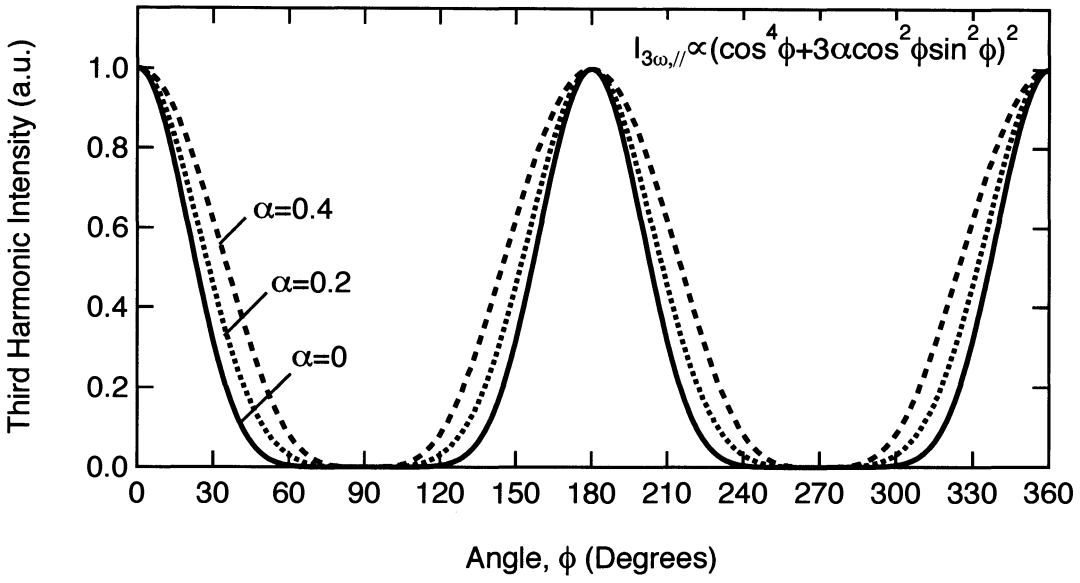

Figure 7.4 : Simulations for a THG signal polarized parallel to the fundamental, considering the $\chi^{(3)}$ tensor contribution relationship is $\alpha\chi^{(3)}_{zzzz} = \chi^{(3)}_{zzxx}$. This simulation shows ϕ dependence for variable α. $\phi = 0$ corresponds to light polarization parallel to the nanotube axis.

Thus, the total induced third harmonic field polarized parallel to the incident fundamental is

$$E_{3\omega,\|} = A_{\mathrm{CNT}}\chi^{(3)}_{NT}E^3(\cos^3\phi + 3\alpha\cos\phi\sin^2\phi)\cos\phi, \tag{7.11}$$

and the intensity is

$$I_{3\omega,\|} = |A_{\mathrm{CNT}}|^2|\chi^{(3)}_{NT}|^2I^3(\cos^4\phi + 3\alpha\cos^2\phi\sin^2\phi)^2. \tag{7.12}$$

Simulations for the third harmonic polarized parallel to the incident fundamental are shown in Figure 7.4, where $I_{3\omega,\|}$ is plotted as a function of ϕ for different values of α. From the figure we can see that the sharpness of the peak that would come purely from $\chi^{(3)}_{zzzz}$ gets broadened as the contribution from the weaker tensor components increases.

Similarly, the total induced third harmonic field polarized perpendicular to the incident

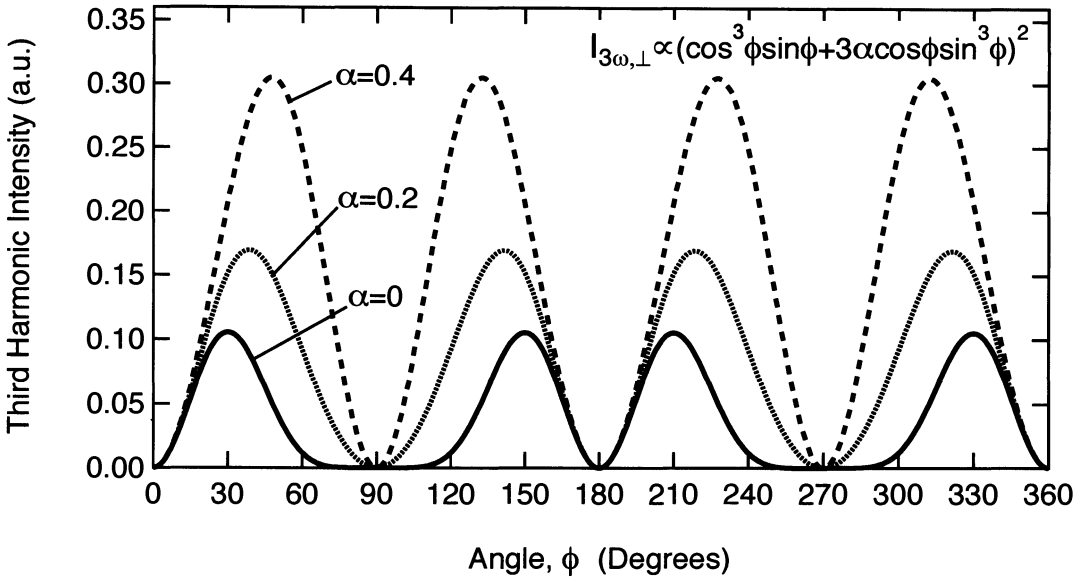

Figure 7.5 : Simulations for a THG signal polarized perpendicular to the fundamental, considering the $\chi^{(3)}$ tensor contribution relationship is $\alpha\chi^{(3)}_{zzzz} = \chi^{(3)}_{zzxx}$. This simulation shows ϕ dependence for variable α. $\phi = 0$ corresponds to light polarization parallel to the nanotube axis.

fundamental is

$$E_{3\omega,\perp} = A_{\mathrm{CNT}}\chi^{(3)}_{NT}E^3(\cos^3\phi + 3\alpha\cos\phi\sin^2\phi)\sin\phi \tag{7.13}$$

and the intensity is

$$I_{3\omega,\perp} = |A_{\mathrm{CNT}}|^2|\chi^{(3)}_{NT}|^2I^3(\cos^3\phi\sin\phi + 3\alpha\cos\phi\sin^3\phi)^2. \tag{7.14}$$

Simulations for the third harmonic polarized perpendicular to the incident fundamental are shown in Figure 7.5, where $I_{3\omega,\perp}$ is plotted as a function of ϕ for different values of α. In this figure, the peaks of the induced third harmonic shift and sharpen with larger contributions from the weaker tensor components.

We fit our data with the theoretically determined fit functions in Equations (7.12) and (7.14). By allowing the value of α to be the only adjustable parameter, we found that the measured THG spectra are in excellent agreement with the theoretically calculated THG,

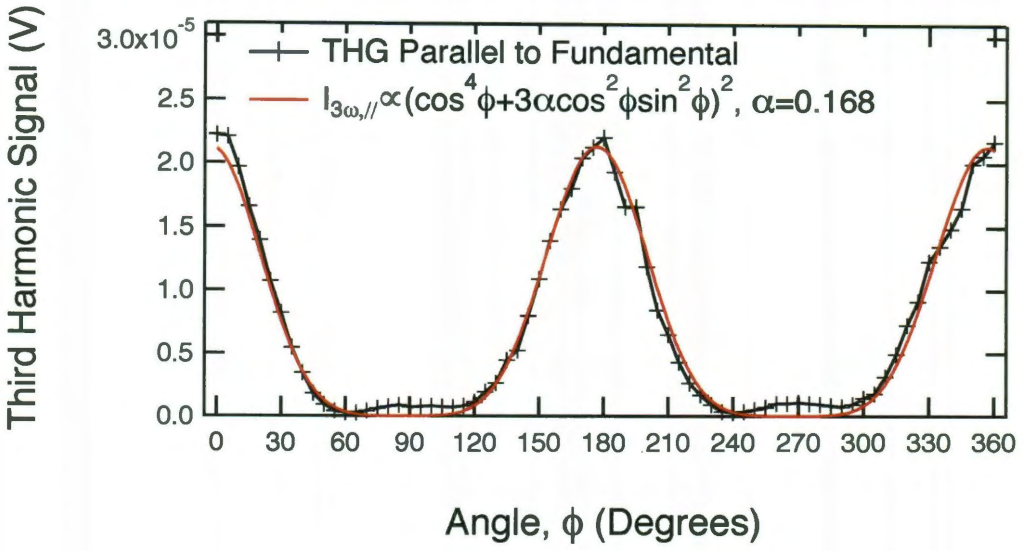

Figure 7.6 : Experimentally measured spectrum with theoretically calculated spectrum for a THG signal polarized parallel to the fundamental, considering the $\chi^{(3)}$ tensor contribution relationship is $\alpha\chi^{(3)}_{zzzz} = \chi^{(3)}_{zzxx}$. The following simulation shows ϕ dependence for variable α. $\phi = 0$ corresponds to light polarization parallel to the nanotube axis.

as shown in Figures 7.6 and 7.7. Not only do the fits correlate extremely well with the measurements, but the fit parameter α is approximately equal to 1/6 in both cases. This value indicates that the dominant $\chi^{(3)}$ tensor component, $\chi^{(3)}_{zzzz}$, is 6 times larger than the weaker components.

7.3 Conclusion

Polarization dependent measurements were performed on our highly aligned sample to extract the third-order SWCNT tensor elements that contribute to the large $\chi^{(3)}$ value measured in the last chapter. We measured the third harmonic signal polarized parallel and perpendicular to the incident fundamental, while rotating the sample through a full rotation. After calculating the ϕ dependence of the third harmonic signal, based on the nonzero

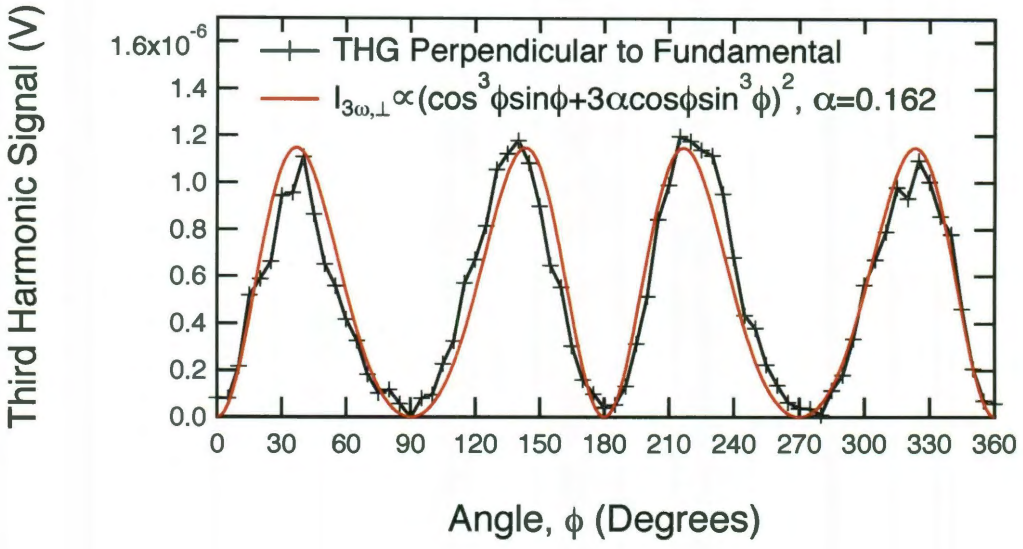

Figure 7.7 : Experimentally measured spectrum with theoretically calculated spectrum for a THG signal polarized perpendicular to the fundamental, considering the $\chi^{(3)}$ tensor contribution relationship is $\alpha\chi^{(3)}_{zzzz} = \chi^{(3)}_{zzxx}$. The following simulation shows ϕ dependence for variable α. $\phi = 0$ corresponds to light polarization parallel to the nanotube axis.

tensor components of the SWCNT third-order susceptibility tensor, it was shown that the third harmonic signal measured from the highly aligned SWCNT sample on sapphire had contributions from weaker $\chi^{(3)}$ tensor elements, and that these weaker components are approximately 1/6 the strength of the dominant $\chi^{(3)}_{zzzz}$.

Chapter 8

Summary

We successfully observed third harmonic generation in highly aligned SWCNTs on a sapphire substrate. Through power-dependent measurements, we found that the third harmonic signal scaled with the cube of the fundamental, which is expected for third harmonic generation (we also saw that the signal saturates at fluences greater than 1.8×10^{-4} J/cm^2). In order to calculate $\chi^{(3)}$ for the carbon nanotube film, we compared our third harmonic signal to that of a fused silica reference. After comparing the ratio $I_{3\omega}/I_{\omega}^3$ of the SWCNT film to that of fused silica, we were able to conclude that $\chi^{(3)} = 5.53 \times 10^{-12}$ esu for the carbon nanotube film, which is similar to previously reported $\chi^{(3)}$ values found from other methods. However, if we take into account the filling factor of 7% for our SWCNT sample, then the effective thickness of our sample is an order of magnitude smaller than our measured value. This allowed us to estimate a $\chi^{(3)}$ value of 7.9×10^{-11} esu for our film.

Furthermore, through orientation-dependent experiments we were successfully able to measure the polarization dependence of third harmonic generation in highly aligned SWCNTs. Thus, the relevant nonzero tensor elements for $\chi^{(3)}$ were extracted. We were also able to calculate the relative contribution of each tensor element to the nonlinear susceptibility. It was shown that the third harmonic signal measured from the highly aligned SWCNT sample had contributions from weaker $\chi^{(3)}$ tensor elements, and that these weaker components are approximately 1/6 the strength of the dominant $\chi^{(3)}_{zzzz}$.

Bibliography

[1] M. S. Dresselhaus, "Fifty years in studying carbon-based materials," *Physica Scripta*, vol. 2012, p. 014002, 2012.

[2] P. R. Wallace, "The band theory of graphite," *Phys. Rev.*, vol. 71, pp. 622–634, 1947.

[3] R. R. Nair, P. Blake, A. N. Grigorenko, K. S. Novoselov, T. J. Booth, T. Stauber, N. M. R. Peres, and A. K. Geim, "Fine structure constant defines visual transparency of graphene," *Science*, vol. 320, p. 1308, 2008.

[4] K. F. Mak, M. Y. Sfeir, Y. Wu, C. H. Lui, J. A. Misewich, and T. F. Heinz, "Measurement of the optical conductivity of graphene," *Phys. Rev. Lett.*, vol. 101, p. 196405, 2008.

[5] F. Schedin, A. K. Geim, S. V. Morozov, E. W. Hill, P. Blake, M. I. Katsnelson, and K. S. Novoselov, "Detection of individual gas molecules adsorbed on graphene," *Nat. Mat.*, vol. 6, pp. 652 – 655, 2007.

[6] K. S. Novoselov, A. K. Geim, S. V. Morozov, D. Jiang, Y. Zhang, S. Dubonos, I. V. Grigorieva, and A. A. Firsov, "Electric field effect in atomically thin carbon films," *Science*, vol. 306, pp. 666–669, 2004.

[7] M. D. Stoller, S. Park, Y. Zhu, J. An, and R. S. Ruoff, "Graphene-based ultracapacitors," *Nano Lett.*, vol. 8, pp. 3498–3502, 2008.

[8] F. Xia, T. Mueller, Y. Lin, A. Valdes-Garcia, and P. Avouris, "Ultrafast graphene photodetector," *Nat. Nanotechnol.*, vol. 4, pp. 839 – 843, 2009.

[9] H. W. C. Postma, T. Teepen, Z. Yao, M. Grifoni, and C. Dekker, "Carbon nanotube single-electron transistors at room temperature," *Science*, vol. 293, pp. 76–79, 2001.

[10] E. S. Snow, F. K. Perkins, E. J. Houser, S. C. Badescu, and T. L. Reinecke, "Chemical detection with a single-walled carbon nanotube capacitor," *Science*, vol. 307, pp. 1942–1945, 2005.

[11] A. K. Geim and K. S. Novoselov, "The rise of graphene," *Nature Mater.*, vol. 6, pp. 183 –191, 2007.

[12] T. H. Maiman, "Stimulated Optical Radiation in Ruby," *Nature*, vol. 187, pp. 493–494, 1960.

[13] P. A. Franken, A. E. Hill, C. W. Peters, and G. Weinreich, "Generation of optical harmonics," *Phys. Rev. Lett.*, vol. 7, pp. 118–119, 1961.

[14] Y. Shen, *The principles of nonlinear optics*. Wiley classics library, Hoboken: Wiley-Interscience, 2003.

[15] C. Kittel, *Introduction to Solid State Physics*. New York: John Wiley & Sons, Inc., 6th ed., 1986.

[16] M. Dresselhaus, G. Dresselhaus, R. Saito, and A. Jorio, "Raman spectroscopy of carbon nanotubes," *Phys. Rep.*, vol. 409, pp. 47 – 99, 2005.

[17] P. Avouris, Z. Chen, and V. Perebeinos, "Carbon-based electronics," *Nat. Nanotechnol.*, vol. 2, pp. 605 – 615, 2007.

[18] T. W. Odom, J. L. Huang, P. Kim, and C. M. Lieber, "Structure and electronic properties of carbon nanotubes," *J. Phys. Chem. B*, vol. 104, pp. 2794–2809, 2000.

[19] K. V. Christ and H. R. Sadeghpour, "Energy dispersion in graphene and carbon nanotubes and molecular encapsulation in nanotubes," *Phys. Rev. B*, vol. 75, p. 195418, 2007.

[20] R. W. Boyd, *Nonlinear Optics: 2nd Edition.* San Diego: Academic Press, 2003.

[21] N. W. Ashcroft and D. N. Mermin, *Solid State Physics.* Toronto: Thomson Learning, 1976.

[22] A. Hagen and T. Hertel, "Quantitative analysis of optical spectra from individual single-wall carbon nanotubes," *Nano Lett.*, vol. 3, pp. 383–388, 2003.

[23] R. B. Weisman and S. M. Bachilo, "Dependence of optical transition energies on structure for single-walled carbon nanotubes in aqueous suspension: An empirical kataura plot," *Nano Lett.*, vol. 3, pp. 1235–1238, 2003.

[24] T. Ando, "Theory of electronic states and optical absorption in carbon nanotubes," *Proceedings of Optoelectronics: Physics and Simulation of Optoelectronic Devices XII*, 2004.

[25] H. Ajiki and T. Ando, "Aharonov-bohm effect in carbon nanotubes," *Physica B*, vol. 201, pp. 349 – 352, 1994.

[26] M. J. O. Connell, S. M. Bachilo, C. B. Huffman, V. C. Moore, E. H. Haroz, K. L. Rialon, P. J. Boul, W. H. Noon, C. Kittrell, J. Ma, R. H. Hauge, R. B. Weisman, and R. E. Smalley, "Band-gap flourescence from individual single-walled carbon nanotubes," *Science*, vol. 297, pp. 593–596, 2002.

[27] J. Lefebvre, S. Maruyama, and P. Finnie, "Photoluminescence: Science and applications," in *Carbon Nanotubes*, vol. 111 of *Topics in Applied Physics*, pp. 287–319, Springer Berlin / Heidelberg, 2008.

[28] S. M. Bachilo, M. Sergei, M. S. Strano, C. Kittrell, R. H. Hauge, R. E. Smalley, and R. B. Weisman, "Structure-assigned optical spectra of single-walled carbon nanotubes," *Science*, vol. 298, pp. 2361–2366, 2002.

[29] C. Fantini, A. Jorio, M. Souza, M. S. Strano, M. S. Dresselhaus, and M. A. Pimenta, "Optical transition energies for carbon nanotubes from resonant raman spectroscopy: Environment and temperature effects," *Phys. Rev. Lett.*, vol. 93, p. 147406, 2004.

[30] A. G. Souza Filho, S. G. Chou, G. G. Samsonidze, G. Dresselhaus, M. S. Dresselhaus, L. An, J. Liu, A. K. Swan, M. S. Ünlü, B. B. Goldberg, A. Jorio, A. Grüneis, and R. Saito, "Stokes and anti-stokes raman spectra of small-diameter isolated carbon nanotubes," *Phys. Rev. B*, vol. 69, p. 115428, 2004.

[31] P. Eklund, J. Holden, and R. Jishi, "Vibrational modes of carbon nanotubes; spectroscopy and theory," *Carbon*, vol. 33, pp. 959 – 972, 1995.

[32] A. Jorio and M. S. Dresselhaus, eds., *Carbon Nanotubes: Advanced Topics in the Synthesis, Structure, Properties and Applications*. Berlin: Springer, 2008.

[33] F. Jonsson, "The nonlinear susceptibilities and their symmetries." Visited Nov 2011. http://jonsson.eu/research/lectures.

[34] G. Y. Guo, K. C. Chu, D.-S. Wang, and C.-G. Duan, "Linear and nonlinear optical properties of carbon nanotubes from first-principles calculations," *Phys. Rev. B*, vol. 69, p. 205416, 2004.

[35] L. D. Dominicis, S. Botti, L. S. Asilyan, R. Ciardi, R. Fantoni, M. L. Terranova, A. Fiori, S. Orlanducci, and R. Appolloni, "Second- and third- harmonic generation in single-walled carbon nanotubes at nanosecond time scale," *Appl. Phys. Lett.*, vol. 85, pp. 1418–1420, 2004.

[36] H. M. Su, J. T. Ye, Z. K. Tang, and K. S. Wong, "Resonant second-harmonic generation in monosized and aligned single-walled carbon nanotubes," *Phys. Rev. B*, vol. 77, p. 125428, 2008.

[37] V. Margulis and T. Sizikova, "Theoretical study of third-order nonlinear optical response of semiconductor carbon nanotubes," *Physica B*, vol. 245, pp. 173 – 189, 1998.

[38] V. A. Margulis, E. A. Gaiduk, and E. N. Zhidkin, "Quadratic electro-optic effects in semiconductor carbon nanotubes," *Phys. Lett. A*, vol. 258, pp. 394 – 400, 1999.

[39] V. A. Margulis and E. A. Gaiduk, "Theoretical modelling of nonlinear refraction and two-photon absorption in single-wall carbon nanotube bundles," *J. Opt. A: Pure Appl. Opt.*, vol. 3, p. 267, 2001.

[40] R. Xie and J. Jiang, "Nonlinear optical properties of armchair nanotube," *Appl. Phys. Lett.*, vol. 71, pp. 1029–1031, 1997.

[41] V. Margulis, E. Gaiduk, and E. Zhidkin, "Third-order optical nonlinearity of semiconductor carbon nanotubes: third harmonic generation," *Diamond Rel. Mat.*, vol. 8, pp. 1240 – 1245, 1999.

[42] J. Jiang, J. Dong, and D. Y. Xing, "Size and helical symmetry effects on the nonlinear optical properties of chiral carbon nanotubes," *Phys. Rev. B*, vol. 59, pp. 9838–9841, 1999.

[43] H. Ajiki and T. Ando, "Electronic states of carbon nanotubes," *J. Phys. Soc. Jpn.*, vol. 62, pp. 1255–1266, 1993.

[44] V. N. Genkin and P. M. Mendis, "Contribution to theory of nonlinear effects in crystals with account taken of partially filled bands," *Sov. Phys. JETP*, vol. 27, pp. 609–, 1968.

[45] L. Vivien, E. Anglaret, D. Riehl, F. Hache, F. Bacou, M. Andrieux, F. Lafonta, C. Journet, C. Goze, M. Brunet, and P. Bernier, "Optical limiting properties of singlewall carbon nanotubes," *Opt. Comm.*, vol. 174, pp. 271 – 275, 2000.

[46] O. Muller, Y. Lutz, A. Teissier, J. P. Moeglin, and V. Keller, "Optical limiting behavior of carbon nanotubes exposed to infrared laser irradiations studied by the z-scan technique," *Appl. Opt.*, vol. 49, pp. 1097–1103, 2010.

[47] J. Seo, S. Ma, Q. Yang, L. Creekmore, R. Battle, M. Tabibi, H. Brown, A. Jackson, T. Skyles, B. Tabibi, S. Jung, and M. Namkung, "Third-order optical nonlinearities of singlewall carbon nanotubes for nonlinear transmission limiting application," *J. Phys.: Conf. Ser.*, vol. 38, p. 37, 2006.

[48] S. Tatsuura, M. Furuki, Y. Sato, I. Iwasa, M. Tian, and H. Mitsu, "Semiconductor carbon nanotubes as ultrafast switching materials for optical telecommunications," *Adv. Mat.*, vol. 15, pp. 534–537, 2003.

[49] J. Wang, Y. Chen, and W. J. Blau, "Carbon nanotubes and nanotube composites for nonlinear optical devices," *J. Mater. Chem.*, vol. 19, pp. 7425–7443, 2009.

[50] H. I. Elim, W. Ji, G. H. Ma, K. Y. Lim, C. H. Sow, and C. H. A. Huan, "Ultrafast absorptive and refractive nonlinearities in multiwalled carbon nanotube films," *Appl. Phys. Lett.*, vol. 85, p. 1799, 2004.

[51] A. G. Rozhin, Y. Sakakibara, M. Tokumoto, H. Kataura, and Y. Achiba, "Near-infrared nonlinear optical properties of single-wall carbon nanotubes embedded in polymer film," *Thin Solid Films*, vol. 464, pp. 368 – 372, 2004.

[52] D. Shimamoto, T. Sakurai, M. Itoh, Y. A. Kim, T. Hayashi, M. Endo, and M. Terrones, "Nonlinear optical absorption and reflection of single wall carbon nanotube thin films by z-scan technique," *Appl. Phys. Lett.*, vol. 92, p. 081902, 2008.

[53] D. V. Khudyakov, A. S. Lobach, and V. A. Nadtochenko, "Nonlinear optical absorption of single-wall carbon nanotubes in carboxymethylcellulose thin polymerfilm and its application as a saturable absorber for mode-locking in pulsed nd:glass laser," *Appl. Opt.*, vol. 48, pp. 1624–1627, 2009.

[54] H. I. Elim, W. Ji, G. H. Ma, K. Y. Lim, C. H. Sow, and C. H. A. Huan, "Ultrafast absorptive and refractive nonlinearities in multiwalled carbon nanotube films," *Appl. Phys. Lett.*, vol. 85, pp. 1799–1801, 2004.

[55] X. Liu, J. Si, B. Chang, G. Xu, Q. Yang, Z. Pan, S. Xie, P. Ye, J. Fan, and M. Wan, "Third-order optical nonlinearity of the carbon nanotubes," *Appl. Phys. Lett.*, vol. 74, pp. 164 – 166, 1999.

[56] G. Y. Slepyan, S. A. Maksimenko, V. P. Kalosha, J. Herrmann, E. E. B. Campbell, and I. V. Hertel, "Highly efficient high-order harmonic generation by metallic carbon nanotubes," *Phys. Rev. A*, vol. 60, pp. R777–R780, 1999.

[57] Z. Jin, X. Sun, G. Xu, S. H. Goh, and W. Ji, "Nonlinear optical properties of some polymer/multi-walled carbon nanotube composites," *Chem. Phys. Lett.*, vol. 318, pp. 505 – 510, 2000.

[58] S. Wang, W. Huang, H. Yang, Q. Gong, Z. Shi, X. Zhou, D. Qiang, and Z. Gu, "Large and ultrafast third-order optical non-linearity of single-wall carbon nanotubes at 820 nm," *Chem. Phys. Lett.*, vol. 320, pp. 411 – 414, 2000.

[59] P. Myllyperkio, O. Herranen, J. Rintala, H. Jiang, P. R. Mudimela, Z. Zhu, A. G. Nasibulin, A. Johansson, E. I. Kauppinen, M. Ahlskog, and M. Pettersson, "Femtosecond four-wave-mixing spectroscopy of suspended individual semiconducting single-walled carbon nanotubes," *ACS Nano*, vol. 4, pp. 6780–6786, 2010.

[60] H. Kim, T. Sheps, P. G. Collins, and E. O. Potma, "Nonlinear optical imaging of individual carbon nanotubes with four-wave-mixing microscopy," *Nano Lett.*, vol. 9, pp. 2991–2995, 2009.

[61] J. R. Heflin, K. Y. Wong, O. Zamani-Khamiri, and A. F. Garito, "Nonlinear optical properties of linear chains and electron-correlation effects," *Phys. Rev. B*, vol. 38, pp. 1573–1576, 1988.

[62] C. Stanciu, R. Ehlich, V. Petrov, O. Steinkellner, J. Herrmann, I. V. Hertel, G. Y. Slepyan, A. A. Khrutchinski, S. A. Maksimenko, F. Rotermund, E. E. B. Campbell, and F. Rohmund, "Experimental and theoretical study of third-order harmonic generation in carbon nanotubes," *Appl. Phys. Lett.*, vol. 81, pp. 4064–4066, 2002.

[63] M. Sheik-Bahae, A. Said, T. H. Wei, D. J. Hagan, and E. W. V. Stryland, "Sensitive measurement of optical nonlinearities using a single beam," *IEEE J. Quant. Electron.*, vol. 26, pp. 760 –769, 1990.

[64] C. L. Pint, Y. Xu, M. Pasquali, and R. H. Hauge, "Formation of highly dense aligned ribbons and transparent films of single-walled carbon nanotubes directly from carpets," *ACS Nano*, vol. 2, pp. 1871–1878, 2008.

[65] L. Ren, C. Pint, L. G. Booshehri, W. D. Rice, X. Wang, D. J. Hilton, K. Takeya, I. Kawayama, M. Tonouchi, R. H. Hauge, and J. Kono, "Carbon nanotube terahertz polarizer," *Nano Lett.*, vol. 9, pp. 2610–2613, 2009.

[66] L. Ren, C. L. Pint, T. Arikawa, K. Takeya, I. Kawayama, M. Tonouchi, R. H. Hauge, and J. Kono, "Broadband terahertz polarizers with ideal performance based on aligned carbon nanotube stacks," *Nano Lett.*, vol. 12, pp. 787–790, 2012.

[67] Center for Ultrafast Optical Science, "Chirped pulse amplification." Visited April 2012. http://www.engin.umich.edu/research/cuos/ResearchGroups/HFS/Experimentalfacilities/Chirped_Pulse_Amp.html.

[68] J. F. Reintjes, *Nonlinear optical parametric processes in liquids and gases*. Quantum electronics–principles and applications, New York: Academic Press, 1984.

[69] G. L. Woods, *Nonlinear Optical Frequency Conversion Devices Based on Intersubband Transitions in Semiconductor Quantum Wells*. PhD thesis, Stanford University, 1997.

[70] M. Levenson, "Feasibility of measuring the nonlinear index of refraction by third-order frequency mixing," *IEEE J. Quant. Electron.*, vol. 10, pp. 110 – 115, 1974.

[71] R. W. Boyd and G. L. Fischer, "Nonlinear optical materials," in *Encyclopedia of Materials: Science and Technology* (K. J. Buschow, R. W. Cahn, M. C. Flemings, B. Ilschner, E. J. Kramer, and S. Mahajan, eds.), pp. 6237–6244, Elsevier, 2001.

[72] B. Buchalter and G. R. Meredith, "Third-order optical susceptibility of glasses determined by third harmonic generation," *Appl. Opt.*, vol. 21, pp. 3221–3224, 1982.

[73] E. Palik, *Handbook of Optical Constants of Solids II.* Handbook of Optical Constants of Solids, San Diego: Academic Press, 1991.

[74] C. L. Pint, Y.-Q. Xu, E. Morosan, and R. H. Hauge, "Alignment dependence of one-dimensional electronic hopping transport observed in films of highly aligned, ultra-long single-walled carbon nanotubes," *Appl. Phys. Lett.*, vol. 94, p. 182107, 2009.

[75] L. Jensen, P.-O. strand, and K. V. Mikkelsen, "Saturation of the third-order polarizability of carbon nanotubes characterized by a dipole interaction model," *Nano Lett.*, vol. 3, pp. 661–665, 2003.

[76] K. R. Sundberg, "A group–dipole interaction model of the molecular polarizability and the molecular first and second hyperpolarizabilities," *J. Chem. Phys.*, vol. 66, pp. 114–118, 1977.